UNIVERSITY OF CALIFORNIA,
IRVINE

Application of Plasmonic Enhancement in Spin-Transfer Torque Random Access Memory (STT-RAM)

DISSERTATION

submitted in partial satisfaction of the requirements
for the degree of

DOCTOR OF PHILOSOPHY

in Electrical and Computer Engineering

by

Parinaz Sadri-Moshkenani

Dissertation Committee:
Professor Ozdal Boyraz, Chair
Professor Nader Bagherzadeh
Professor Hung Cao

2022

DEDICATION

To my parents, for being great role models and for their invaluable support and encouragement throughout my academic life.

TABLE OF CONTENTS

Page

LIST OF FIGURES

LIST OF TABLES

ACKNOWLEDGEMENTS

I would like to thank my PhD advisor, Professor Boyraz, for supporting and guiding me through my PhD, and for his flexibility and patience while I was making my way through research, for his great ideas and helpful perspectives, which were of great help to my progress, and finally his positive and professional attitude.

I also want to thank Professor Nader Bagherzadeh, who was the principal investigator of the interdisciplinary project that my dissertation was based on, for facilitating communication between the people involved in the project and for his persistence in leading the project to progress in a reasonable time frame.

Special thanks to Dr. Eric A. Montoya, who helped me with the interdisciplinary information I needed for my part of the project, being a great researcher and communicator, he always made an effort to be available on a timely manner for the needs of the project.

My sincere thanks also go to the alumni members of my research group, Dr. Rasul Torun and Dr. Qiancheng Zhao, who helped me with their perspectives towards research and working with the optical instruments in Advanced Photonic Devices and Systems Laboratory at UCI.

And thanks to the current members of my research group at, Mohammad Wahiduzzaman Khan, Mustafa Mert Bayer, and Md Shafiqul Islam, who I had the pleasure to work with closely and have done a great job keeping the environment of our research lab friendly yet professional where everyone is willing to help each other with a positive attitude.

Great thanks to my father, may he rest in peace, who inspired my never-ending passion for learning by showing me the joy of it and by being a great role model to look up to. And my mother, who inspired me to never give up and to finish what I started, no matter how long and tough things get.

VITA

Parinaz Sadri-Moshkenani

2012 B.S. in Electrical Engineering, Isfahan University of Technology

2015 M.S. in Electrical Engineering, University of Tehran

2016-22 Teaching Assistant, University of California, Irvine

2018 Modeling and Simulation Intern, Imec USA

2019 Image Sensor Characterization Intern, ON Semiconductor

2022 R&D Diagnostics Intern, Alcon

2022 Ph.D. in Electrical and Computer Engineering, University of California, Irvine

JOURNAL PUBLICATIONS

P. Sadri-Moshkenani, M. W. Khan, M. S. Islam, E. A. Montoya, I. Krivorotov, and O. Boyraz, "Optoelectronic Readout of STT-RAM Based on Plasmon Drag Effect," IEEE Journal of Quantum Electronics, vol. 57, pp. 1-7, September 2021.

P. Sadri-Moshkenani, M. W. Khan, M. S. Islam, E. A. Montoya, I. Krivorotov, N. Bagherzadeh, and O. Boyraz, "Effect of magnesium oxide adhesion layer on resonance behavior of plasmonic nanostructures," Applied Physics Letters, vol. 116, pp. 241601, June 2020.

M. W. Khan, Q. Zhao, P. Sadri-Moshkenani, M. S. Islam, and O. Boyraz, "Graphene-incorporated plasmo-thermomechanical infrared radiation detection," JOSA B, vol. 37, pp. 774-783, March 2020.

P. Sadri-Moshkenani, M. W. Khan, M. S. Islam, I. Krivorotov, M. Nilsson, N. Bagherzadeh, and O. Boyraz, "Array of symmetric nanohole dimers with high sensitivity for detection of changes in an STT-RAM ultrathin dielectric layer," JOSA B, vol. 36, pp. 3090-3097, November 2019.

P. Sadri-Moshkenani, J. Rashed-Mohassel, and M. Shahabadi, "Microstrip antenna array fed by a low-loss gap-waveguide feed network," IEEE Transactions on Antennas and Propagation, vol. 66, pp. 4359-4363, August 2018.

Q. Zhao, P. Sadri-Moshkenani, M. W. Khan, R. Torun, and O. Boyraz, "On-chip bimetallic plasmo-thermomechanical detectors for mid-infrared radiation," IEEE Photonics Technology Letters, vol. 29, pp. 1459-1462, September 2017.

CONFERENCE PUBLICATIONS

M. S. Islam, I. U. Zaman, P. Sadri-Moshkenani, M. W. Khan, and O. Boyraz, "Metalens wide-angle receiver for free space optical communications," SPIE Optics and Photonics Conference, San Diego, CA, August 2021.

P. Sadri-Moshkenani, M. W. Khan, M. S. Islam, D. Shi, E. A. Montoya, I. Krivorotov, N. Bagherzadeh, and O. Boyraz. "Optoelectronic Readout of STT-RAM Memory Cells Using Plasmon Drag Effect," OSA Conference on Lasers and Electro-Optics (CLEO), San Jose, CA, May 2021.

D. Shi, O. Boyraz, K. Cui, M. S. Islam, and P. Sadri-Moshkenani, "Wide-angle beam focusing with a tuning GeSbTe phase-change metalens," SPIE Photonics West, Online, March 2021

M. W. Khan, P. Sadri-Moshkenani, M. S. Islam, and O. Boyraz, "Active modulation of optical leaky wave antenna by vanadium dioxide corrugations," SPIE Optics and Photonics Conference, Online, September 2020.

M. W. Khan, P. Sadri-Moshkenani, M. S. Islam, O. Boyraz, J. Sullivan, Z. Yu, and J. Lee, "Selective and efficient infrared detection by plasmonically heated vanadium-dioxide nanowire," SPIE Optics and Photonics Conference, Online, September 2020.

P. Sadri-Moshkenani, M. W. Khan, M. M. Bayer, M. S. Islam, E. A. Montoya, I. Krivortov, M. Nilsson, N. Bagherzadeh, and O. Boyraz, "Effect of Tantalum and MgO adhesion layers on plasmonic nanostructures," SPIE Optics and Photonics Conference, San Diego, CA, September 2019.

G. Ghazi, P. Sadri-Moshkenani, and R. Safian, "Array optimization for maximum realized gain in terahertz antenna with lens," IEEE International Symposium on Antennas and Propagation and USNC-URSI Radio Science Meeting, July 2019.

M. W. Khan, P. Sadri-Moshkenani, M. S. Islam, and O. Boyraz, "Graphene-coated suspended metallic nanostructures for fast and sensitive optomechanical infrared detection," OSA Conference on Lasers and Electro-Optics (CLEO), San Jose, CA, May 2019.

P. Sadri-Moshkenani, M. W. Khan, M. S. Islam, I. Krivorotov, M. Nilsson, N. Bagherzadeh, and O. Boyraz, "Array of symmetric nanohole dimers for STT-RAM ultrathin layer sensing," OSA Conference on Lasers and Electro-Optics (CLEO), San Jose, CA, May 2019.

Q. Zhao, M. W. Khan, P. Sadri-Moshkenani, R. Regan, F. Capolino, and O. Boyraz, "Demonstration of a Plasmo-Thermomechanical Radiation Detector with Si3N4 Waveguide Optical Readout Circuit," OSA Conference on Lasers and Electro-Optics (CLEO), San Jose, CA, May 2018.

Q. Zhao, M. W. Khan, P. Sadri-Moshkenani, R. Torun, I. U. Zaman, and O. Boyraz, "Plasmo-thermomechanical suspended nanowire array detectors for mid-infrared spectrum," SPIE Optics and Photonics Conference, San Diego, CA, August 2017.

P. Sadri-Moshkenani, M. W. Khan, Q. Zhao, I. Krivorotov, M. Nilsson, N. Bagherzadeh, and O. Boyraz, "Plasmonic detection of possible defects in multilayer nanohole array consisting of essential materials in simplified STT-RAM cell," SPIE Optics and Photonics Conference, San Diego, CA, August 2017.

Q. Zhao, P. Sadri-Moshkenani, M. W. Khan, R. Torun, I. U. Zaman, and O. Boyraz, "Infrared detection using plasmonically enhanced thermomechanically actuated nanowire arrays," OSA Conference on Lasers and Electro-Optics (CLEO), San Jose, CA, May 2017.

S. Rahman, P. Sadri-Moshkenani, R. Torun, and O. Boyraz, "Space-time-wavelength mapping based electronically controlled two dimensional optical tweezing," OSA Conference on Lasers and Electro-Optics (CLEO), San Jose, CA, June 2016.

ABSTRACT OF THE DISSERTATION

Application of Plasmonic Enhancement in Spin-Transfer Torque Random Access Memory (STT-RAM)

By

Parinaz Sadri-Moshkenani

Doctor of Philosophy in Electrical and Computer Engineering

University of California, Irvine, 2022

Professor Ozdal Boyraz, Chair

Spin-transfer torque random access memory (STT-RAM) is a new memory technology which has attracted significant interest in recent years, due to its low power consumption, scalability, and high speed. Specifically for its potential use in space applications, it is important to quantify its robustness under ionizing radiation, e.g., gamma radiation. To this end, here, utilizing plasmonic sensing is proposed and theoretically demonstrated for in situ detection of defects caused by ionizing radiations. Plasmonic nanostructures are highly used for sensing purposes as they support strong field enhancement in nanoscale, making them highly sensitive to the refractive index change of their surrounding medium. STT-RAM structure in its simple form includes a dielectric barrier layer (MgO) sandwiched between two ferromagnetic layers (CoFeB), all placed between two metal layers for electrical contact (Au). The metal layers in STT-RAM structure can be utilized to support plasmonic resonance thus enable sensing of nanoscale changes

that can be caused by irradiation. This is demonstrated via creating a nanohole array pattern in the STT-RAM multilayer. Moreover, the sensing performance is further improved by designing a dimer nanohole array.

Fabrication of STT-RAM multilayer requires the presence of a dielectric substrate, onto which the layers are deposited. Therefore, there is a need for adhering the Au contact layer onto common dielectric substrate materials. However, as Au is a noble metal, an adhesion layer is necessary to achieve its firm bonding onto the substate. Conventional adhesion materials include metals like Cr, Ti, and Ta, which adversely affect the plasmonic resonance thus degrading the sensing performance. Here, MgO is proposed as an alternative low loss adhesion layer and tested optically and mechanically. It is shown that is has negligible effect on plasmonic resonance as well as strong adhesion performance.

Finally, an opto-electronic readout scheme for STT-RAM cells is proposed and theoretically demonstrated. This method offers simplification of the readout circuitry as well as offering potential for high-speed readout of memory cells, without using conventional photodetectors. The proposed readout scheme is based on plasmonic enhancement of a nonlinear phenomenon called optical rectification. A single optical beam illuminates an array of STT-RAM cells, inducing electrical voltage in each cell, which is used to determine the memory state. Plasmonic enhancement is shown to provide approximately 20 times enhancement in variation of the photo-induced voltage with respect to the memory state. As a result, the proposed readout method offers potential for improving the memory readout rate, provided that proper supporting electronic circuitry is available.

Chapter 1

Introduction

New memory technologies that allow high density memory cells, high speed, and low power read and write abilities have been extensively studied in the literature. Among them, spin-transfer torque random access memory (STT-RAM) has received significant attention due to its low power consumption (100 f J per switch), high endurance, and high speed (read and write speed of 1 ns to 10 ns). In addition, STT-RAM technology offers good scalability, which is due to switching current reduction when the width of memory cells is decreased [1-5].

Core element of STT-RAM consists of a thin (nanoscale thickness) dielectric layer (typically MgO) placed between two ferromagnetic layers (typically CoFeB). Such combination of layers forms a magnetic tunnel junction (MTJ), placed between two metal electrodes as shown in Figure 1.1(a) [2]. The metal electrode layer typically includes one or more metal films which may include noble metals such as Au or Pt, as well as a nonmagnetic buffer including metals such as Ta, ruthenium (Ru), and tungsten (W) or a combination of them. The purpose of buffer layer is to improve surface flatness, film adhesion, and crystalline growth [6-8]. However, such layers also introduce optical losses and degrade the plasmonic performance that is intended here. Therefore, for the most part of this dissertation, only the essential part of MTJ stack (ferromagnet/dielectric/ferromagnet [6]) is included in the designed nanostructures.

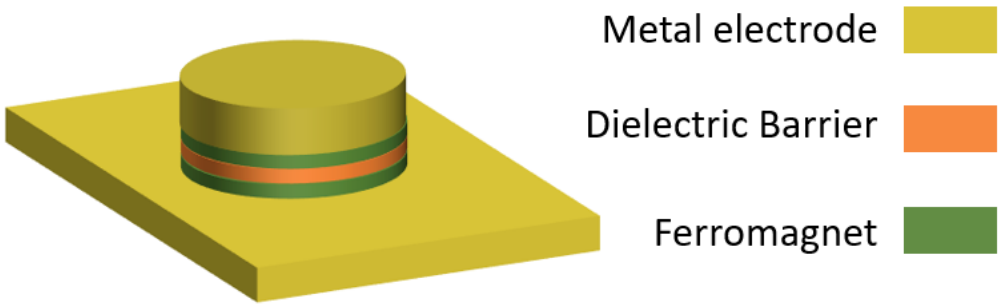

(a)

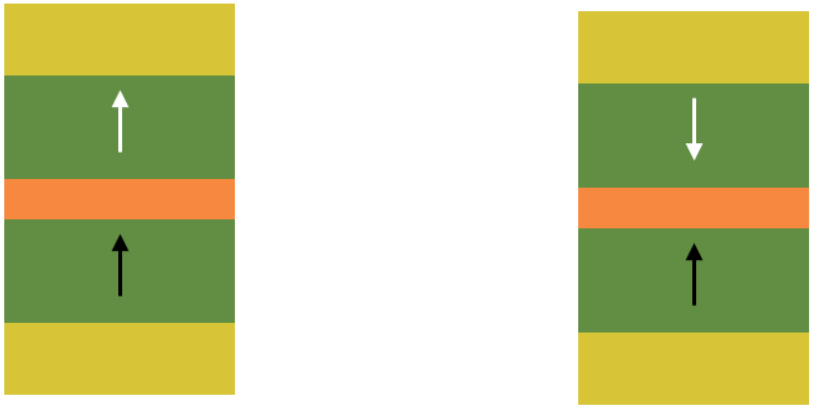

(b) (c)

Figure 1.1 (a) Basic structure of STT-RAM including its core element which is an MTJ (ferromagnet/dielectric/ ferromagnet) sandwiched between metal electrode layers, (b,c) Cross section of STT-RAM showing its magnetic states: (b) parallel, (c) anti-parallel.

The principle of STT-RAM for recording information is based on creating a spin-polarized tunneling current, which can be created between the two ferromagnetic layers if the dielectric barrier layer is thin enough. In general, the magnetic moment of one of the ferromagnetic layers (free layer) can be in "parallel" state with regards to the magnetic

moment of the other ferromagnetic layer (pinned layer), resulting in a high magnetoresistance, or in "anti-parallel" state to the pinned layer, showing a low magnetoresistance (Figure 1.1(b,c)). By applying a voltage pulse to the MTJ, a spin-polarized current can be created which transfers spin angular momentum from the pinned layer to the free layer [9-11]. This transfer results in application of a torque on magnetization of the free layer thus reversing the magnetization of it.

Although STT-RAM technology is promising it also has certain challenges, one of which is the small difference between the values of tunneling magnetoresistance (TMR) in parallel versus anti-parallel states (typically $\frac{R_{AP}}{R_P} < 2.5$). Such small difference requires tight tolerances on variations of write voltage levels and TMR variations from one device to another [12, 13]. Furthermore, a small change of conductivity in the dielectric layer due to radiation damages caused by ionizing radiation can flip the state of the memory cell and cause bit error. Radiation damage becomes an important subject when it comes to space applications, to assure their stability when used in such applications [14]. Due to the structure of STT-RAM and because of the nanoscale thickness of its layers, understanding the effect of ionizing radiation on it is a challenge. Focusing on the core elements of STT-RAM (ferromagnetic/dielectric/ferromagnetic), the dielectric layer is where the main radiation damages are expected to occur, since the metallic alloys are robust against the ionized radiation. Radiation damages in dielectric layers typically include electric charge accumulation and atomic displacements resulting in color center formation. In thin dielectric films, radiation induced defects are shown to create a conductive channel passing a leakage

current [15-17]. This can affect the state of the memory cells and result in loss of the stored information in them, which needs to be studied.

One way to study the level of radiation hardness of STT-RAM, is to use optical sensing methods. Such methods are capable of sensing nanoscale changes which are suitable for detection of possible radiation defects in the ultrathin dielectric layer in STT-RAM structure, due to the small wavelength of the optical frequencies. Since the structure of STT-RAM includes metallic layers, one can utilize them to localize the detection to the dielectric layer further through excitation of surface plasmons. In specific, noble metals like gold and silver are known to have good plasmonic performance, with gold being more chemically stable [18]. As a result, using them as the metal electrodes in the STT-RAM structure or adding them to the STT-RAM multilayer, one can excite plasmonic modes thus achieving enhanced sensing of possible radiation damages in STT-RAM [14, 19, 20]. Chapter 3 of this dissertation presents further discussion of such enhancement, where plasmonic designs are provided as well as their sensitivity to the changes in the MgO layer is quantified via simulations.

STT-RAM layers are typically deposited on an SiO_x(100nm)/Si substrate. Therefore, when using noble metals as electrodes in the structure of STT-RAM, an adhesion layer is needed to create a bond between them and the oxide layer of the substrate. The adhesion material used most in the literature are Cr, Ti, and Ta, which degrade the plasmonic sensing performance by creating excess damping of plasmonic resonance due to their optical losses [6, 21-24]. To avoid this, low-loss adhesion layers are suggested instead, such as ITO, TiO_2, Cr_2O_3, or using a molecular link for adhesion [24-29]. Another approach is using a modified fabrication

process called angular evaporation method to achieve less overlap between the localized field hotspots and the adhesion material so the damping effect of lossy adhesion material on plasmonic resonance becomes less [30]. This technique, however, has the drawback of requiring a more complicated fabrication. As an alternative low-loss adhesion material, MgO is demonstrated via mechanical and optical characterization to be an alternative low-loss adhesion material [31, 32], which is elaborated in Chapter 4 of this dissertation.

Another important aspect when dealing with random access memory (RAM), in addition to their radiation hardness, is how to access the information stored in the memory cells, i.e., their readout method. RAM readout can be performed optically or electrically, where the former offers advantages such as, improved memory performance, simplified readout circuitry, and increased data transfer rate between memory cells and the processor unit [33-38]. To achieve these advantages for STT-RAM in specific, an opto-electronic readout scheme can be designed. Conversion of optical field to electric voltage can be performed via optical rectification (OR), which is a nonlinear optical phenomenon and can be further enhanced through plasmonic resonance. The enhancement of OR effect through plasmonic resonance is called plasmon drag effect (PLDE) [39-41]. The voltage enhancement can be used towards a potentially high-speed readout (from the optical design point of view), assuming conventional electronics are used for the voltage measurement [42, 43]. It should be noted that such readout method also has the advantage of not needing the addition of III-V semiconductor materials for the opto-electronic conversion, which are conventionally used in photodetectors and light sources and not CMOS-compatible [33, 34, 37]. Chapter 5, the final chapter of this dissertation, presents the design and numerical study of the proposed

opto-electronic readout scheme for STT-RAM, where the photo-induced voltage is calculated. Finally, the dissertation ends with a general conclusion on all the presented works.

Chapter 2

Basics of Plasmonics

In this chapter, fundamentals of plasmonic are explained. To do so, starting from Maxwell's equations, which describe the electromagnetics theory, simple cases of plasmonic enhancement for different types of plasmonic modes (propagating versus non-propagating) are discussed.

2.1 Maxwell's Equations

Maxwell's equations represent a macroscopic formulation of electromagnetism, that were published in 1873 [44]. The point form of Maxwell's equation in SI units are summarized in the following:

$$\nabla . \boldsymbol{D} = \rho_s \tag{2.1}$$

$$\nabla . \boldsymbol{B} = 0 \tag{2.2}$$

$$\nabla \times \boldsymbol{E} = -\frac{\partial \boldsymbol{B}}{\partial t} \tag{2.3}$$

$$\nabla \times \boldsymbol{H} = \boldsymbol{J}_s + \frac{\partial \boldsymbol{D}}{\partial t} \tag{2.4}$$

where **E** is the electric field, **H** is the magnetic field, $\mathbf{J_s}$ is the applied current density source, and ρ_s is the charge density source applied. **D** and **B** are the electric and magnetic flux densities, which are related to **E** and **H** through the material properties in the following way:

$$\boldsymbol{D} = \varepsilon_0 \boldsymbol{E} + \boldsymbol{P} \tag{2.5}$$

$$\boldsymbol{B} = \mu_0 \boldsymbol{H} + \boldsymbol{M} \tag{2.6}$$

where **P** is the electric polarization density, **M** is the magnetization density, ε_0 (8.85×10^{-12} F/m) and μ_0 ($4\pi\times10^{-7}$ H/m) are the electric permittivity and permeability of vacuum, respectively, which are related to the speed of light (c) via the equation $c = \frac{1}{\sqrt{\varepsilon_0 \mu_0}}$.

For the case of linear and isotropic material, equations (2.5) and (2.6) can be written as:

$$\boldsymbol{D} = \varepsilon \boldsymbol{E} \tag{2.7}$$

$$\boldsymbol{B} = \mu \boldsymbol{H} \tag{2.8}$$

where $\varepsilon = \varepsilon_0 \varepsilon_r$ is the material permittivity, ε_r being its relative permittivity, and $\mu = \mu_0 \mu_r$ is the material permeability, μ_r being its relative permeability.

To fully account for the material properties, one needs to consider the equation below in addition to equations (2.7) and (2.8):

$$\boldsymbol{J} = \sigma \boldsymbol{E} \tag{2.9}$$

where σ is the conductivity of the material and **J** is the internal current density.

2.2 Wave Equation

Maxwell's curl equations, (2.3) and (2.4) show that a time-varying magnetic field creates an electric field that a time-varying electric field creates a magnetic field. Combining these two equations results in the wave equation, which is the key to solve Maxwell's equations.

Equations (2.3), (2.4) can be combined using the linear relationship between **B** and **H** given in equation (2.8). This, in the absence of charge and current density sources (source-free medium ρ=0, **J**=0), results in the following:

$$\nabla \times \nabla \times \boldsymbol{E} = -\mu \frac{\partial^2 \boldsymbol{D}}{\partial t^2} \tag{2.10}$$

which can be rewritten using the identities $\nabla \times \nabla \times \boldsymbol{E} = \nabla(\nabla . \boldsymbol{E}) - \nabla^2 \boldsymbol{E}$ and $\nabla . (\varepsilon \boldsymbol{E}) = \boldsymbol{E} . \nabla \varepsilon + \varepsilon \nabla . \boldsymbol{E}$ as well as $\nabla . \boldsymbol{E} = 0$, which results from equation (2.1) under source-free condition. This leads to the equation:

$$\nabla(-\frac{1}{\varepsilon} \boldsymbol{E} . \nabla \varepsilon) - \nabla^2 \boldsymbol{E} = -\mu\varepsilon \frac{\partial^2 \boldsymbol{E}}{\partial t^2} \tag{2.11}$$

This can be simplified for a homogeneous medium (spatially constant permittivity) into the *wave equation* for electric field:

$$\nabla^2 \boldsymbol{E} - \frac{\varepsilon_r \mu_r}{c^2} \frac{\partial^2 \boldsymbol{E}}{\partial t^2} = 0 \tag{2.12}$$

The *wave equation* for magnetic field can be derived in a similar fashion:

$$\nabla^2 \boldsymbol{H} - \frac{\varepsilon_r \mu_r}{c^2} \frac{\partial^2 \boldsymbol{H}}{\partial t^2} = 0 \tag{2.13}$$

2.3 Time-Harmonic Dependence

Maxwell's equations can be simplified if one assumes the time variation of the fields to be steady-state sinusoidal (time-harmonic). In such case, electric and magnetic fields for the

case can be written in phasor form as:

$$\boldsymbol{E}(x,y,z,t) = \boldsymbol{E}(x,y,z)e^{j\omega t} \tag{2.14}$$

$$\boldsymbol{H}(x,y,z,t) = \boldsymbol{H}(x,y,z)e^{j\omega t} \tag{2.15}$$

Substituting equations (2.14) and (2.15) into the Maxwell's equations (2.1) through (2.4) and eliminating the $e^{j\omega t}$ term, the time-harmonic form of Maxwell's equations is:

$$\nabla . \boldsymbol{D} = \rho_s \tag{2.16}$$

$$\nabla . \boldsymbol{B} = 0 \tag{2.17}$$

$$\nabla \times \boldsymbol{E} = -j\omega \boldsymbol{B} \tag{2.18}$$

$$\nabla \times \boldsymbol{H} = \boldsymbol{J_s} + j\omega \boldsymbol{D} \tag{2.19}$$

Similarly, the *wave equation* (2.12) turns into a time-independent equation, known as *Helmholtz equation*:

$$\nabla^2 \boldsymbol{E} + k^2 \boldsymbol{E} = 0 \tag{2.20}$$

Where $k = k_0\sqrt{\varepsilon_r \mu_r}$ is the wave vector in the material with relative permittivity/dielectric constant of ε_r, relative permeability of μ_r, and $k_0 = \frac{\omega}{c}$ is the wave vector in vacuum.

Regarding the material properties for the case of time-harmonic dependence, one can combine equations (2.5), (2.7), and (2.9) with the fundamental formula $\boldsymbol{J} = \frac{\partial \boldsymbol{P}}{\partial t}$ relating the internal current density and the electric polarization density, to obtain the relationship between relative permittivity and conductivity of the material [45]:

$$\varepsilon_r = 1 - \frac{j\sigma}{\varepsilon_0 \omega} \tag{2.21}$$

This shows that in time-harmonic analysis, the relative permittivity is complex-valued ($\varepsilon_r = \varepsilon_1 - j\varepsilon_2$), which includes the information for conductivity of material.

Alternatively, material properties may be stated using its complex refractive index, $\tilde{n} = n - j\kappa$, defined as $\tilde{n} = \sqrt{\varepsilon_r \mu_r}$. For a nonmagnetic material ($\mu_r = 1$), this results in the following equations:

$$\varepsilon_1 = n^2 - \kappa^2 \tag{2.22}$$

$$\varepsilon_2 = 2n\kappa \tag{2.23}$$

κ is the extinction coefficient, which quantifies the attenuation/absorption of the propagating wave in the medium.

2.4 Wave Propagation in Planar Geometry

To analyze the propagation of wave in a planar geometry, the geometry shown in Figure 2.1 is considered. It is assumed that permittivity is only a function of z ($\varepsilon_r = \varepsilon_r(z)$). Considering time-harmonic dependence, and the propagation direction to be along the x direction, the electric field for the propagating wave would be in the form $\boldsymbol{E}(x, y, z) = \boldsymbol{E}(z)e^{-j\beta x}$, and $\boldsymbol{H}(x, y, z) = \boldsymbol{H}(z)e^{-j\beta x}$, where β is the propagation constant of the wave which is the x component of the wave vector. With these assumptions, there are no changes along y direction ($\frac{\partial}{\partial y} = 0$) and $\frac{\partial}{\partial x}$ can be replaced with $-j\beta$. As a result, the following can be obtained

from equations (2.18), (2.19), and (2.20) [45]:

$$\frac{\partial^2 \boldsymbol{E}(z)}{\partial z^2} + (k^2 - \beta^2)\boldsymbol{E} = 0 \tag{2.24}$$

$$\frac{\partial^2 \boldsymbol{H}(z)}{\partial z^2} + (k^2 - \beta^2)\boldsymbol{H} = 0 \tag{2.25}$$

$$\frac{\partial E_y}{\partial z} = j\omega\mu H_x \tag{2.26}$$

$$\frac{\partial E_x}{\partial z} + j\beta E_z = -j\omega\mu H_y \tag{2.27}$$

$$-j\beta E_y = -j\omega\mu H_z \tag{2.28}$$

$$\frac{\partial H_y}{\partial z} = -j\omega\varepsilon E_x \tag{2.29}$$

$$\frac{\partial H_x}{\partial z} + j\beta H_z = j\omega\varepsilon E_y \tag{2.30}$$

$$-j\beta H_y = j\omega\varepsilon E_z \tag{2.31}$$

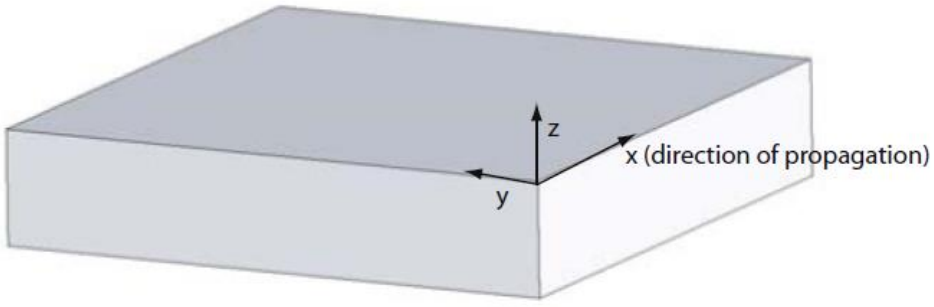

Figure 2.1. Definition of planar geometry for propagation of wave. Direction of propagation is along the x direction [45].

It can be shown that the above system of equations has two sets of solutions with different polarizations: transverse magnetic (TM or p) and transverse electric (TE or s) modes [45]. The nonzero field components for TM mode are E_x, E_z, H_y and the ones for TE mode are H_x, H_z, E_y.

For TM mode, the curl equations result in E_x and E_z being formulated based on H_y:

$$E_x = \frac{j}{\omega \varepsilon_0 \varepsilon_r} \frac{\partial H_y}{\partial z} \tag{2.32}$$

$$E_z = \frac{-\beta}{\omega \varepsilon_0 \varepsilon_r} H_y \tag{2.33}$$

, and the equation (2.20) simplifies into the following wave equation for TM mode:

$$\frac{\partial^2 H_y}{\partial z^2} + (k^2 - \beta^2) H_y = 0 \tag{2.34}$$

Similarly, for TE mode, H_x and H_z can be formulated based on E_y:

$$H_x = \frac{-j}{\omega \mu_0} \frac{\partial E_y}{\partial z} \tag{2.35}$$

$$H_z = \frac{\beta}{\omega \mu_0} E_y \tag{2.36}$$

, and the wave equation for TE mode is:

$$\frac{\partial^2 E_y}{\partial z^2} + (k^2 - \beta^2) E_y = 0 \tag{2.37}$$

2.5 Plasmonic Modes

Plasmonics is the science describing the interaction of light with matter through excitation of electromagnetic surface modes at a metal-dielectric interface. Such modes are collective oscillations of electrons, which can be in the form of propagating waves at a planar metal-dielectric interface (surface plasmon polaritons) or in the form of local oscillations at the surface of metal nanoparticles (localized surface plasmons) [45, 46]. Plasmonic modes offer strong localization of electric field (Figure 2.2), which makes them highly sensitive to changes. The following sections explain the basics and formulations for the two main categories of plasmonic modes.

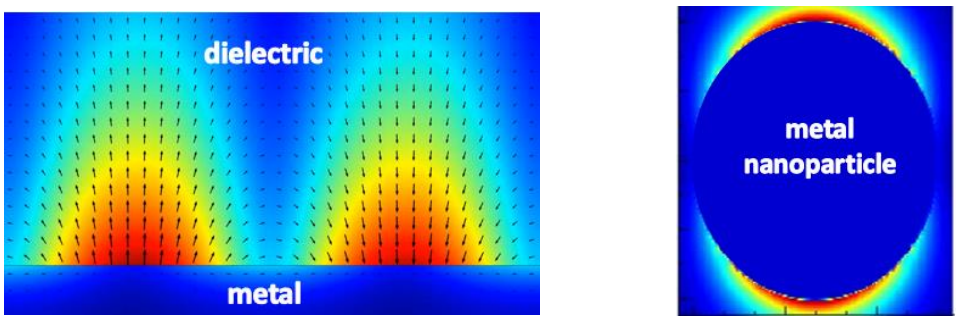

Figure 2.2 Spatial distribution of electric field magnitude showing field localization for (a) surface plasmon polaritons excited at a planar metal dielectric interface, (b) localized surface plasmons excited at the surface of a metal nanoparticle placed in a dielectric medium.

2.5.1 Surface Plasmon Polaritons (SPPs)

Surface plasmon polaritons are electromagnetic surface waves propagating at the interface between a metal and a dielectric, which originate from coupling of the electromagnetic fields

to the electron plasma of the metal.

In this section, the basics of SPP is explained through theoretical analysis of the simplest geometry capable of supporting SPPs, a single planar metal-dielectric interface. Figure 2.3 shows such geometry, where the z>0 half space is filled with a dielectric and the z<0 half space is occupied by a metal. The goal here is to find the modes confined to the interface and propagating along it for the case of time-harmonic dependence. Under such assumptions, the following can be written for magnetic field component of TM mode in the z>0 half space (dielectric region):

$$H_y = A_d e^{-j\beta x} e^{-k_d z} \tag{2.38}$$

where A_d is the magnitude of magnetic field at the interface, and k_d is the z component of the wave vector, which quantifies the field confinement to the interface via introducing an evanescent decay along +z direction. Subscript "d" refers to the dielectric region.

Substituting equation (2.36) into equations (2.32) and (2.33), electric field components can be obtained:

$$E_x = -jA_d \frac{k_d}{\omega \varepsilon_0 \varepsilon_d} e^{-j\beta x} e^{-k_d z} \tag{2.39}$$

$$E_z = -A_d \frac{\beta}{\omega \varepsilon_0 \varepsilon_d} e^{-j\beta x} e^{-k_d z} \tag{2.40}$$

Similarly, for the z<0 half space, the field components are:

$$H_y = A_m e^{-j\beta x} e^{k_m z} \tag{2.41}$$

$$E_x = jA_m \frac{k_m}{\omega \varepsilon_0 \varepsilon_m} e^{-j\beta x} e^{k_m z} \tag{2.42}$$

$$E_z = -A_m \frac{\beta}{\omega \varepsilon_0 \varepsilon_m} e^{-j\beta x} e^{k_m z} \tag{2.43}$$

where subscript "m" refers to the metal region.

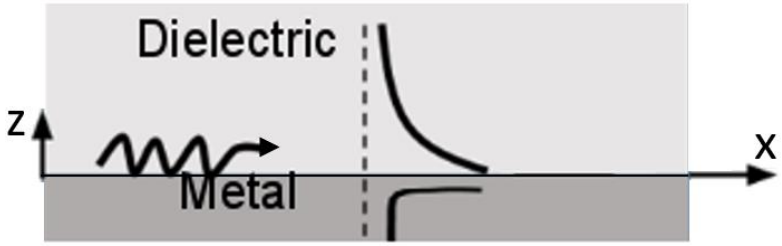

Figure 2.3 Geometry of a planar metal-dielectric interface and simple illustration of the supported SPP modes propagating along the interface with their field confined to the interface.

Applying continuity boundary condition for the tangential field components at the interface (H_y and E_x) results in $A_d = A_m$ and the following:

$$\frac{k_d}{k_m} = -\frac{\varepsilon_d}{\varepsilon_m} \tag{2.44}$$

It should be noted that the field confinement/localization at the interface requires the real part of k_d and k_m to be both positive. This means that equation (2.44) is satisfied only when ε_d and the real part of ε_m have opposite signs, meaning $\mathrm{Re}\{\varepsilon_m\} < 0$.

Furthermore, substituting equations (2.38) and (2.41) into the wave equation (2.34), assuming both the dielectric and the metal are nonmagnetic ($\mu_d = \mu_m = 1$), leads to:

$$k_d^2 + k_0^2 \varepsilon_d - \beta^2 = 0 \tag{2.45}$$

$$k_m^2 + k_0^2 \varepsilon_m - \beta^2 = 0 \tag{2.46}$$

Solving these two equations for β, the dispersion equation for SPP mode is written as:

$$\beta = \frac{k_0 \sqrt{\varepsilon_d \varepsilon_m}}{(\varepsilon_d + \varepsilon_m)} \tag{2.47}$$

Similarly, for TE mode, equations (2.35) and (2.36) can be used to formulate the field components for both dielectric and metal regions, then boundary conditions at the interface can be applied. It can be shown that the boundary conditions require the field to be zero. This means TE -polarized SPP mode is supported by the metal-dielectric interface, and only TM-polarized SPPs exist in such structure [45].

Going back to the dispersion equation (2.47) obtained for TM-polarized SPPs, in the ideal case of $\mathrm{Im}\{\varepsilon_\mathrm{m}\} = 0$ and $\mathrm{Re}\{\varepsilon_\mathrm{m}\} = -\varepsilon_\mathrm{d}$, a plasmonic resonance occurs, where β becomes infinite, which means ultimate confinement of SPP to the interface, according to equations (2.1)(2.45) and (2.46). However, using measured permittivity data for a metal, it can be shown that $\mathrm{Re}\{\beta\}$ has a finite value which puts an upper limit on the confinement level. This is shown in Figure 2.4 for silver-air and silver-silica interfaces as examples. It should be noted that since the metal permittivity is complex-valued in general, β also has an imaginary part, which means SPPs are modes of high absorption/losses [45].

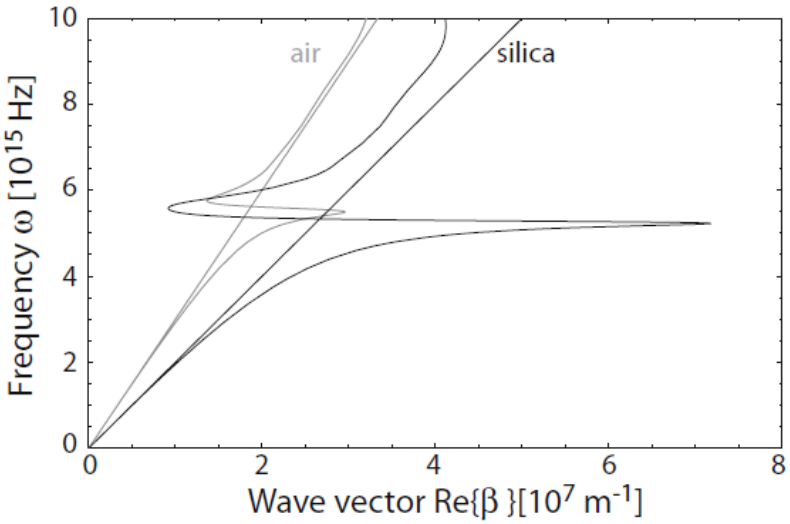

Figure 2.4 Dispersion curve of SPPs at a silver-air interface (gray curve) and a silver-silica (black curve) interface, with light lines of air and silica included [45].

There is also a lower limit for Re{β} for SPPs, where equations (2.1)(2.45) requires Re{β}>$k_0\varepsilon_d$, so the mode is confined at the interface (field localization).. This means that the confined modes are on the right of the light line of the dielectric, shown in Figure 2.4. Therefore, to excite such modes, special techniques should be utilized to satisfy phase matching condition. In addition, for the SPP mode to have stronger confinement (field localization) at the interface, larger values of Re{β} are desired, which can be achieved via tuning the excitation frequency.

Regarding the excitation of SPPs, several methods are used in the literature to satisfy the phase matching condition. The two most common approaches are grating coupling and prism coupling [47-49]. In specific, prism coupling has the drawback of being bulky, so it is not considered in applications where compactness is a criterion. Other approaches for excitation of SPPs include using guided wave excitation through an optical waveguide or

near-field excitation via placing an optical fiber tip in the near field domain of the metal-dielectric interface where the SPP mode propagates (Figure 2.5 (c,d)) [45, 50].

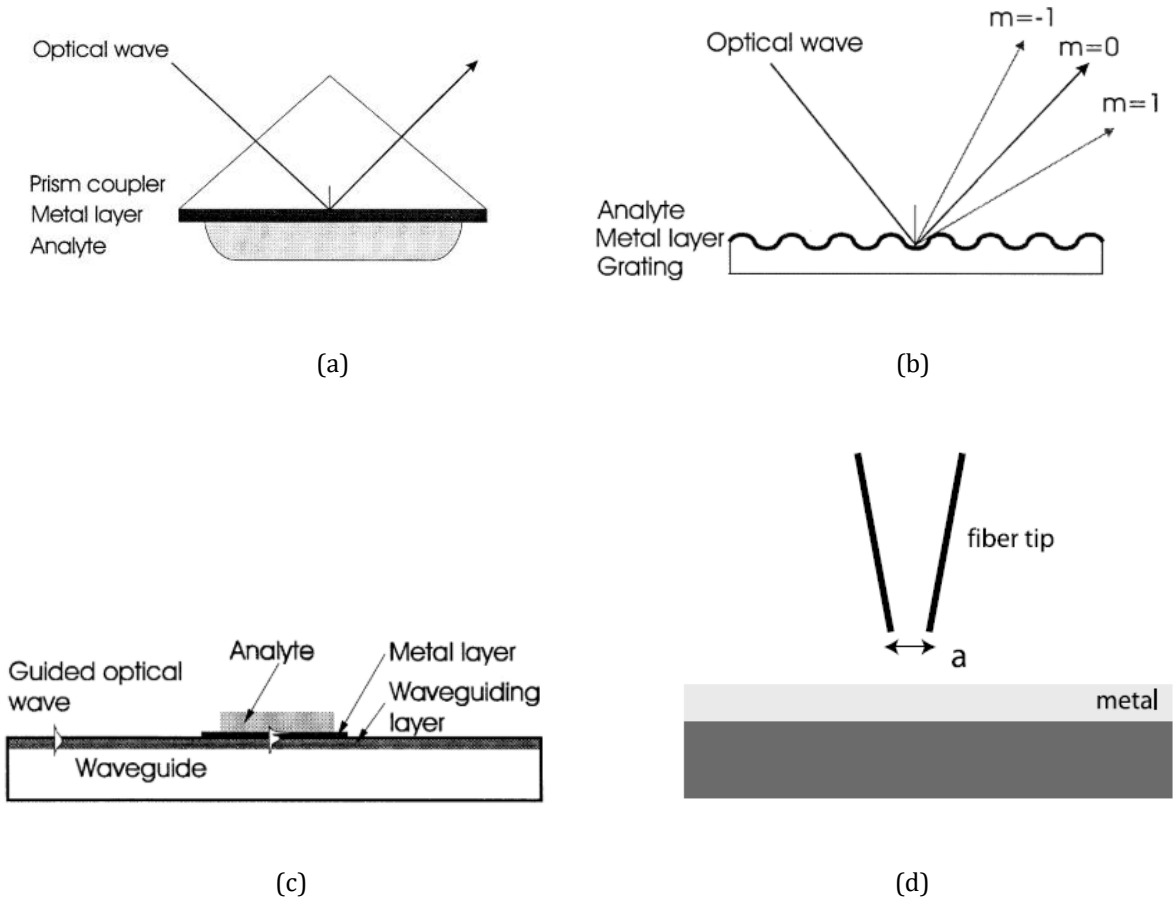

Figure 2.5 SPP excitation techniques (a) prism coupling (b) grating coupling (c) waveguide-based excitation (d) near-field excitation. ((a-c) are from [50], and (d) is from [45]).

In this dissertation, the grating coupling approach is utilized for SPP excitation, which is explained here in further. To explain the grating coupling method, a simple on-dimensional grating is considered (Figure 2.6). The periodicity in such grating helps create phase matching between the in-plane component of wave vector in the dielectric medium ($k_x = k_0 \varepsilon_d \, sin\theta$) and the propagation constant of SPP (β) as [45]:

$$\beta = k_0\sqrt{\varepsilon_d}\, sin\theta + \frac{2m\pi}{p} \tag{2.48}$$

where p is the grating period and m is a nonzero integer.

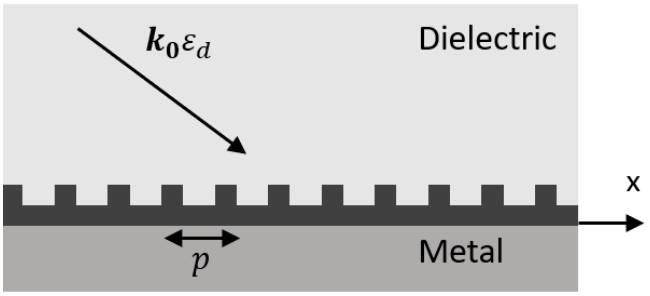

Figure 2.6 Excitation of SPPs via grating coupling technique. The excitation wave is incident from the dielectric medium [45].

2.5.2 Localized Surface Plasmons (LSPs)

Localized surface plasmons are non-propagating localized oscillations of electrons which occur at a metal-dielectric interface of a nanoparticle. Such modes do not need phase matching techniques for their excitations, like SPPs do.

Here, the basics of LSP is explained through the simple case of a spherical particle made of homogeneous isotropic metal with dielectric constant of ε_m placed in a non-absorbing isotropic dielectric medium with dielectric constant of ε_d ($\mathrm{Im}\{\varepsilon_d\} = 0$). To simplify the analysis further, the particle diameter (d) is assumed to much smaller than the wavelength of excitation, $d \ll \lambda$. Under such assumption, for time-harmonic dependence, the phase of electromagnetic field is almost constant, meaning that the field can be approximated to be static (quasi-static approximation).

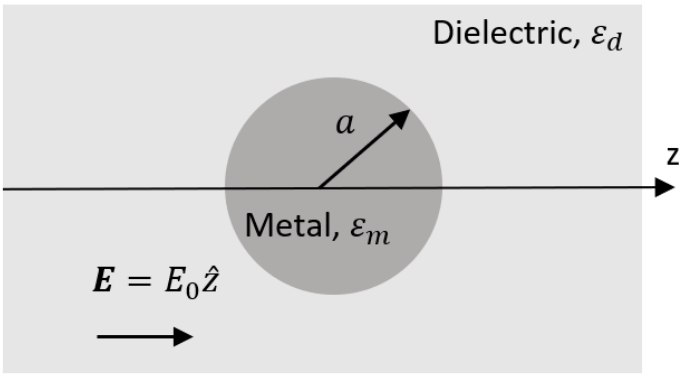

Figure 2.7 A homogeneous isotropic metal sphere placed in a non-absorbing dielectric medium under electrostatic [45].

Figure 2.7 shows the geometry of such structure, where the metal particle is placed at the origin, in a uniform static electric field polarized along z direction, $\boldsymbol{E} = E_0\hat{z}$. To find the modes supported in this structure, one should find the solutions of the Laplace equation for electric potential, $\nabla^2\Phi = 0$, and calculate the electric field from it, using $\boldsymbol{E} = -\nabla\Phi$. For this structure, the general solution to the Laplace equation is [45, 51]:

$$\Phi(r,\theta) = \sum_{n=0}^{\infty} (A_n r^n + B_n r^{-(n+1)}) P_n(cos\theta) \tag{2.49}$$

where r (radial distance) and θ (azimuthal angle) are the two the spherical coordinates, and $P_n(cos\theta)$ are the Legendre Polynomials. This equation holds for the electric potential both inside and outside the sphere (Φ_{in} and Φ_{out}). Considering that the potential should stay finite and that the electric field for $r \to \infty$ is $E_0\hat{z}$, in addition to the continuity conditions for tangential component of the electric field and for normal component of the displacement field at the boundary one can obtain Φ_{in} and Φ_{out} and use $\boldsymbol{E} = -\nabla\Phi$ to calculate the electric field [45, 51]:

$$\boldsymbol{E_{in}} = \frac{3\varepsilon_d}{\varepsilon_m + 2\varepsilon_d}\boldsymbol{E_0} \tag{2.50}$$

$$\boldsymbol{E_{out}} = \boldsymbol{E_0} + \frac{\varepsilon_m - \varepsilon_d}{\varepsilon_m + 2\varepsilon_d} E_0 a^3 \frac{1}{r^2}\left(2cos\theta\,\hat{r} + sin\theta\,\hat{\theta}\right) \tag{2.51}$$

These equations show that a resonance enhancement in electric field occurs if $|\varepsilon_m + 2\varepsilon_d|$ reaches its minimum. This means, the resonance condition for the case of small $\mathrm{Im}\{\varepsilon_m\}$ simplifies into:

$$Re\{\varepsilon_m\} = -2\varepsilon_d \tag{2.52}$$

This equation requires $\mathrm{Re}\{\varepsilon_m\} < 0$, like the case for SPPs.

2.6 Plasmonic Enhancement and Sensing

The strong field localization brought about by the excitation of plasmonic modes (plasmonic resonance) can provide performance enhancement in a variety of applications. Applications of plasmonic enhancement include, but not limited to, photocurrent enhancement in photovoltaic applications [52], surface-enhanced Raman spectroscopy [53], frequency up-conversion efficiency enhancement [54], and chemical and biological sensing applications where the high sensitivity of plasmonic modes to the refractive index change of their surrounding medium facilitates improved sensing performance [50, 55-57]. As for the plasmonic metal for optical frequencies, noble metals have received significant interest due to their good plasmonic performance. Their negative real part of permittivity at such frequencies makes them capable of support surface plasmon modes and their small

imaginary part of permittivity facilitates relatively small losses/damping of plasmonic modes (for both SPP and LSP), which means a stronger resonance and field localization. More specifically, silver and gold are the two most used plasmonic metals for optical frequencies. Silver provides sharper plasmonic resonance than gold, resulting in its higher sensitivity. However, gold is has better chemical stability, which makes it a good candidates for sensing applications in different environments [18]. Further research has been performed, to achieve novel materials which provide reduction of the plasmonic losses compared to gold and silver [58].

Plasmonic sensing can be performed based on SPP or LSP modes in general. Since the excitation of SPPs is dependent on the excitation wavelength and angle of incidence (equation (2.48)). Therefore, SPP resonance shows up as a dip in optical reflection or transmission spectrum. Angular interrogation and wavelength interrogation methods can be used for SPP-based sensing, where a change of resonance angle or wavelength occurs due to refractive index change in the medium. In addition, SPP-based sensing can be done via measurement of intensity near the resonance [50, 59].

Regarding LSP-based sensing, various shapes of metallic nanoparticles are studied in the literature, where the plasmonic enhancement and sensitivity are shown to be affected by the shape and dimensions of the nanoparticles [60, 61]. For LSP sensing, typically extinction (absorption) spectrum is used [62-64]. For measuring local refractive index changes, LSP sensors are more suitable compared to SPP sensors. However, LSP resonances generally have a broader linewidth compared to SPPs due to their radiation losses, which is not desired

in sensing applications [65].

Chapter 3

PLASMONIC DETECTION OF POSSIBLE DEFECTS IN STT-RAM

3.1 Introduction

Plasmonic sensing is among the most highly sensitive detection schemes where the strong field localization of the plasmonic mode contributes to enhanced sensing performance, which can be used to detect possible irradiation defects in STT-RAMs [14, 19, 20]. Among different plasmonic nanostructures, nanohole arrays have attracted lots of interest due to their ease of fabrication, potential for miniaturization, and simplified optical alignment [66]. Because of these properties, in this chapter the plasmonic sensing of STT-RAM is evaluated for nanohole array geometry in the STT-RAM multilayer. Since it is the complementary structure for the nanopillar array, which is the original geometry for an array of STT-RAM cells (unit cell shown on Figure 1.1), the results should give a good enough estimate of the performance.

To further increase the sensitivity of plasmonic sensors, significant research has been [67-70], among which some take the approach of modifying the shape of nanostructures to achieve sensitivity enhancement. As examples, arrays of elliptical nanoholes [71] and overlapping dimer nanoholes [55] can offer a stronger field enhancement and therefore

higher sensitivity due to their sharper geometrical features.

An alternative approach for achieving higher sensitivity in plasmonic devices is to create a Fano resonance, which originates from coupling of a broadband bright mode and a narrowband dark mode. To do so, typically it is necessary to create a form of asymmetry in the nanostructure geometry. Many works have been done in this regard, studying the Fano resonance formed via geometrical asymmetry in the nanostructure arrays made of metallic nanoparticles [62, 63, 72-74] or nanoapertures/nanoholes with different shapes [69, 75, 76], where the asymmetry is typically created by using two or more coupled nanoparticles/nanoapertures in each unit cell, which can be of either the same or different sizes. Specifically, for nanoholes of the same size and shape, examples of quadrumer, heptamer, and heptamer nanohole clusters have been presented in the literature [77-79]. Although non-overlapping nanohole quadrumer and heptamer geometries are studied in the literature, the simple case of non-overlapping nanohole dimers is not studied. Therefore, in this chapter study of dimer nanohole array to create Fano resonance is performed, and its enhancement of sensitivity compared to conventional nanohole array is theoretically quantified for detection of changes in the STT-RAM ultrathin dielectric barrier layer.

In the following, design of nanohole array in STT-RAM multilayer is presented as well as the theoretical demonstration of its ability to detect changes in its ultrathin dielectric barrier layer. Subsequently, modeling and design basics of dimer nanohole array to achieve a highly sensitive Fano resonance are discussed, and its sensitivity to changes of refractive index in the cladding material (bulk sensitivity) is estimated through numerical simulations. Next,

the sensing ability of the designed dimer nanohole array with regards to refractive index changes in STT-RAM dielectric layer due to possible irradiation damage is estimated theoretically. Comparisons with conventional nanohole array are made to show the improvement made in sensing performance by using dimer nanohole array.

3.2 Metrics for Sensing Performance

When it comes to sensing applications, a higher sensitivity, and a sharper resonance (smaller resonance linewidth) is desired. Sensitivity (S) is defined as the resonance shift divided by refractive index change, which for wavelength interrogation has the unit of the unit of nm/RIU:

$$S = \frac{\Delta\lambda}{\Delta n} \tag{3.1}$$

where Δλ is the wavelength shift of the resonance caused by the refractive index change of Δn.

To combine the sensitivity with resonance sharpness in, one can define a figure of merit (FOM), as refractive index sensitivity divided by the resonance linewidth [78] :

$$FOM = \frac{S}{linewidth} \tag{3.2}$$

A better sensing performance is equivalent with larger FOM values, as it facilitates better sensing resolution defined by the following formula [80]:

$$Resolution = \frac{1}{FOM.\Delta I} \tag{3.3}$$

where ΔI is the resonance contrast (or depth). It is important to note that a larger resonance contrast is desirable as it improves the sensing resolution.

3.3 STT-RAM with Tantalum Contact Layers

A typical material used for metal electrodes layers in STT-RAM is tantalum (Ta) [2]. Since the main idea here is to utilize the metal layers in the STT-RAM structure to support plasmonic resonance, an initial step is to evaluate TA for its plasmonic performance. For a TM-polarized SPP mode localized at a Ta/air interface, one can use equation (2.47) taking the permittivity data for Ta from [81], to calculate the propagation constant β.

To achieve strong field localization and therefore high sensitivity, a strong local maximum for $Re\{\beta\}$ is desired when plotted versus frequency. However, the local maximum of $Re\{\beta\}$ is too weak for this case, as shown in Figure 3.1(a) around 440 THz, which means poor confinement and sensitivity. Hence, Ta cannot support an SPP mode because of its high optical losses. This is specifically clear in Figure 3.1(b), which shows the imaginary part of its permittivity has a significant value around 440 THz. To achieve a strong plasmonic resonance, a silver (Ag) film can be added beneath the STT-RAM multilayer stack. This helps because Ag is known to have good plasmonic performance, due to its small losses in the visible and NIR ranges [82].

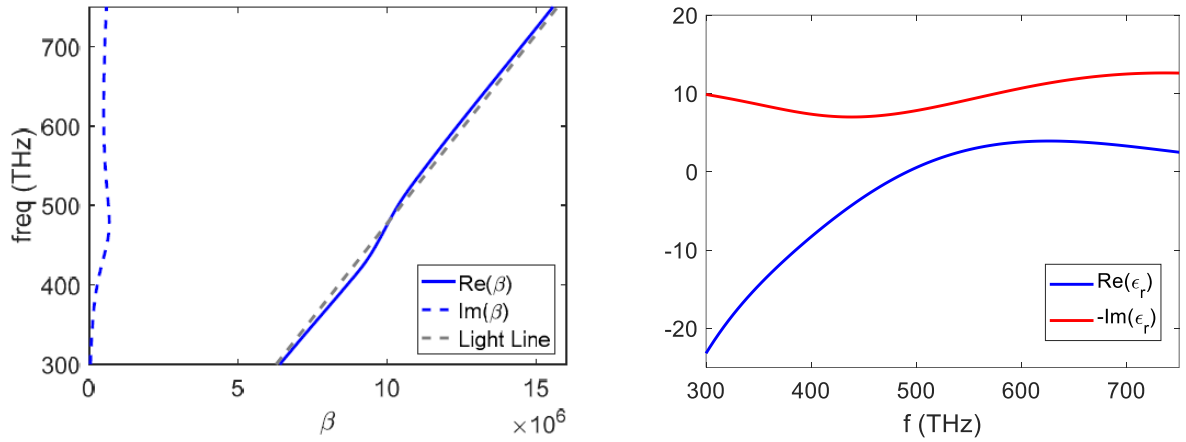

(a) (b)

Figure 3.1 (a) Propagation constant of SPP mode at Ta/air interface. The interface does not support a strong surface plasmon resonance, (b) Real and imaginary parts of permittivity of Ta. Its high losses make it impossible to get a strong enough surface plasmon resonance at Ta/air interface [19].

3.4 STT-RAM with Gold Contact Layers

Among different versions of multilayer structure presented in the literature for STT-RAM technology, it is common that noble metals such as platinum (Pt) or Au are used as part of the metal electrode contact layers placed around the essential part of MTJ stack (CoFeB/MgO/CoFeB). Typically, in the structure of STT-RAM, the noble metal layers are accompanied with nonmagnetic metal buffers consisting of Ta, and/or other materials such as Ru and W to improve the electrical performance, while in some cases Ta is used as the contact layer itself [6-8]. Since Ta cannot provide strong plasmonic performance, in Section 3.5, a silver (Ag) layer, which is a good plasmonic metal, is added in the multilayer platform used for the plasmonic nanostructure design. However, Ta introduces additional optical

losses which degrades the plasmonic performance. In addition, Ferromagnetic layers like CoFeB also introduce additional losses [83]. Therefore, later in Section 3.10.2, the multilayer structure is further simplified to Au/MgO/Au is used in the plasmonic nanostructure designed for STT-RAM defect detection, where Au contact layers are included as well as the MgO layer, where the ionizing radiation is expected to cause damage mostly.

3.5 STT-RAM Nanohole Array on Silver Film

To demonstrate nanohole array performance for detection of irradiation damage in STT-RAM multilayer, since Ta does not show good plasmonic performance, here I add Ag as the plasmonic metal supporting strong plasmonic resonance. As a result, the multilayer structure considered for the nanohole array consists of Ta (4 nm) / CoFeB (1.5nm) / MgO (2nm) / CoFeB (1.5nm) / Ta (4nm) layers (typical thicknesses for STT-RAM), all on a 300nm silver layer. The nanoholes in this design are close ended, modeled here as a PEC boundary (Figure 3.2), to simplify the design process by reducing the simulation time. Optical properties of Ag, Ta, and CoFeB are taken from the measured data provided in [84], [81], and [83], respectively. For MgO, refractive index is set to 1.73, with its extinction coefficient being zero [85]. To perform the design, Lumerical FDTD is utilized. In the simulation, a unit cell of the structure is modelled, with periodic boundary conditions and a normally incident plane wave considered as the excitation source.

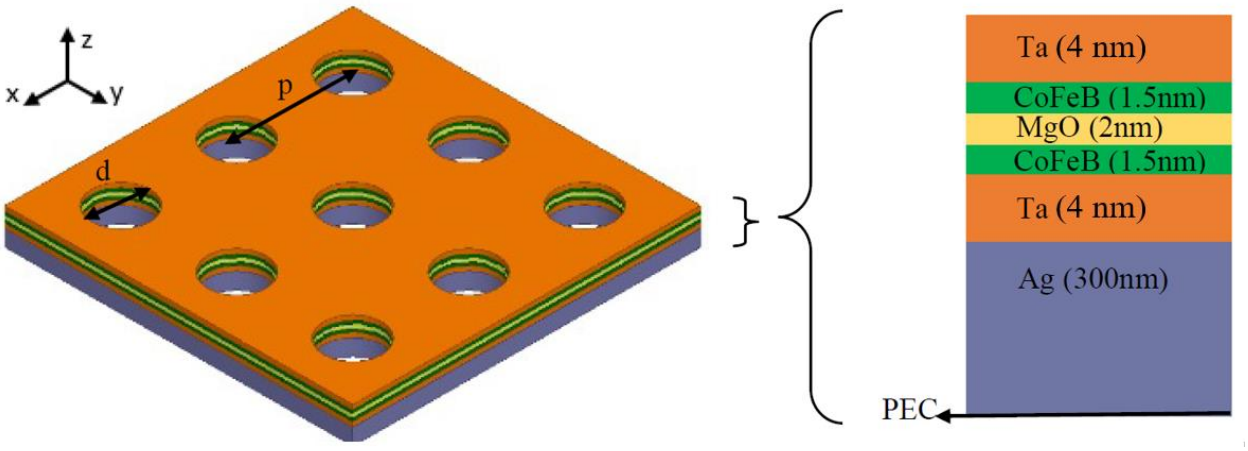

Figure 3.2 STT-RAM multilayer nanohole array structure with silver as plasmonic metal [19].

The main design parameter is the nanohole array period (p), which is used to set the resonance wavelength (λ_{res}) to the design wavelength [86]:

$$p = \frac{\lambda_{res}}{Re\{\frac{\beta_{spp}}{k_0}\}} \tag{3.4}$$

, where β_{spp} is propagation constant of (1, 0) SPP mode, propagating along the lattice vector, λ_{res} is the resonance wavelength. Based on this equation, increasing p would increase λ_{res} and vice versa. After setting the resonance wavelength to the design wavelength by tuning the value of p, the nanohole diameter (d) was used to achieve the highest resonance contrast. It should be noted that changing d slightly affects λ_{res} which is negligible.

The design wavelength for the plasmonic resonance is set to $\lambda_{res} = 780\ nm$. The choice of design wavelength is made by making a compromise to avoid larger optical losses in Ta at smaller wavelengths and to achieve high sensitivity offered by smaller wavelengths. The dimensions of the designed nanohole array are $p = 700\ nm$, and $d = 350\ nm$, for which the

reflectance spectrum has a minimum at $\lambda_{res} = 785\ nm$ as shown in Figure 3.3(a)), where SPP mode is excited. The field enhancement at the resonance, illustrated in Figure 3.4, shows that the plasmonic hotspots are located at the top surface, where the STT-RAM multilayer is placed. Therefore, the designed nanohole array is expected to show high sensitivity to the MgO layer, where irradiation defects are expected to occur.

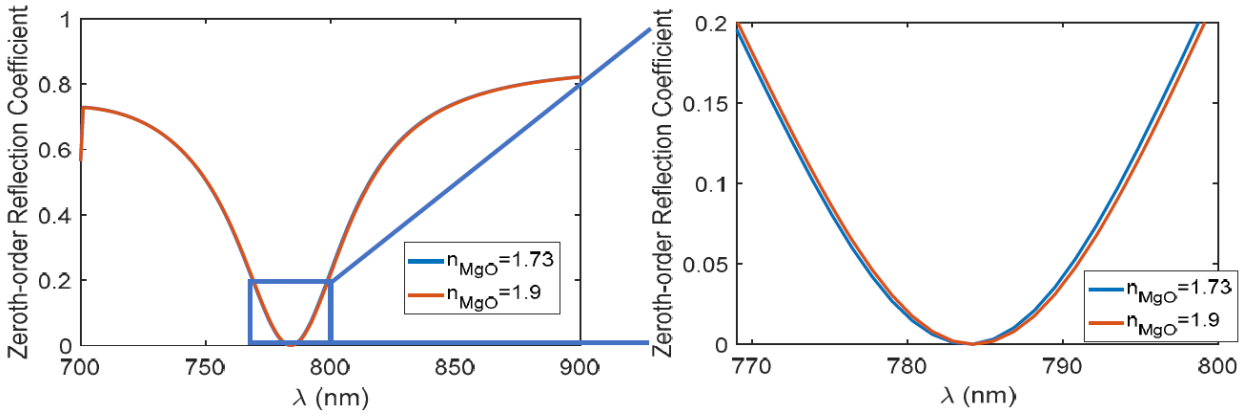

(a) (b)

Figure 3.3 (a) Zeroth-order reflection spectrum of the designed multilayer nanohole array ($p = 700\ nm$, $d = 350\ nm$), (b) zoomed view [19].

To quantify the sensitivity, an FDTD simulation is performed with the MgO refractive index changed to 1.9 (10% increase), which shows a red shift of 0.25 nm (122 GHz) in the resonance, shown in Figure 3.3(b). It should be mentioned that the relatively broad bandwidth of the designed nanohole array (FWHM of about 60nm) is because of its multilayer structure and losses in Ta and CoFeB layers while FWHM bandwidth of about 5nm can be obtained for a silver nanohole array with the same thickness.

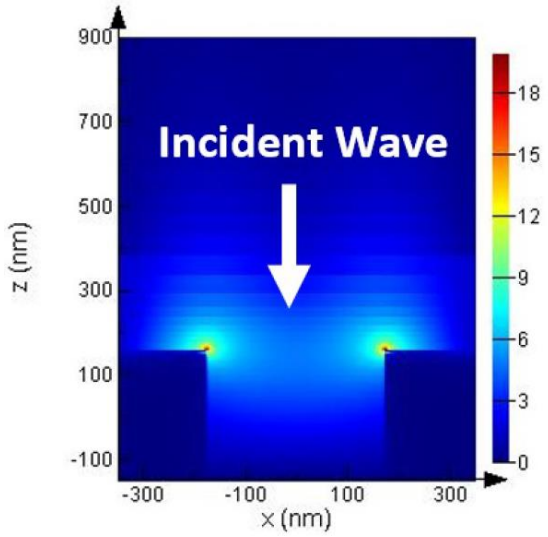

Figure 3.4 Field enhancement of the designed multilayer nanohole array ($p = 700nm$, $d = 350nm$) at plasmonic resonance wavelength ($\lambda_{res} = 785\,nm$). The plasmonic hotspots at the top surface make the structure sensitive to the refractive index changes in the MgO layer [19].

3.6 Sensing Enhancement via Dimer Nanohole Array

To increase sensitivity by creating a Fano resonance, the simple structure of dimer nanohole array is studied here. Fano resonance originates from the coupling between a broadband bright mode and a narrowband dark mode [62, 63, 72-74]. For the dimer nanohole array structure, such coupling is facilitated through the asymmetry created by moving the two nanoholes in a unit cell close to each other along the dimer axis, so the inter-hole spacing between two nanoholes in the nanohole dimer (s) becomes smaller than the spacing between on nanohole in the dimer and the closest nanohole in the adjacent unit cell along y direction (s') (Figure 3.5). Furthermore, the material difference between the upper cladding and the substrate helps enhance such coupling thus improving sensing performance, as

discussed in [87] for the case of plasmonic nanocube. However, for conventional plasmonic nanohole arrays, such material difference causes sensing degradation. It is noteworthy that there are techniques, such as substrate etching, suggested in the literature to avoid this. However, they require further fabrication steps and therefore complexity [88]. s

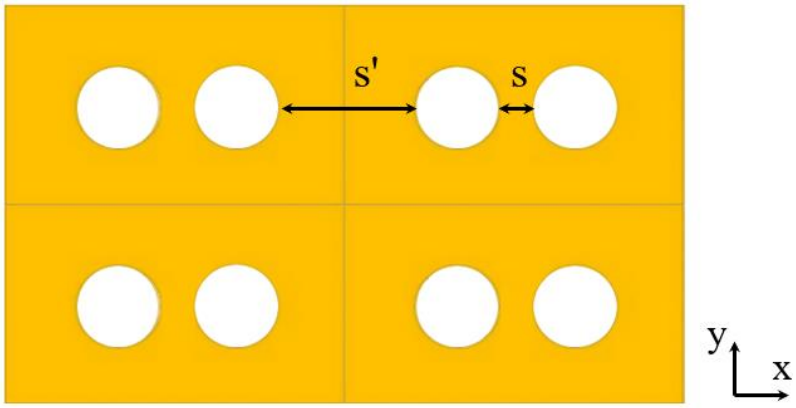

Figure 3.5 Schematic of few unit cells of dimer nanohole array showing the asymmetry along the dimer axis ($s < s'$).

The Fano resonance under study here is created from coupling between a broadband SPP mode (bright mode), and a narrowband Rayleigh-Wood Anomaly (dark mode). Rayleigh-Wood Anomaly (WA) originates from the incident wave being diffracted tangential to the surface of a periodic grating [89]. The grating formula is as follows:

$$sin(\theta_m) = sin(\theta) + \frac{m\,\lambda}{n\,p} \tag{3.5}$$

where θ is the angle of incidence, $\theta_m$is the diffraction angle for the m^{th} diffraction order, p is the grating period, λ is the wavelength in the vacuum, and n is the cladding refractive index. Based on this equation, since WA corresponds to $\theta_m = \pm 90°$, the wavelength at which WA

occurs can be calculated from:

$$\frac{m\,\lambda}{n\,p} = -\,sin(\theta) \pm 1 \tag{3.6}$$

For air cladding ($n = 1$), and for the case of normal incidence ($\theta = 0$), excitation wavelength for the first order WA mode ($m = \pm 1$) would be equal to the period (p).

It is important to note that equations above are only applicable for the case of WA modes one-dimensional (1D) grating which has periodicity only along x direction. For two-dimensional (2D) grating where periodicity is present in x and y directions, equation (3.5) can be modified into the following form:

$$sin(\theta_m) = sin(\theta) + \left| \frac{m\,\lambda}{n\,p_x}\hat{x} + \frac{m'\,\lambda}{n\,p_y}\hat{y} \right| \tag{3.7}$$

where m and m' are integers designating the mode order in x and y directions, respectively. Moreover, p_x and p_y are the grating periods along x and y directions.

It should be noted that despite the design presented in Section 3.5, for the rest of this chapter, open-ended nanoholes are considered to enable transmission of the optical wave. This is helpful, as measurement of optical transmission offers simplified optical alignment in experimental sense.

3.7 Modeling of Dimer Nanohole Array

To study the basics and design of plasmonic dimer nanohole array and its design parameters to achieve a highly sensitive Fano resonance, initially modeling of dimer nanohole array is

performed based on an Au thin film placed on quartz substrate and with air cladding. The unit cell of the structure is shown in Figure 3.6(a, b). For numerical simulations here, COMSOL Multiphysics 5.4 is utilized, which is based on finite element method (FEM), and a normally incident plane wave with its electric field polarized along y direction is considered to illuminate the array. For the COMSOL model, the material data for Au is taken from [90], and refractive index of quartz is set to fixed value of $n_{quartz} = 1.45$ as it is almost constant over the wavelength range of interest [91]. Due to symmetry of the nanohole dimer with respect to the y axis and to decrease simulation time, the modelled geometry includes only half a unit cell, and boundary conditions on the xz and yz plane side walls are set as perfect electric conductor (PEC) and perfect magnetic conductor (PMC), respectively (Figure 3.6(c)). Two periodic ports are defined to illuminate the structure from the bottom, and perfectly matched layers (PML) are defined behind the ports to avoid unwanted multiple reflections from the top and bottom boundaries. It is noteworthy to mention that it is necessary to place the PML on the air side in a farther distance from the nanostructure compared to the one on the substrate side. This is because at the resonance wavelength, the evanescent field in air extends to a larger distance, as shown in Figure 3.7.

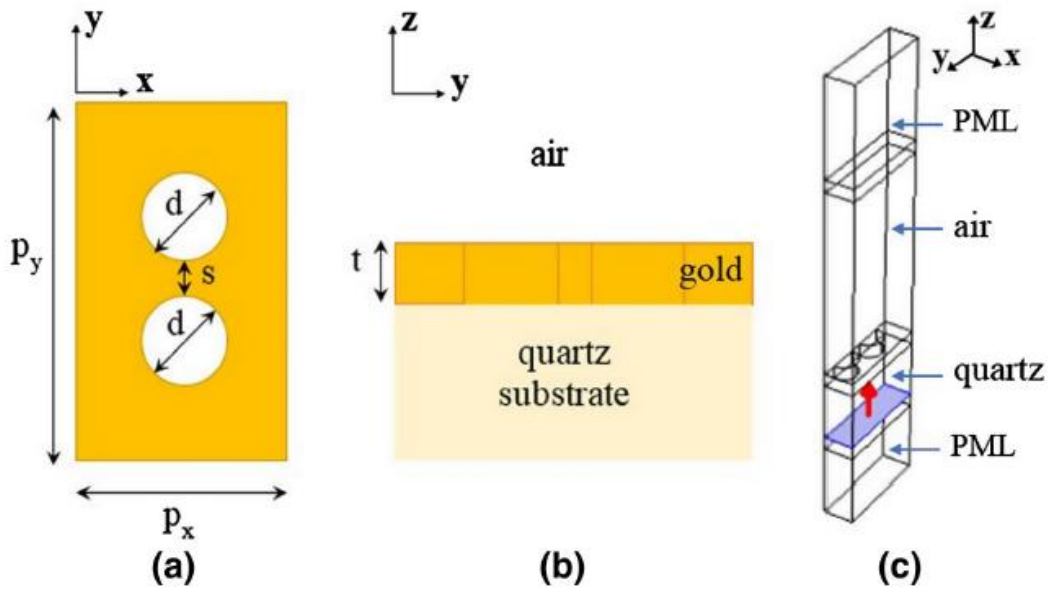

Figure 3.6 Unit cell for gold dimer nanohole array: (a) top view, (b) side view, and (c) simulation model [14].

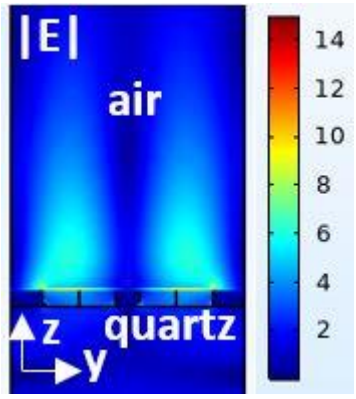

Figure 3.7 E-field distribution in yz-plane cross section of gold dimer nanohole array on quartz substrate, showing the evanescent field extends up to a larger distance in the air cladding [14].

3.8 Optical Response and Field Enhancement of Fano Resonance in Dimer Nanohole Array

To explain the design basics of dimer nanohole array to achieve the highly sensitive Fano resonance, it is helpful to first discuss the numerical simulation results for optical response of a dimer nanohole array with certain dimensions ($t = 60\ nm, d = 250\ nm, s = 75\ nm, p_x = 450\ nm, p_y = 775\ nm$). This serves as initial example to show the resonance feature in the optical spectra and its field localization and enhancement at the top surface, which facilitates its high sensitivity to refractive index changes around it. The optical response for such design is provided in Figure 3.8(a), showing a Fano resonance around $\lambda = 787\ nm$, which shows up as a local minimum in the transmission response and a local maximum in the absorption response. Since measuring the transmission is simpler in terms of optical alignment, for the design process of dimer nanohole array here, only the transmission spectrum is used.

It should be mentioned that since the main asymmetry present in the structure of the dimer nanohole array is along y direction, the two coupled modes creating the Fano resonance propagate along y axis, which are referred to as SPP(0, m') and WA(0, m), m' and m representing the mode orders. Using equation (3.5) for normal incidence, the theoretical prediction of excitation wavelength for WA(0, 1) mode is $\lambda = p_y$, resulting in $\lambda = 775\ nm$ the dimer nanohole array with the dimensions provided earlier in this section. This is very close to the Fano resonance wavelength observed in Figure 3.8(a), confirming the source of the Fano resonance is excitation of WA(0, 1) mode. In addition, it should be noted that the peak

transmission in Figure 3.8(a) refers to excitation of SPP mode of order (0, 1). This was determined through simulation of the nanostructure for a larger wavelength range and confirming that this is the SPP mode with largest resonance wavelength, which is the case for SPP(0, 1) mode based on equation and considering that $p_y > p_x$ for the current design.

The purpose of designing the dimer nanohole array here is to obtain the Fano resonance is to achieve high sensitivity at the top interface (Au/air interface), where the dielectric barrier layers of STT-RAM will be placed. Therefore, it is important to calculate the field enhancement. This is shown in Figure 3.8(b) for the dimer nanohole array under discussion, having its maximum at the Au/air interface, which is where high sensitivity is needed.

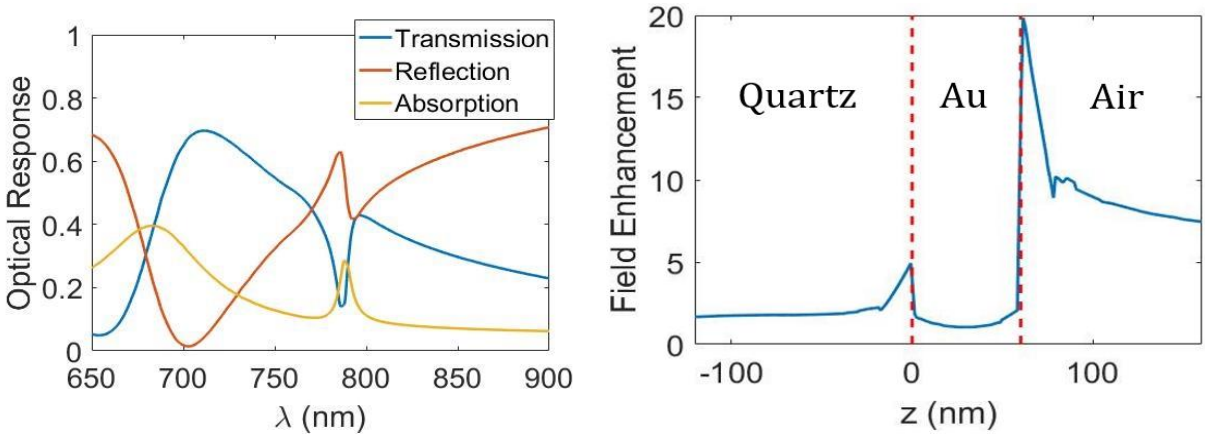

(a) (b)

Figure 3.8 (a) Optical Spectra for Au dimer nanohole array on quartz substrate showing Fano resonance around $\lambda = 787\ nm$ (a) Field enhancement of it at the Fano resonance along z axis at a major hotspot located around the dimer (dimensions are $t = 60\ nm, d = 250\ nm, s = 75\ nm, p_x = 450\ nm, p_y = 775\ nm$) [14].

To better illustrate the origin of the Fano resonance, its electric and magnetic field distributions at the resonance wavelength are shown in Figure 3.9. In specific, field

enhancement and local hot spots can be seen in Figure 3.9(a, b), where electric field magnitude distribution plots across the yz symmetry plane of the nanohole dimer and across an xy plane located at the top surface at $z = 60\,nm$ (Au/air interface) are presented. In addition, the propagation of wave along y direction can be concluded from the xy plots of E_z and H_x components which are shown in Figure 3.9(d, e). Lastly, in Figure 3.9(c, f), E_z and H_z are shown in yz plane and xy plane, respectively, to provide a better sense of the resonant mode.

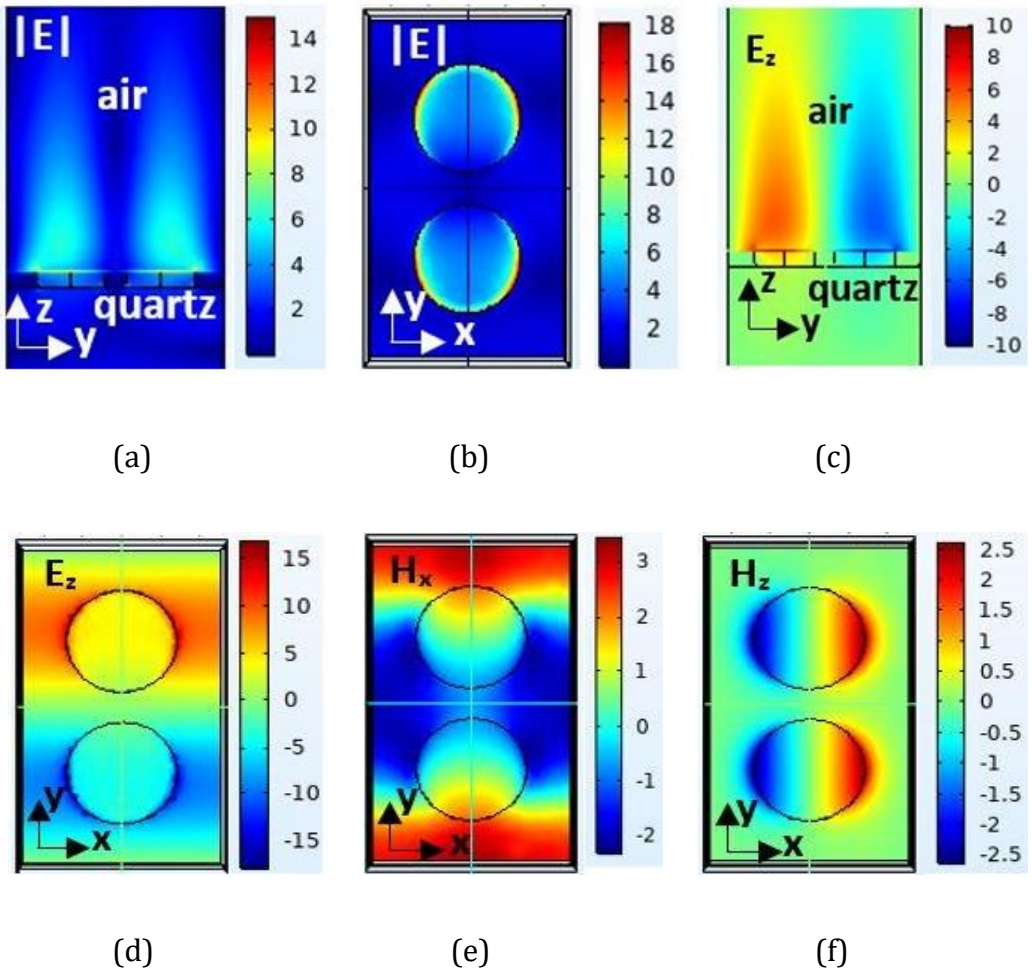

(a) (b) (c)

(d) (e) (f)

Figure 3.9 Field distributions of the excited Fano resonant mode at in Au dimer nanohole array on a quartz

substrate (dimensions are $t = 60\ nm, d = 250\ nm\ , s = 75\ nm, p_x = 450\ nm,\ p_y = 775\ nm$). The yz cross section shown is the yz symmetry plane of the nanohole dimer, and the xy plane shown is at $z = 60\ nm$ (at the top surface, i.e., Au/air interface) [14].

3.9 Effect of Changing Dimer Nanohole Array Dimensions on Fano Resonance

To design the dimer nanohole array for excitation of a strong Fano resonance mode, it is important to know how changing its dimensions affect the Fano resonance. As previously discussed in Section 3.2, for evaluation of sensing performance, higher sensitivity and smaller linewidth are desired, with sensitivity being the major factor. In this section, the focus is on studying the effect of changing each of the dimer nanohole array dimensions, while keeping others fixed, using simulation results for field enhancement, which is directly related to sensitivity. To do so, the maximum field enhancement at the Au/air interface is used for the study throughout this section (FE_{max}). In addition, the depth of the resonance feature (resonance contrast or magnitude) in the transmission spectrum is discussed. The resonance contrast is important in experimental sense, since it is a measure for resonance strength, quantifying the visibility of the resonance feature in the optical transmission spectrum as well as showing the efficiency of the resonant mode excitation. The dimer nanohole array considered here is based an Au film placed on a quartz substrate and with air as the top layer, similar to those discussed in Sections 03.7 and 3.8 (Figure 3.6). To

simplify the study, the diameters of the two nanoholes in the nanohole dimer are set to be equal in all cases. In other words, the nanohole dimer is symmetric with regards to the xz cross sectional plane passing center of the unit cell.

The impact of changing the array period in the direction along the dimer axis (p_y) while keeping other dimensions fixed is shown in Figure 3.10. It is clear that a change in p_y mainly affects the resonance wavelength, as it directly changes the criteria for excitation of WA(0, 1), provided in equation (3.6). An increase in p_y increases the resonance wavelength and vice versa. Moreover, red shifting of the SPP(0, 1) mode is observed following an increase in p_y, which is in accordance with the theoretical expectation based on equation (2.48). Increasing p_y results in a stronger Fano resonance (deeper resonance feature as well as larger FE_{max}). This is because larger p_y leads to further asymmetry created along the y direction, since nanoholes in a unit cell become farther from the ones in the unit cell adjacent to them along y direction.

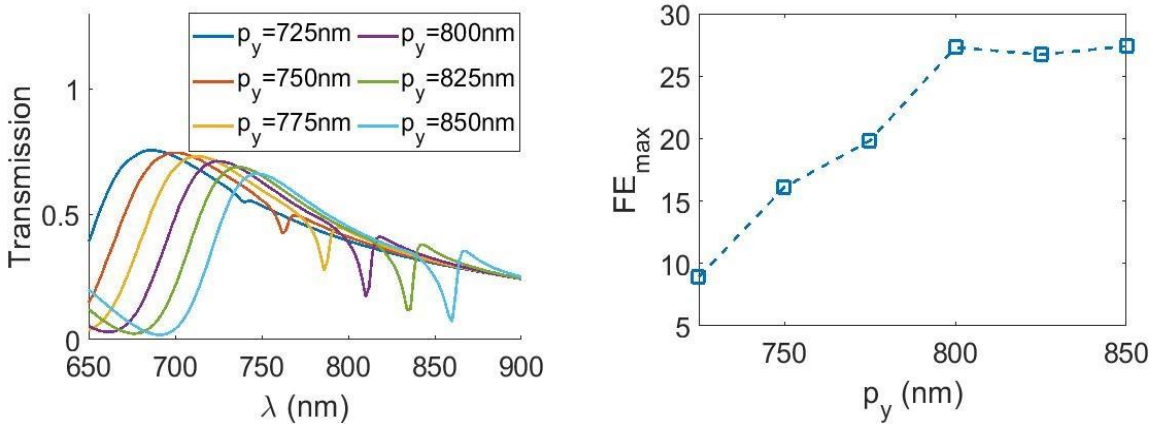

(a) (b)

Figure 3.10 Study of effect of changing p_y on Fano resonance of Au dimer nanohole array on quartz substrate with air cladding: (a) Optical transmission spectrum and (b) Maximum field enhancement (Dimensions are $t = 60\ nm, d = 250\ nm, s = 100\ nm, p_x = 450\ nm$) [14].

While changing the p_y significantly affects the resonance wavelength, changing the period in x direction (p_x) has little to no effect on it (Figure 3.11). This is because the main decision maker for the Fano resonance wavelength is WA(0, 1), which propagates along y direction thus being independent from the array period in x direction. On the other hand, decreasing p_x helps enhance the Fano resonance strength, increasing the resonance contrast as well as its sharpness, as shown in Figure 3.11(a). Also, the FE_{max} data plotted in Figure 3.11 (b) is in accordance with this, showing its overall trend as increasing when p_x becomes smaller, meaning stronger resonance. This is reasonable, since a decrease in p_x, meaning larger nanohole-to-metal area ratio, facilitates more coupling of optical power to WA(0, 1) mode, through increasing the optical transmission of the broadband SPP(0, 1) mode. It should be noted that the irregularities in the overall trend of FE_{max} in Figure 3.11(b) is due to the sampling error originating from the wavelength step selected for the simulations and can be eliminated by decreasing the wavelength step size. Here, the wavelength step size is remained relatively coarse to reduce the simulation time.

It is noteworthy to mention that the extra dip showing up at $\lambda = 700\ nm$ for the case of $p_x = 600\ nm$ is related to the WA(1, 1) mode at the Au/quartz interface, which is close to the theoretical expectation, $\lambda = 688\ nm$, obtained from equation (3.7). Similar explanation applies to the resonance feature at $\lambda = 670\ nm$ for $p_x = 550\ nm$.

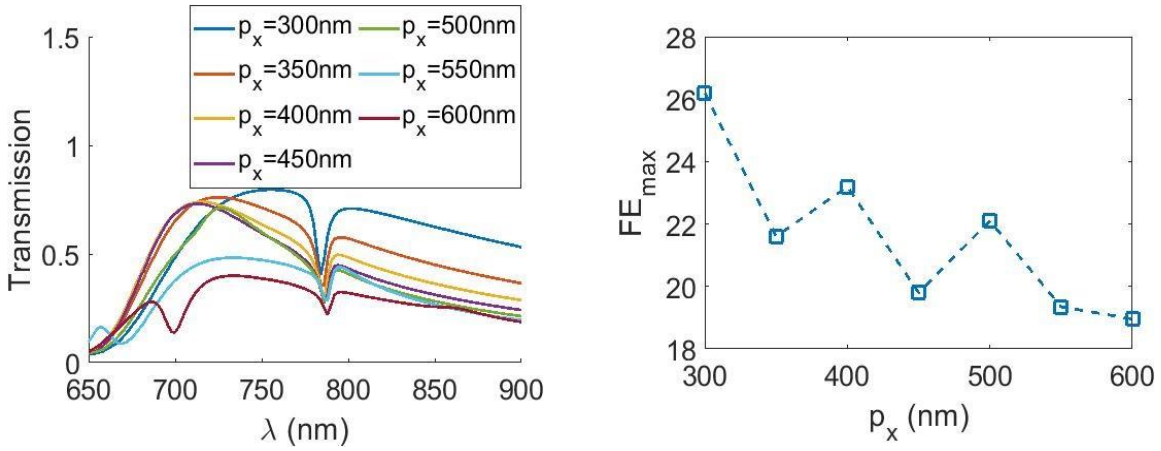

(a) (b)

Figure 3.11 Study of effect of changing p_x on Fano resonance of Au dimer nanohole array on quartz substrate with air cladding: (a) Optical transmission spectrum and (b) Maximum field enhancement (Dimensions are $t = 60\ nm, d = 250\ nm, s = 100\ nm, p_y = 775\ nm$) [14].

After studying how changing the period affects the Fano resonance supported by dimer nanohole array, the effect of changing the nanohole diameter (d) and the inter-hole spacing (s) between the two nanoholes composing the nanohole dimer in a unit cell is investigated. Based on the simulation results presented in Figure 3.12 and Figure 3.13, one can observe that changes in d and s have a correlated effect on the resonance strength of the Fano mode. Such correlation suggests that for each nanohole diameter value, there is a specific inter-hole spacing for the dimer that leads to the Fano resonance with largest strength. For example, among the cases presented in Figure 3.12 and Figure 3.13, the strongest Fano resonance in terms of maximum field enhancement and resonance sharpness happens for the two cases of $s = 100\ nm, d = 225\ nm$ and $s = 75\ nm, d = 250\ nm$.

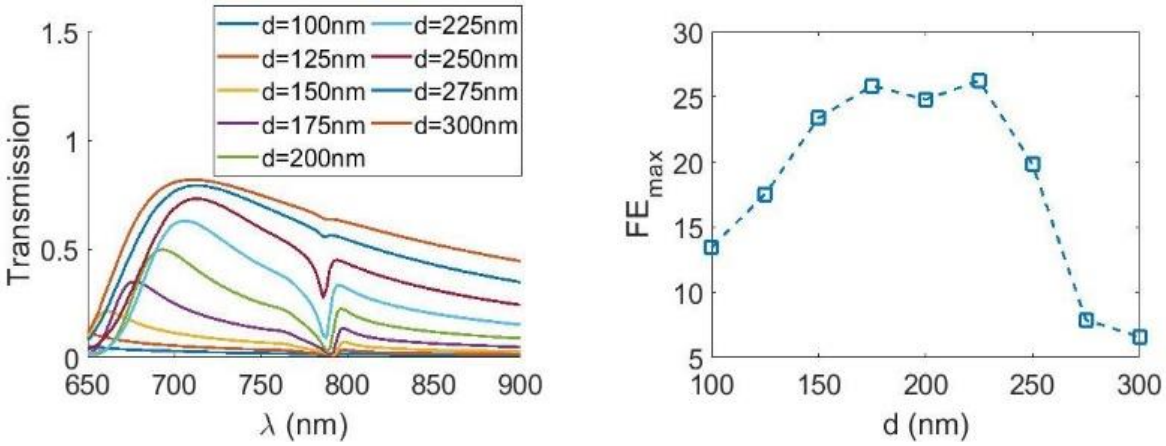

(a) (b)

Figure 3.12 Study of effect of changing nanohole diameter on Fano resonance of Au dimer nanohole array on quartz substrate with air cladding: (a) Optical transmission spectrum and (b) Maximum field enhancement (Dimensions are $t = 60\ nm, s = 100\ nm, p_x = 450\ nm, p_y = 775\ nm$) [14].

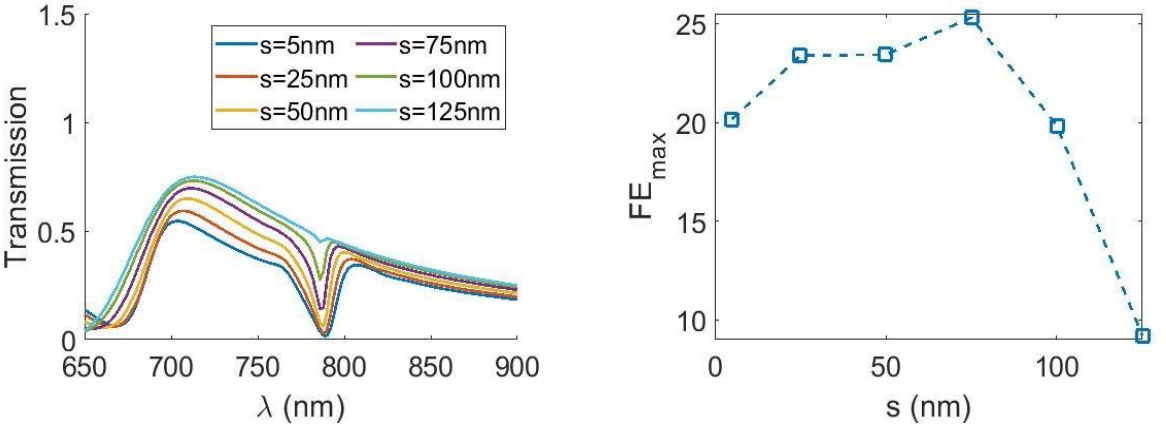

(a) (b)

Figure 3.13 Study of effect of changing the dimer inter-hole spacing on Fano resonance of Au dimer nanohole array on quartz substrate with air cladding: (a) Optical transmission spectrum and (b) Maximum field enhancement (Dimensions are $t = 60\ nm, d = 250\ nm, p_x = 450\ nm, p_y = 775\ nm$) [14].

Further simulations confirm that when p_y is kept constant, for a larger value of nanohole diameter a smaller inter-hole spacing is needed to achieve the strongest Fano resonance. For example, for dimer nanohole array with dimensions set as "$t = 60\ nm, p_x = 450\ nm, p_y = 775\ nm$", for the case of $d = 300\ nm$ the inter-hole spacing of $s = 5\ nm$ results in strongest Fano resonance, while for $d = 250\ nm$, inter-hole spacing of $s = 75\ nm$ creates the strongest resonance. This is because with p_y being constant, a larger nanohole diameter would need a smaller inter-hole spacing to create as strong of an asymmetry between the inter-hole spacings inside a unit cell and across adjacent cells in y direction (s and s' in Figure 3.5).

The thickness of the Au layer can also affect the Fano resonance strength, as it determines the extent of coupling of the incident power to the SPP(0, 1) mode and WA(0, 1) as a result. The simulation results for sweeping the value of Au thickness (t) are shown in Figure 3.14. It can be observed that as the Au thickness becomes closer to the Au skin depth ($\sim 26\ nm$ at $\lambda = 780\ nm$). This is because for such small thicknesses, the Au layer cannot act as a good metal. On the other hand, for $t = 150\ nm$ and larger the Fano resonance becomes weaker, having smaller resonance sharpness and contrast as the optical transmission gets smaller. It is important to note that the Au thickness that can offer the strongest Fano resonance can be increased if one increases the nanohole diameter, as it helps increase the optical transmission of the broadband SPP(0, 1) mode thus exciting the WA(0, 1) more efficiently.

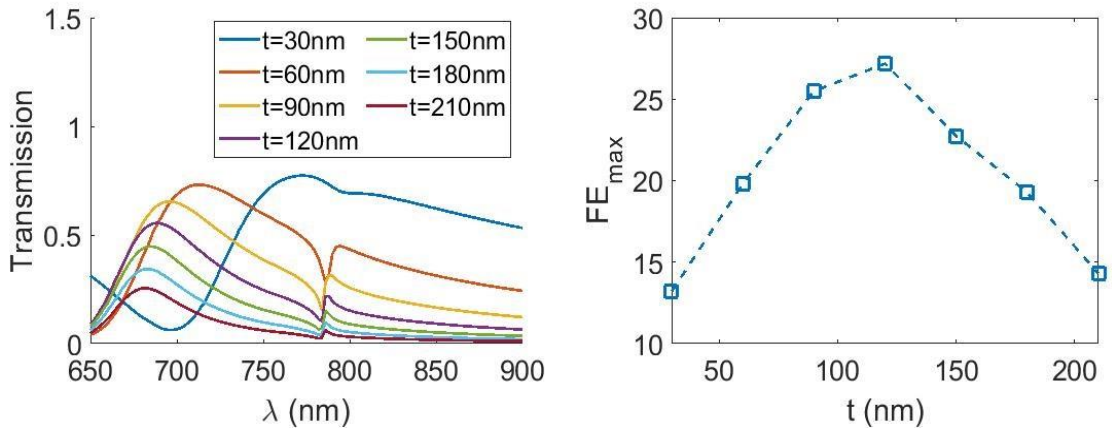

(a) (b)

Figure 3.14 Study of effect of changing the dimer inter-hole spacing on Fano resonance of Au dimer nanohole array on quartz substrate with air cladding: (a) Optical transmission spectrum and (b) Maximum field enhancement (Dimensions are $t = 60\ nm, s = 100\ nm, d = 250\ nm, p_x = 450\ nm, p_y = 775\ nm$) [14].

3.10 Sensing Performance of Dimer Nanohole Array

To evaluate sensing performance of dimer nanohole array and compare it with conventional nanohole array structure, it is helpful to study its sensing ability with regards to changes in the top cladding/cover material, which is known as bulk sensing. This facilitates comparison of sensing ability of dimer nanohole array with the current research in the literature. Such study is presented in the first part of this section. Later in this section, ability of nanohole array designed in a simplified STT-RAM multilayer to detect changes in its ultrathin dielectric layer is investigated and compared to sensing performance of conventional nanohole array. To quantify the sensing ability of dimer nanohole array structure, sensitivity and FOM parameter, defined in Section 3.2, are estimated through numerical simulations

throughout this section.

3.10.1 Bulk Sensing

For evaluation of dimer nanohole array regarding it bulk sensing performance, the top cladding material is set to water, as it is the most common case for nanohole array bulk sensing in the literature. The dimer nanohole array structure multilayer is similar to Figure 3.6, except for its top cover material which is water. Moving from the design presented in previous sections for air cladding ($n = 1$) to the one intended for water cladding ($n = 1.33$) here, it is important to note that the increase in cladding refractive index increases the excitation wavelength of the WA(0, 1) involved in the Fano resonance. To tune the resonance wavelength back to its previous value, one can reduce p_y. Also, nanohole array diameter and dimer inter-hole spacing are tuned to achieve a sharp resonance. As a result, the selected dimensions for the dimer nanohole array are $t = 60\ nm, s = 20\ nm, d = 200\ nm, p_x = 450\ nm, p_y = 520\ nm$.

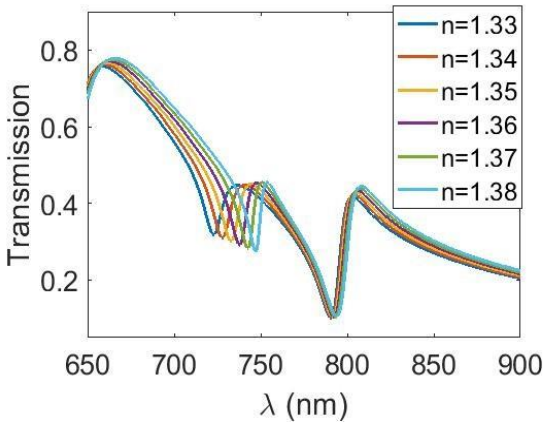

(a)

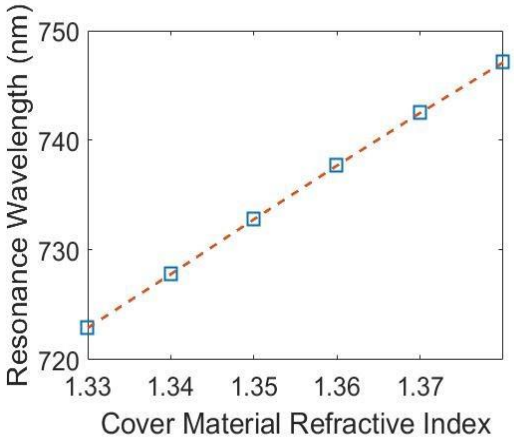

(b)

Figure 3.15 Evaluation of bulk sensing performance of dimer nanohole array in Au film on quartz substrate, with water as its top cladding: (a) Optical transmission spectrum and (b) Plot of resonance wavelength of the Fano resonance with shorter resonance wavelength versus refractive of the top layer (Dimensions are $t = 60\ nm, s = 20\ nm, d = 200\ nm, p_x = 450\ nm, p_y = 520\ nm$) [14].

To evaluate bulk sensing of the designed dimer nanohole array, its optical transmission spectrum is obtained through simulation for different value of cladding refractive index (Figure 3.15(a)). The results show two Fano resonances in the wavelength range of study ($\lambda = 723\ nm$ and $\lambda = 790\ nm$ for n= 1.33). The two resonances are a result of coupling between SPP(0, 1) and WA(0, 1) modes. The Fano mode with larger resonance wavelength is due to excitation of modes at the Au/quartz interface, and the one with smaller resonance wavelength is related to modes excited at the Au/air interface. Hence, the latter is much more sensitive to changes in the water cladding, showing much larger resonance shift as the cladding material changes. Therefore, it is the resonance for which the sensing performance is estimated. It is noteworthy to mention that in this design, the two Fano resonances localized at cladding side and the substrate side have their wavelengths closer to each other than the designs with air cladding presented in the previous sections. The reason is that for the case of water cladding, the refractive index of the cladding is closer that of the quartz substrate.

Sensitivity is defined as resonance wavelength shift divided by the refractive index change, based on equation (3.1). Therefore, one can plot the resonance wavelength versus refractive index and calculate its slope to obtain sensitivity. Such plot is shown Figure 3.15(b) for the Fano resonance with shorter wavelength for the designed structure, from which sensitivity

is calculated to be $S = 486\, nm/RIU$, which is larger than the highest sensitivity value reported in [77] for heptamer nanohole array ($S = 400\, nm/RIU$). Considering the 12 nm linewidth of the Fano resonance under study, the dimer nanohole array is calculated to have FOM of 40.5 regarding bulk sensing, which is about 70% larger than highest FOM reported for heptamer nanohole array ($FOM = 23.8$) [77]. It is important to highlight that in addition to having superior sensing ability compared to heptamer nanohole array, dimer nanohole array has imposes less fabrication complexity, since it allows larger inter-hole spacing, resulting in increasing the minimum feature size.

To compare the sensing performance of dimer nanohole array with conventional nanohole array, FOM values are compared, as FOM combines wavelength shift with resonance sharpness and plays a role in resolution of refractive index sensing. Among studies in the literature on nanohole arrays designed for visible wavelengths [80, 92-97], the highest reported value for FOM is 40 [97]. Even though the dimer nanohole array design here is not optimized, it has a slightly larger FOM. In addition, the FOM reported in [97] is for a nanohole array with substrate etching to facilitate further overlap of the surrounding water cladding with the plasmonic field and increase sensitivity as a result. Therefore, to have a better comparison, dimer nanohole array bulk sensing should be compared with the nanohole array reported in [96] which has a similar substrate and has FOM of 23.3. Based on this, dimer nanohole array facilitates more than 70% improvement.

In addition, other types of nanostructure shapes based on SPP sensing are presented in the literature, including nanoslit array [98] ($FOM = 33.9$), elliptic nanohole array [99]

(FOM~16.5), and array of overlapped double holes [55] (FOM~16.3). Considering these values, it is concluded that the dimer nanohole array design presented here provides improvement in sensing.

3.10.2 STT-RAM Ultrathin Dielectric Barrier Sensing

As previously discussed, the goal of this chapter is to design plasmonic nanostructures in STT-RAM multilayer to detect possible irradiation changes in its ultrathin dielectric layer (MgO). Therefore, performance of dimer nanohole array for sensing such changes is evaluated here. For this purpose, a simplified STT-RAM multilayer of Au ($5\,nm$) / MgO ($10\ nm$) / Au ($60\,nm$) placed on a quartz substrate and surrounded by air is considered. It should be noted that the MgO layer thickness increased to 10 nm to reduce simulation time by relaxing the requirement for small enough mesh size to achieve accurate results. Furthermore, thickness of the bottom Au layer is set to 60 nm, which is much larger than its skin depth (~$26\,nm$ at $\lambda = 780\,nm$), to make it capable of supporting a strong plasmonic resonance. The rest of the design dimensions of the dimer nanohole array considered here are $s = 75\,nm, d = 250\,nm, p_x = 450\,nm, p_y = 775\,nm$. To calculate the sensitivity, simulations are performed while varying the refractive index value of the dielectric layer from $n = 1.3$ to n=2.1 in increments of 0.2 (Figure 3.16(a)), where a resonance linewidth of 11 nm can be observed. Sensitivity to such changes is calculated from the slope of resonance wavelength versus dielectric layer refractive index plot, shown in Figure 3.16(b). To estimate the resonance wavelength shift due to radiation-induced changes in the dielectric MgO layer, one needs to multiply the sensitivity value by the expected

refractive index change of MgO. Since no dose test have been established for MgO, here the data available for silica is used to make an estimate. Based on the date presented in [100], refractive index change of ~0.05 (3.5%) occurs in silica when undergoing ion beam radiation (Br ions and $\sim 46\, krad$ dose level). Using the same percentage change for MgO refractive index, resonance shift of 0.3 nm is estimated. It is important to mention, that different dose of radiation and different ion type would cause different result [101].

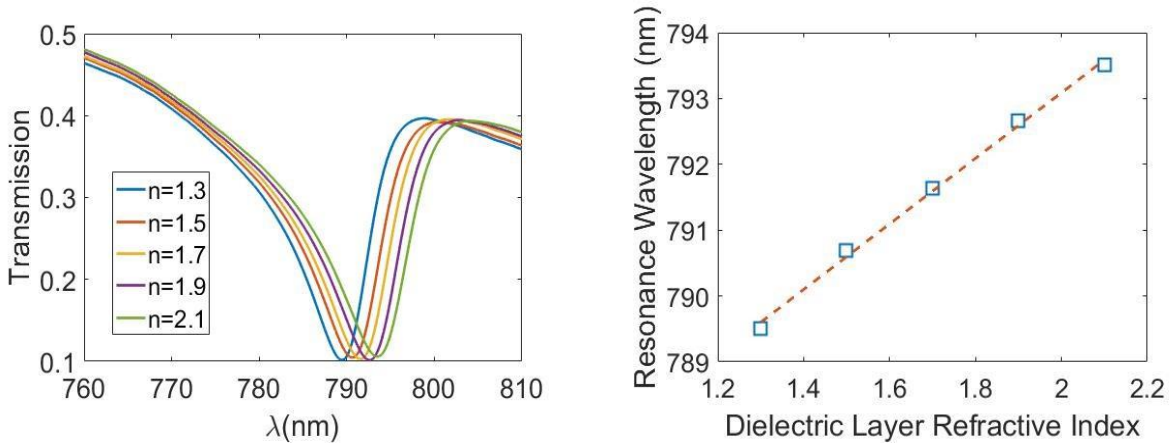

(a) (b)

Figure 3.16 Evaluation of sensing performance of dimer nanohole array regarding changes in the ultrathin dielectric layer, for a simplified STT-RAM multilayer of Au (5 nm) / MgO (10 nm) / Au (60 nm) placed on a quartz substrate and surrounded by air: (a) Optical transmission spectrum and (b) Plot of resonance wavelength of the Fano resonance versus refractive of the dielectric layer (Dimensions are $s = 75\, nm, d = 200\, nm, p_x = 450\, nm, p_y = 775\, nm$) [14].

To show the improvement achieved in sensing of MgO layer by using dimer nanohole array, compared to conventional nanohole array, a nanohole array is also designed for similar resonance wavelength and in the same multilayer platform. The nanohole diameter and

period for such design are $d = 400\,nm$ and $p = 750\,nm$, respectively. The design dimensions are chosen to achieve excitation of first order SPP mode at the air-Au interface at around $\lambda = 790\,nm$ wavelength, and to obtain around the same resonance contrast as the Fano resonance supported by the dimer nanohole array shown in Figure 3.16(a). Keeping the resonance contrast the same (Figure 3.17), the two nanostructures are compared based on their FOM values thus comparing refractive index resolution of their sensing, based on equation (3.3).

To make a fair comparison, it is important to consider differences in the percentage area of the unit cell where MgO layer is present in each nanostructure. This is done by normalizing the calculated sensitivity to the MgO-per-unit cell area defined as $(1 - 2A_{\text{nanohole}}/A_{unit\ cell})$ for dimer nanohole array and $(1 - A_{\text{nanohole}}/A_{unit\ cell})$ for conventional nanohole array. Calculations based on the simulation results shown in Figure 3.16 and Figure 3.17 show that improvements of 30% and 70% are achieved in normalized sensitivity and normalized FOM values, respectively, when using dimer nanohole array.

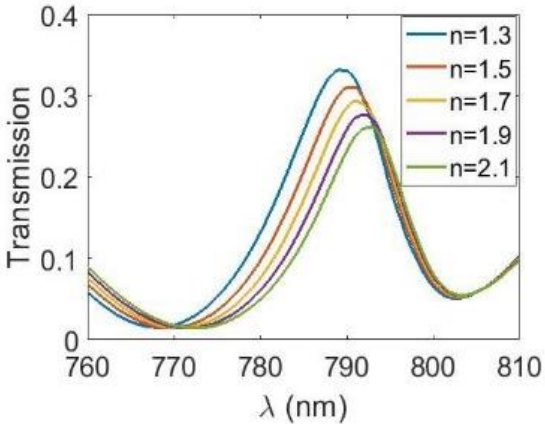

Figure 3.17 Evaluation of sensing performance of conventional nanohole array regarding changes in the

ultrathin dielectric layer, for a simplified STT-RAM multilayer of Au (5 nm) / MgO (10 nm) / Au (60 nm) placed on a quartz substrate and surrounded by air: Optical transmission spectrum for different refractive index values of dielectric layer (Dimensions are $d = 400\ nm, p = 750\ nm$) [14].

3.11 Summary and Conclusion

In summary, we discussed design of plasmonic nanohole array in STT-RAM multilayer structure, to provide a highly sensitive means capable of detecting possible irradiation damages in the STT-RAM ultrathin dielectric barrier. In addition, study of dimer nanohole array for achieving a Fano resonance with improved sensing performance was performed. Comparisons were made between dimer nanohole array and conventional nanohole array regarding their sensing ability. For bulk sensing of dimer nanohole array, sensitivity of 846 nm/RIU and FOM of 40.5 were demonstrated though theoretical simulation, which are both larger than the typical values presented in the literature for conventional nanohole array structure. Regarding detection of changes in the ultrathin dielectric layer, overall improvement of 70% is shown when using dimer nanohole array, and resonance wavelength shift due to radiation-induced changes was estimated to be 30 nm.

Chapter 4

Adhesion Layer Effect on Resonance of Plasmonic Nanostructures

4.1 Introduction

As discussed in earlier in this dissertation, plasmonic nanostructures can provide strong field enhancement, offering high sensitivity when being used in sensing applications. The most used plasmonic metals are gold and silver. As they are noble metals, it is necessary to use an adhesion layer so that a firm bonding between the plasmonic metal and the dielectric substrate can be enabled. To address this, traditionally, metals such as titanium (Ti), chromium (Cr), and tantalum (Ta) can be used as adhesion material, with the first two being the most common in the literature. These metals, however, have significant losses (large extinction coefficient), which creates resonance damping showing up as broadening of the plasmonic resonance, meaning smaller FOM (based on equation (3.2)), and reduction of its contrast (depth) [6, 21-24, 31, 32, 102]. It is important to note that sensitivity, as defined in equation (3.1), is not significantly affected by the adhesion layer losses. However, the resonance broadening and contrast reduction result in lower signal-to-noise ratio in measurements, decreasing the sensing resolution (equation (3.3)) [103].

To avoid the sensing degradation caused by lossy adhesion materials, efforts have been made in the literature including papers suggesting use of oxides such as TiO_2, Cr_2O_3, and ITO [24-27]. Alternatively, using a molecular linker, which covalently binds the plasmonic metal on dielectric substrate, is demonstrated to be a non-damping adhesion layer option [28, 29]. The downside with regards to using a molecular linker is that its deposition time is required to be long (3 hours to 3 days), as the adhesion performance increases for a longer deposition time [28]. Another way to avoid the excess losses introduced by metallic adhesion layers in plasmonic nanostructures is to use a selective deposition technique to reduce the overlap between the adhesion layer and the plasmonic hotspots of the structure. This is demonstrated in [30] for nanogap array structure. While this method helps diminish the effect of adhesion layer losses on the plasmonic performance, it requires additional alignment steps in the process of fabrication.

In this chapter, MgO is suggested and tested as an alternative low loss adhesion layer. The effect of different adhesion layers on the plasmonic resonance of different nanostructures is studied through numerical simulations and compared to the case of MgO adhesion layer. This is done through initial simulations where bulk material properties are considered for the adhesion layers (Section 4.2). However, optical properties of thin films can be significantly different from bulk materials because of larger amount of scattering at the particle boundaries [104-110]. Therefore, thin-film material data for Ta and MgO for such simulations is obtained through ellipsometry measurements (Section 4.3), used in a second set of simulations to provide an experimental estimate, and compared to the cases of other adhesion materials presented in the literature (Section 4.4). The results show that using an

MgO adhesion layer has a negligible effect on plasmonic resonance. In addition, MgO is tested mechanically regarding its adhesion performance, showing its ability to create a strong bond between substrate and the plasmonic metal. Detailed information on deposition of samples and utilizing them for mechanical testing is provided in Section 4.5.

4.2 Adhesion Layer Effect on Nanostructures Plasmonic Resonance Considering Bulk Properties

Material properties of the adhesion layer used in plasmonic nanostructures can negatively affect the plasmonic resonance, causing broadening, or reduction of contrast in the resonance spectral feature. Here, initial simulations, where bulk material properties for adhesion materials are considered, are performed for different adhesion layers. Such simulations are used to show that MgO has a potential to be used as a low-loss adhesion material, in terms of its optical properties. Also, the results provide an estimate of effect of Ta adhesion layer on plasmonic performance. Comparisons with Ti and Cr, the most common adhesion metals, are made using the simulation results. For this purpose, different plasmonic nanostructures are studied, as the extent of adhesion layer effect on plasmonic resonance also depends on the nanostructure geometry and field distribution of the excited plasmonic mode, which determines the overlap of hotspots with the adhesion layer [30].

The nanostructures used for the study here are dimer nanohole array, nanohole array, nanodisk array, and bowtie slot antenna array [14, 61, 111, 112], shown in

(c) (d)

Figure 4.1. The designs are based on a 60 nm Au film, except for the case of nanodisk array where a 20 nm Au film is considered to achieve a relatively sharp resonance for a smaller period thus reducing the simulation time. For all cases, the Au film is placed on quartz (SiO_2) substrate ($n = 1.45$), the top cladding material is air, and a plane wave normal incidence (propagation along z direction) polarized along y direction is assumed with resonance observed in optical transmission spectral response. Design process is performed using finite element method (FEM) simulations through which the dimensions are set to achieve a resonance wavelength around $\lambda = 710\ nm$. In the simulations, Au material data from [90] is used and the Au film is assumed to be fully etched following the nanostructure geometry in all cases.

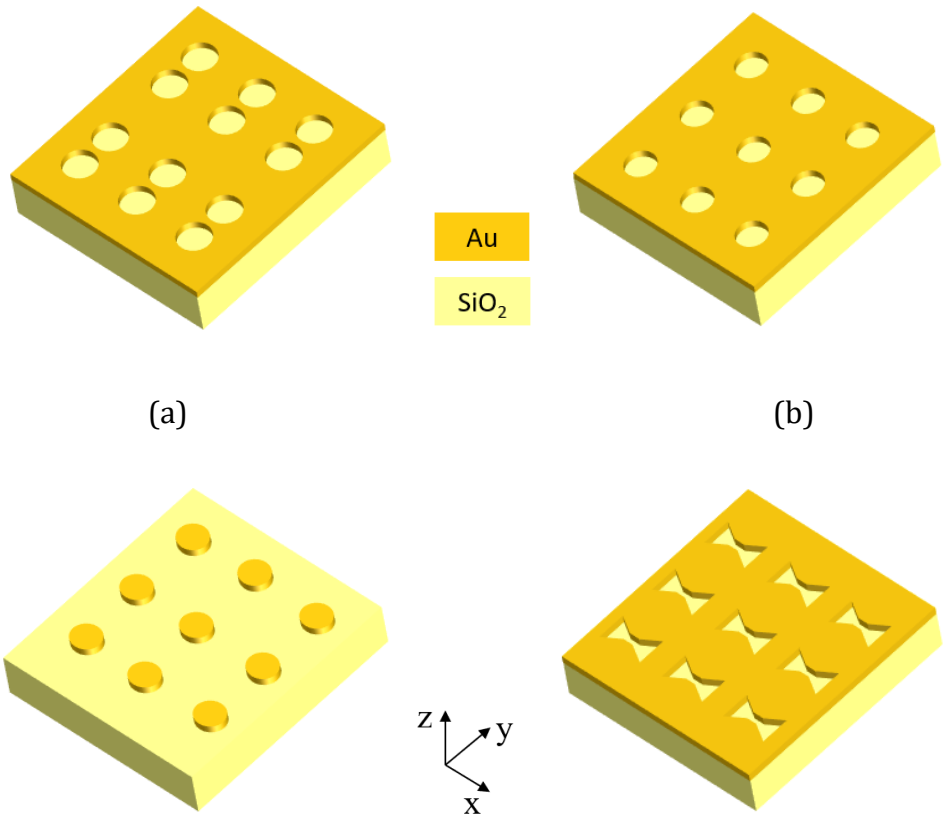

(c) (d)

Figure 4.1 Plasmonic nanostructures designed for study of adhesion layer effect on plasmonic resonance: (a) Dimer nanohole array, (b) Nanohole array, (c) Nanodisk array, (d) Bowtie slot antenna array.

The dimer nanohole array and dimer nanohole array structures are designed to support propagating plasmonic modes, and their designs are done based on the discussions presented in Chapter 3. The dimer nanohole array supports a WA(0, 1) mode coupled with SPP(0, 1) mode, similar to the designs presented in Chapter 3, with its field enhancement peak at the Au/air interface. The designed nanohole array has the SPP(0, 1) mode at the Au/substrate interface excited. Hence, it has its maximum field enhancement at the Au/SiO_2 interface. For nanodisk array, diameter of nanodisk is mainly used to set the resonance wavelength to the design wavelength. It is noteworthy to mention that increasing the thickness of Au film decreases the resonance wavelength. Therefore, for a larger Au film thickness, a larger nanodisk diameter is needed. However, resonance broadening occurs when increasing the Au thickness due to coupling between the nanodisks in adjacent unit cells. This can be improved via increasing the array period. The excited mode is an LSPR mode, forming a dipole-like field distribution across the nanodisk diameter [113]. For design of bowtie slot antenna array, perimeter of bowtie slot is changed to tune the resonance wavelength. The excited plasmonic mode mainly originates from LSPR, with its maximum field enhancement in small gap region of the antenna [114]. It should be noted that the LSPR modes excited in the designed nanodisk array and bowtie slot array have a larger field enhancement at the Au/ SiO_2 interface due to larger refractive index of SiO_2 compared to ai.

Dimensions of designed nanostructures obtained through simulations are shown in Figure 4.2, where the top view for unit cell of each nanostructure is depicted. In terms of resonance spectral feature, the resonances supported by the dimer nanohole array and nanodisk array show up as a resonance dip in their transmission spectra (solid lines without markers in Figure 4.3(a, d)). For the cases of nanohole array and bowtie slot antenna array, however, plasmonic resonance at the design wavelength creates a resonance peak in their transmission spectra (solid lines without markers in Figure 4.3(b, c)).

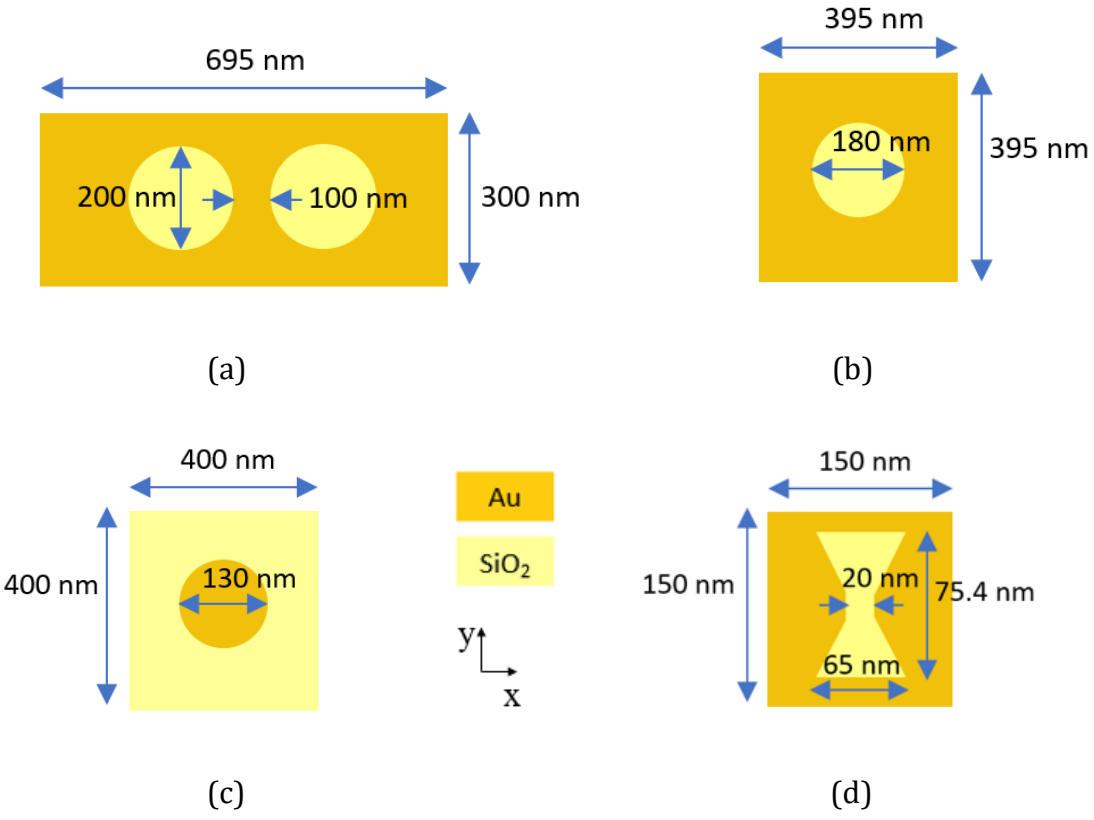

Figure 4.2 Unit cell top view schematic showing the dimensions of the designed plasmonic nanostructures: (a) Dimer nanohole array, (b) Nanohole array, (c) Nanodisk array, (d) bowtie slot antenna array [32].

As discussed above, depending on the geometry and dimensions, each of the four designed

nanostructures support excitation of specific type of plasmonic resonance at the design wavelength with certain field enhancement properties. Therefore, depending on the overlap of their field distribution with adhesion layer, material properties of adhesion layer affect their resonance differently. To study the effect of adhesion layer, simulations are done with adhesion layer of $5\,nm$ thickness placed between the SiO_2 substrate and the Au film, considering different adhesion materials. The adhesion layer is assumed to be fully etched in all cases. Adhesion layers of Cr, Ti, Ta, and MgO are studied, where bulk material properties are used. The bulk material data for Cr, Ti, and Ta is taken from [81], and for MgO is taken from [85]. Spectral response of the designed plasmonic nanostructures obtained from such simulations are presented in Figure 4.3.
From these plots, resonance broadening, in terms of linewidth increase, and reduction resonance contrast (or magnitude) are calculated in percentage. The calculated values are shown in two separate graphs in Figure 4.4. The linewidth calculated for the nanohole array and the bowtie slot array is defined as full width at half maximum (FWHM). For nanodisk array, linewidth is defined as the full width at half depth (FWHD). On the other hand, for the case of dimer nanohole array, since the resonance under study is a Fano resonance, linewidth is the difference between the wavelength of resonance and that of the closest local maximum in its transmission spectrum. In all cases, resonance magnitude is calculated from the difference between value of transmission local maximum (or minimum), occurring at the resonance wavelength, and that of its closest local minimum (or maximum).

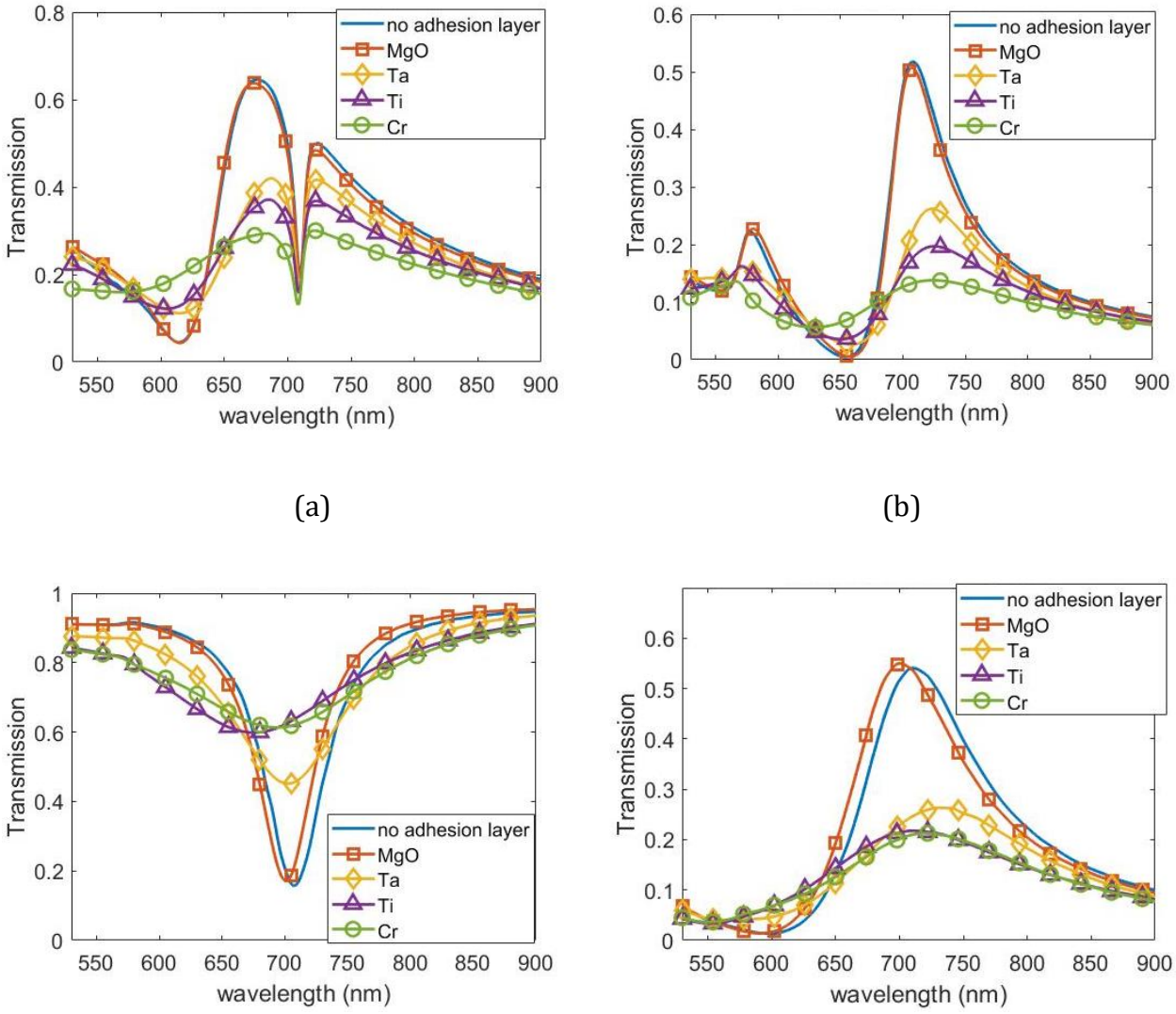

Figure 4.3 Transmission spectra of the designed plasmonic nanostructures, with dimensions provided in Figure 4.2, without and with different adhesion layers, obtained using bulk material properties for adhesion layer material in each case (a) Dimer nanohole array, (b) Nanohole array, (c) Nanodisk array, (d) Bowtie slot antenna array [32].

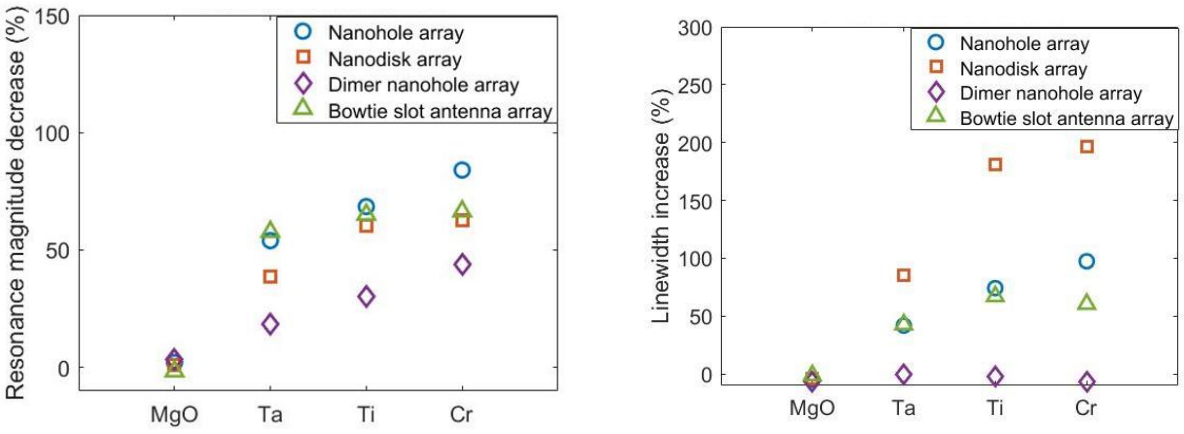

(a) (b)

Figure 4.4 Effect of different adhesion layer materials on resonance of plasmonic nanostructures, considering bulk optical properties and 5 nm thickness for adhesion layer, (a) Resonance magnitude decrease (b) Linewidth increase [32].

Based on the results shown in Figure 4.4 (a), the most affected cases in terms of resonance magnitude are nanohole array or bowtie slot array nanostructures, depending on the adhesion material used. Among the results provided here, it can be seen that Cr as adhesion layer causes the highest reduction in resonance magnitude, causing up to 84% reduction in resonance magnitude. Among the adhesion materials studied here, MgO is the first in terms of causing the least reduction of resonance magnitude (less than 3.6% for all four nanostructures), with Ta being second. Regarding resonance broadening due to presence of adhesion layer, similar overall trend can be seen in Figure 4.4(b). Among the cases included, no resonance broadening occurs when using MgO as adhesion layer. In fact, resonance linewidth decreases when adding MgO adhesion layer to the multilayer stack of the designed plasmonic nanostructures, leading to 1.2% - 7% decrease in linewidth, depending on the

nanostructure geometry. On the other hand, Cr causes the highest resonance broadening (up to 2 ×). In addition, Ta causes less broadening, compared to Ti.

Based on the discussion above, MgO causes the least resonance damping (less reduction of resonance magnitude and less broadening). Furthermore, resonance damping is less for Ta, compared to Ti and Cr (with Cr causing the highest resonance damping). This is because Ta has smaller material losses, quantified with its smaller extinction coefficient (κ) at the design wavelength, while Cr has the largest material losses (Figure 4.5). It is noteworthy to highlight that the severity of resonance damping is also dependent on the nanostructure geometry. For instance, among the nanostructures studied here, resonance damping is the least in the case of dimer nanohole array, since its plasmonic hotspots have the least overlap with adhesion layer as its field enhancement maximum is at the Au/air interface. The simulation results provided here show that MgO has potential to be used as low loss adhesion material, as it does not have any negative effect on resonance of plasmonic nanostructures. In addition, among the metal adhesion materials studied here, Ta is the best choice as it creates less resonance damping. It should be noted that, however, the simulations here provide a rough estimate, as they are based on bulk material properties of adhesion materials while in practice, thin film material properties can be quite different. This will be addressed in the following sections.

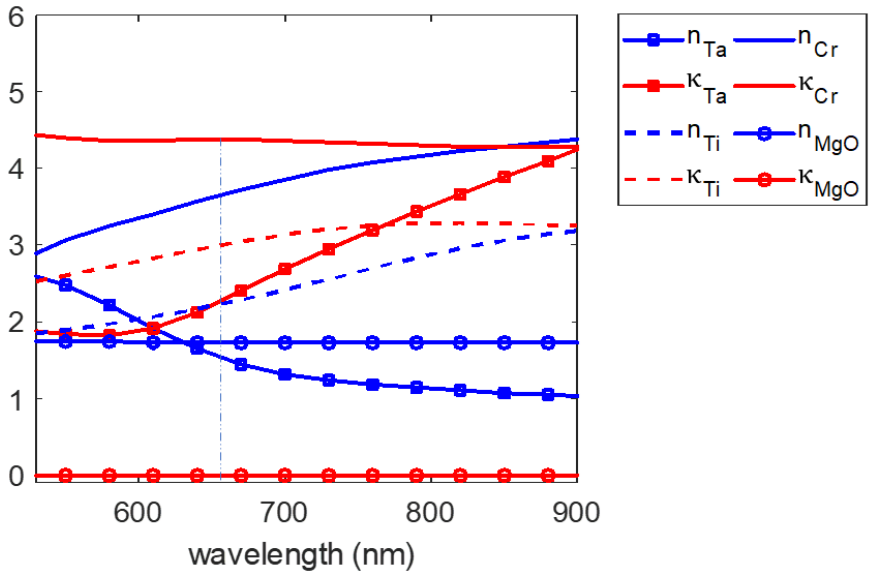

Figure 4.5 Bulk material optical properties of different adhesion material. (Red curves: Refractive index, Blue curves: Extinction coefficient).

4.3 Thin Film Material Properties of Adhesion Layer Material

As mentioned earlier in this chapter, optical properties of thin films can be different from their bulk material properties due to extra scattering which happens at the particle boundaries. Therefore, to obtain a better estimate of how optical properties of adhesion layer affect plasmonic resonance in practice, such effects should be included in the numerical simulations. To address this, and because a major focus of this chapter is to prove MgO as a low loss adhesion layer, optical measurement of MgO thin film is performed to obtain its refractive index and extinction coefficient. In addition, to perform a better comparison of MgO with lossy adhesion materials, Ta thin film is also measured, as it is the best choice among the metal adhesion layers studied in Section 4.2 in terms of smaller resonance

damping.

To perform the thin film optical measurements for MgO and Ta, two samples are fabricated where thin film layers are deposited via magnetron sputtering, in 2 $mTorr$ (0.27 Pa) of Ar process gas, with base pressure of the system being below $2 \times 10^{-8}\ Torr$ ($2.7 \times 10^{-6} Pa$). The first sample is a quartz substrate / MgO (5 nm) multilayer, and the second sample consists of quartz substrate / Ta (5 nm) / Au (2 nm) layers (Figure 4.6). Deposition of Ta and Au films are done via d.c. sputtering, and MgO deposition is performed through r.f. sputtering. The reason for using a thin Au layer on top of Ta thin film is to prevent Ta from oxidization. For both samples, before performing the ellipsometry measurements, a translucent tape was placed on the back of the substrate to minimize back reflection thus improving the accuracy of measurement.

Figure 4.6 Multilayer structure of fabricated samples used for optical thin-film measurement of MgO and Ta.

The fabricated samples are measured using an ellipsometer, where 70° angle of incidence and wavelength range of 530 nm – 750 nm is used for the incident beam. To increase measurement accuracy, an average of 30 scans are taken. For each sample, after obtaining the optical reflection data, curve fitting is performed to match the data. The curve fitting is based on a predefined optical model where Cauchy dispersion equation is considered as the dispersion model for the thin film under study, approximated up to its third term as shown in the following equations:

$$n(\lambda) = N_0 + \frac{N_1}{\lambda^2} + \frac{N_2}{\lambda^4} \tag{4.1}$$

$$\kappa(\lambda) = K_0 + \frac{K_1}{\lambda^2} + \frac{K_2}{\lambda^4} \tag{4.2}$$

For each thin film under study, values of the coefficients in the Cauchy dispersion equation (N_0 , N_1, N_2, K_0 , K_1, K_2) are set to achieve the best fit with the measured data, which leads to an estimate of the refractive index and extinction coefficient of thin film material for each wavelength ($n(\lambda)$ and $\kappa(\lambda)$). A second set of spectroscopic measurement is performed using a Cary-7000 Universal Measurement Spectrophotometer, which confirmed the accuracy of the calculated Cauchy coefficients up to 900 nm wavelength. Therefore, the thin film data presented here includes a 530 nm – 900 nm wavelength range, plotted in Figure 4.7 (solid lines) along with bulk material data in each case (dashed lines). It is clear that Ta in its thin film form, has higher extinction coefficient compared to bulk Ta, meaning higher optical absorption (loss). Also, its refractive index is very different from its bulk version. For MgO thin film, too, refractive index is different from its bulk refractive index. Regarding its extinction coefficient, at larger wavelengths, thin film values are larger than those for bulk material. For shorter wavelengths, however, the measured extinction coefficient for the MgO thin film is smaller and becomes slightly negative. This is because the translucent tape used on the back of the substrate is not able to eliminate all the back reflections, as MgO is an extremely transparent material. Considering this and the fact that the measured extinction coefficient of MgO thin film has a very small magnitude in shorter wavelengths, it is assumed

to be zero at such wavelengths, when using the data for numerical simulations in the next section. Next section provides a second study of the nanostructures designed in Section 4.2, where thin film material data is used for adhesion layer material instead of bulk properties, to provide a more realistic comparison, and to show that MgO in its thin film form also shows a good optical performance, not degrading the plasmonic performance.

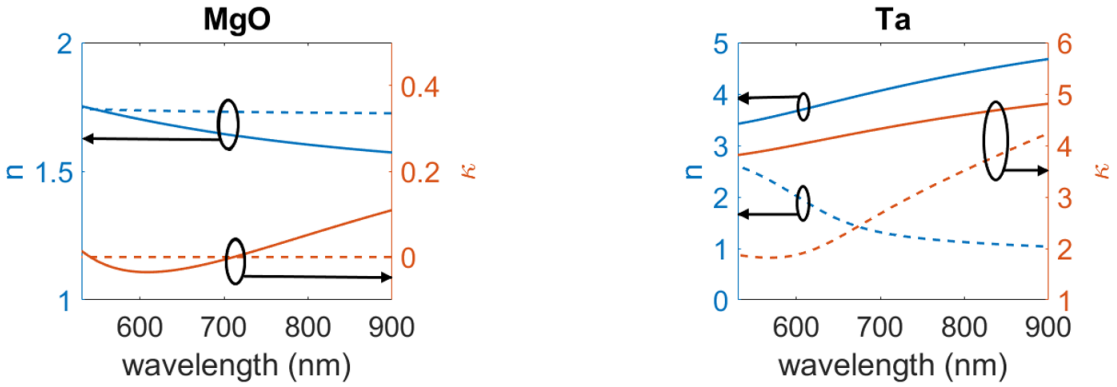

Figure 4.7 Thin-film (solid lines) and bulk (dashed lines) optical properties of (a) Magnesium oxide (b) Tantalum. (Red curves: Extinction coefficient, Blue curves: Refractive index) [32].

4.4 Adhesion Layer Effect on Nanostructures Plasmonic Resonance Considering Thin Film Properties

The measured optical properties of Ta and MgO thin films, provided in Section 4.3, are now used in a second set of optical numerical simulations, for the four nanostructures designed in Section 4.2. The goal is to come up with an experimental estimate to observe how using an MgO adhesion layer can affect the plasmonic resonance of the nanostructures, compared to other adhesion materials used in the literature. To achieve this end, thin film material data

for different adhesion materials is used in COMSOL simulations of the designed nanostructures, assuming adhesion layer of 5 nm thickness in each case. The adhesion materials studied here besides MgO, include the metals commonly used as adhesion layer (Cr, Ti, Ta) as well as indium tin oxide (ITO) which is one of the dielectric adhesion materials used in the literature which has low optical absorption thus expected to create very small degradation in plasmonic resonance of the nanostructures. As for the thin film material properties used in the numerical simulations, for MgO and Ta, thin film material properties obtained from ellipsometry measurements in Section 4.3 are used, which are for 5 nm thick films, same as the thickness assumed in the simulations. For Cr, Ti, and ITO, thin film data is taken from [104, 106, 115], which are measurement data for film thickness of 5 nm, 32 nm, and 17 nm, respectively. Here, for the case of Ti and ITO, it is assumed that such data provide a good estimate for thin 5 nm-thick films. However, it should be mentioned that optical properties of thin film materials can highly change with their thickness. In addition, deposition technique can affect their optical properties. Examples are shown at the end of this section, in Table 4.1, Table 4.2, and Table 4.3 for thin films of Cr, Ti, and ITO, respectively. Hence, while the simulation results included in this section provide an experimental estimate, one should keep in mind that in practice, measurement results may be different.

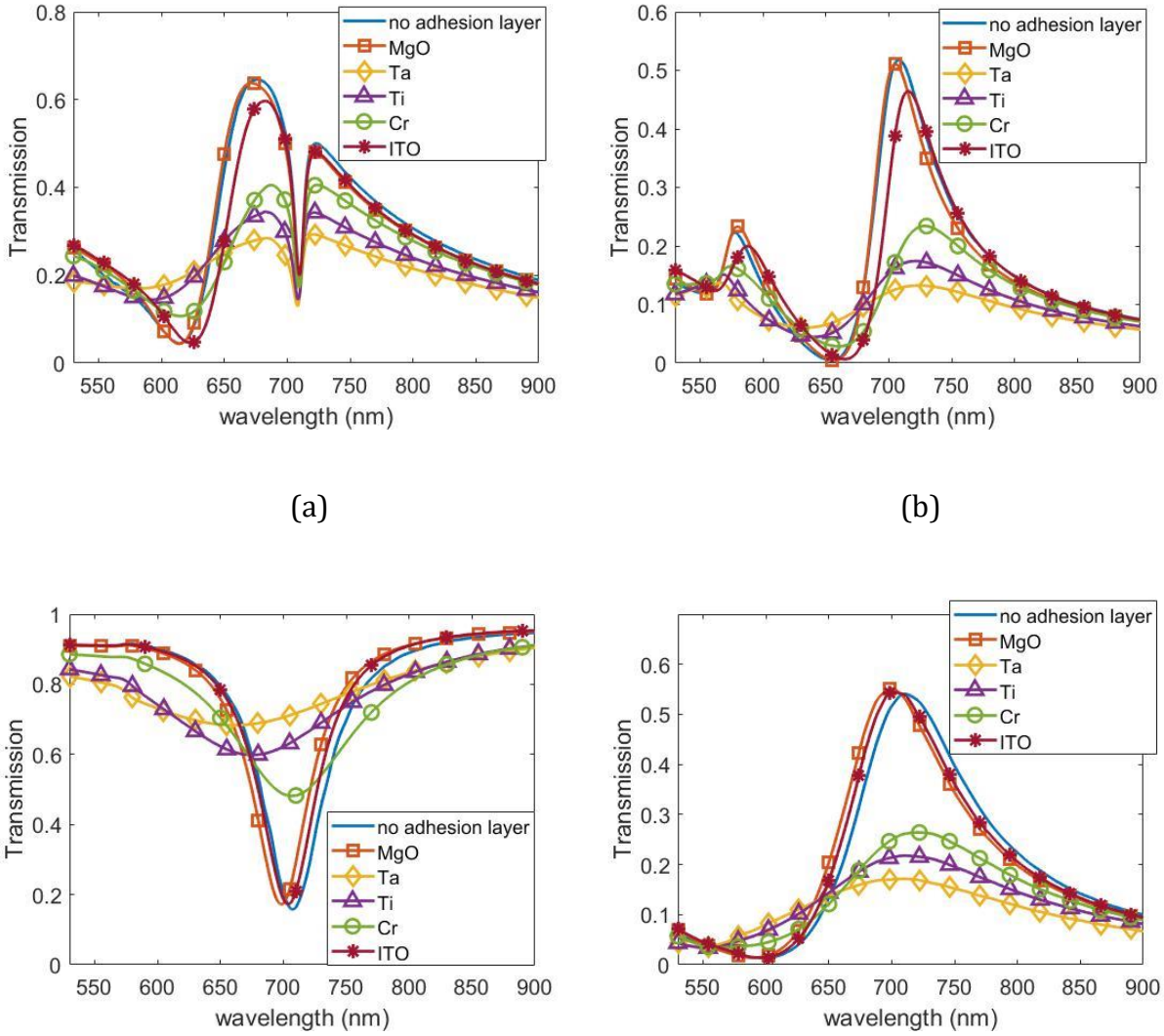

Figure 4.8 Transmission spectra of the designed plasmonic nanostructures, with dimensions provided in Figure 4.2, without and with different adhesion layers, obtained using thin film material properties for each adhesion layer material (a) Dimer nanohole array, (b) Nanohole array, (c) Nanodisk array, (d) Bowtie slot antenna array [32].

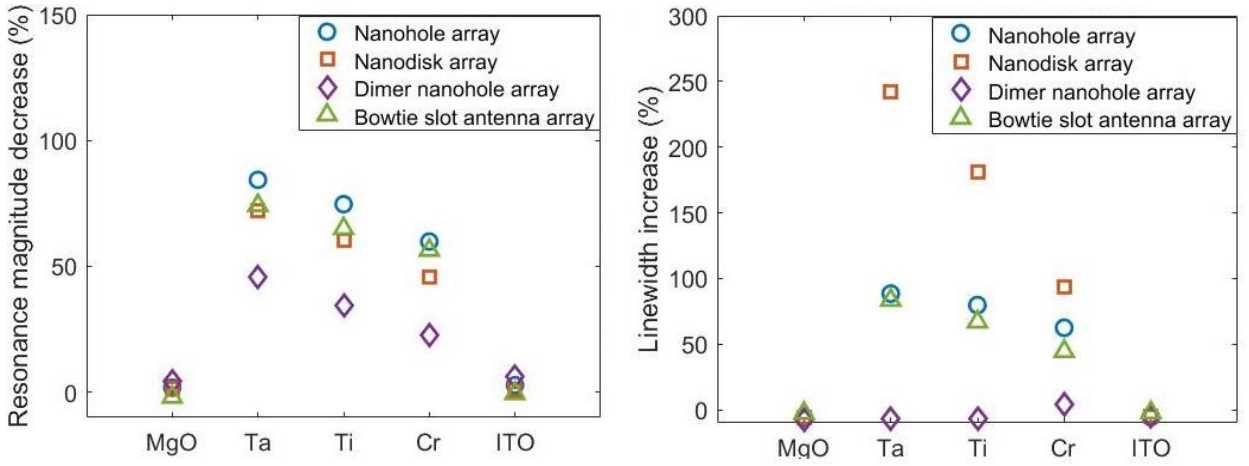

(a) (b)

Figure 4.9 Effect of different adhesion layer materials on resonance of plasmonic nanostructures, considering thin film optical properties and 5 nm thickness for adhesion layer, (a) Resonance magnitude decrease (b) Linewidth increase [32].

Using the thin film material data mentioned above for different adhesion layers, transmission spectrum is obtained for designed nanostructures in Section 4.2 (nanohole array, dimer nanohole array, bowtie slot array, and nanodisk array), shown in Figure 4.8. Similar to the study in Section 4.2, resonance damping in each case is quantified by resonance magnitude reduction and linewidth increase, presented in Figure 4.9. Comparing different adhesion materials, the order of performance among Cr, Ti, and Ta is changed compared to the results presented in Section 4.2. This time, Ta causes the largest resonance damping, quantified with 84% resonance magnitude reduction and more than two times resonance broadening. This is due to the difference between the thickness and deposition method of the measured thin films. It is obvious from the simulation results that MgO also in its thin film form does much better than the metallic adhesion layers, causing no more than 4%

decrease in resonance magnitude and no more than 2% resonance broadening. In addition, MgO has a performance comparable to, and even slightly better than, ITO.

Once again, the effect of adhesion layer on plasmonic resonance depends on the nanostructure geometry and the field distribution of the excited mode. This can be observed in the results included in Figure 4.8 and Figure 4.9, showing the largest resonance broadening for the case of nanodisk array and smallest resonance damping for the case of dimer nanohole array (no more than 4% broadening and no more than 6% resonance magnitude reduction).

The results presented here further verify that MgO is a good alternative as a low-loss adhesion material in terms of its optical performance. To prove MgO as a good adhesion material, it is also necessary to test its adhesion performance, which is discussed in the next section.

Table 4.1 Effect of thickness and deposition method on optical properties of Cr thin film ($\lambda = 800\ nm$) [32].

Thickness (nm)	n	κ	Reference	Deposition Method
5-35	1.54-2.95	1.55-1.1	[104]	E-beam evaporation
45-70	1.03-1.45	1.33-1.72	[108]	Angle vapor deposition
45	3.16	3.46	[106]	Vacuum evaporation
5-114	2.49-3.42	1.09-1.61	[109]	Magnetron sputtering
124-173.6	3.31-3.33	0.11-0.19	[110]	Thermal evaporation

Table 4.2 Effect of thickness and deposition method on optical properties of Ti thin film ($\lambda = 800\ nm$) [32].

Thickness (nm)	n	κ	Reference	Deposition Method
25	1.54	1.2	[105]	Evaporation
32	3.16	4.01	[106]	Vacuum evaporation
21-133	0.89-1.94	0.57-0.69	[107]	Physical vapor deposition
60	3.28	3.88	[116]	Magnetron sputtering

Table 4.3 Effect of thickness and deposition method on optical properties of ITO thin film ($\lambda = 800\ nm$) [32].

Thickness (nm)	n	κ	Reference	Deposition Method
10.8-104.4	1.45-1.73	0.02-0.04	[117]	Pulsed laser deposition
15-100	1.8-2.14	0.37-4.42	[118]	E-beam evaporation
17	1.77	0.005	[115]	--
80	1.9	~0.007	[119]	Pulsed DC sputtering
80	1.78	≤0.005	[119]	Pulsed DC sputtering (annealed)

4.5 Mechanical Stability of Magnesium Oxide as Adhesion Layer

So far in this chapter, optical performance of MgO was tested, showing its potential to be used in plasmonic nanostructures while minimally affecting their plasmonic resonance. To be able to conclude on the fact that MgO can be used as adhesion layer for such structures, however, one must prove that it is capable of adhering Au onto dielectric substrate. Here,

MgO adhesion is first tested with regards to adhering a uniform Au thin film onto a dielectric substrate. To demonstrate mechanical stability of MgO adhesion specifically for nanoparticles, a second test is performed for fabricated samples of nanohole array and dimer nanohole array.

Regarding the first step of MgO adhesion testing, two samples of Au thin film (30 nm thick) with approximately $10 \times 10\ mm^2$ area are fabricated on Si 100/SiO_x (100 nm) substrate, one without adhesion layer and one with a 3 nm MgO as adhesion layer between the Au film and the substrate. Deposition method used for MgO and Au films is the same as the ellipsometry sample used in Section 4.3 for measuring MgO thin film optical properties. Scanning electron microscopy (SEM) images confirm that the Au layer deposited is polycrystalline in both samples. To test the adhesion of MgO layer, sonication technique [120, 121] is applied to the two samples. The reason to choose sonication for testing is, it is the roughest step the plasmonic devices experience in their process of fabrication or cleaning. Therefore, it can be used to determine if MgO can strong enough adhesion for the Au layer to survive the fabrication process. To perform the test, the fabricated samples are placed in separate beakers of isopropyl alcohol and sonicated for 15 minutes. For the sample without adhesion layer, the Au layer started to exfoliate near the edges of the wafer, observed by eye. On the other hand, the sample with MgO adhesion layer shows no changes. This is shown through inspection of the samples through optical imaging microscopy and scanning electron microscopy (SEM), shown in Figure 4.10. Afterwards, sonication is continued for 5 more hours. By the end of this step, it is observed that the Au layer on the sample without adhesion layer is completely exfoliated. However, the sample with the thin MgO adhesion layer shows

no signs of Au exfoliation. This confirms that MgO has strong adhesion performance when used to adhere Au on dielectric substrate.

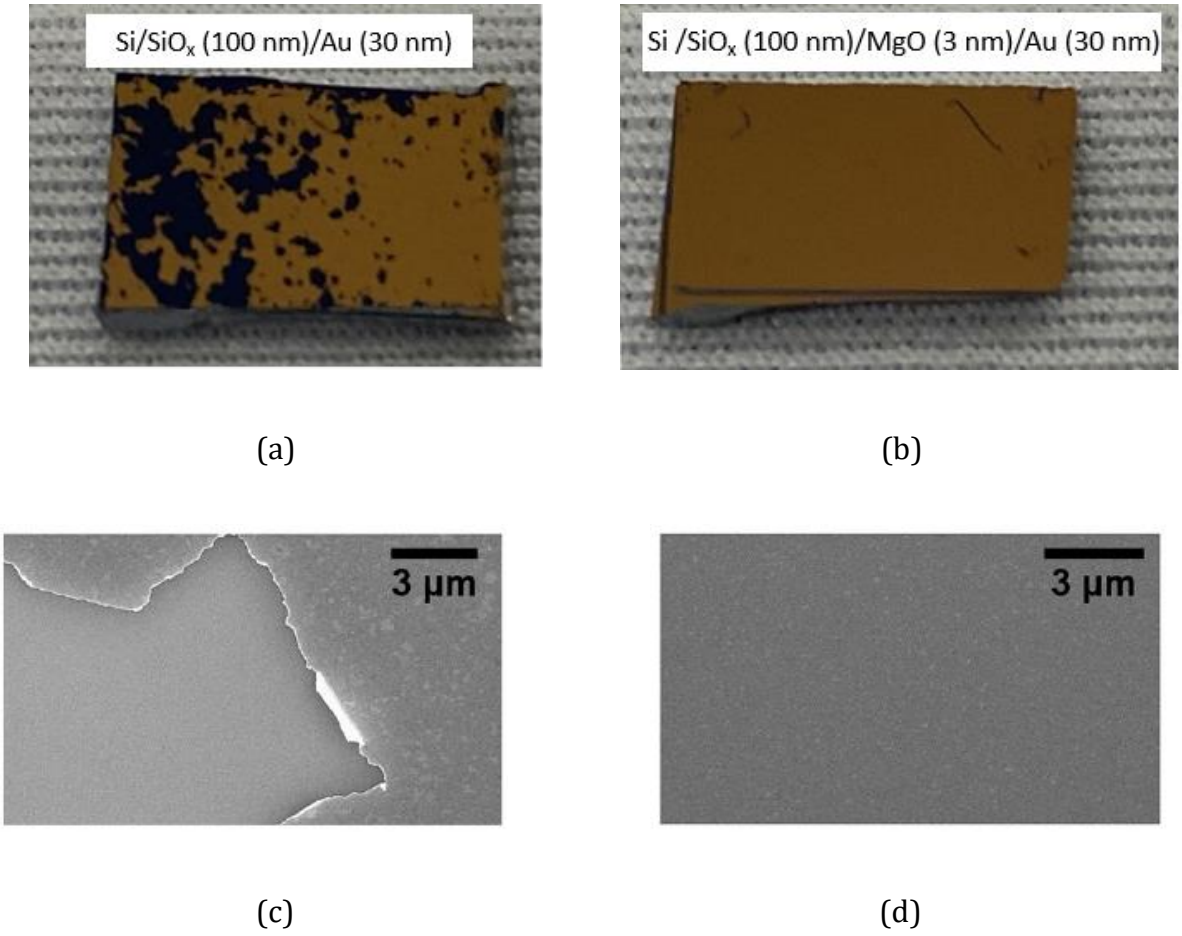

Figure 4.10 Images of test samples for evaluation of mechanical stability of MgO as adhesion layer, after 15 minutes of sonication in isopropyl alcohol (a) Optical imaging microscopy of sample without adhesion layer (b) Optical imaging microscopy of sample with MgO adhesion layer (c) Scanning electron microscopy of sample without adhesion layer (d) Scanning electron microscopy of sample with MgO adhesion layer [32].

To further test the MgO adhesion performance, in a second step, fabrication of a nanohole array and a dimer nanohole array is performed while using MgO as adhesion layer. To this end, a multilayer stack of MgO and Au layers is used (quartz substrate / MgO (3 nm) / Au (60

nm) / MgO (6 nm) / Au (5 nm) is used). The fabrication process is described in the following. A single layer positive tone e-beam resist polymethyl methacrylate (PMMA 495A4) is spin coated on top of the multilayer stack at 3000 rpm. The resist is then prebaked for 15 minutes at 180C, followed by electron beam exposure at 100 kV with 100uC/cm2 does level (Vistec EBPG 5000þES E-beam Writer). Afterwards, the resist is developed in standard MIBK:IPA 1:3 solution for 45 seconds, and rinsed by isopropyl alcohol for 30 seconds and N2 blow dry. At this point, Ar^+ ion milling is used to etch the exposed parts of the multilayer stack and create the nanohole patterns in it. Next, to remove the resist, the sample is left in 60C acetone for 45 minutes, then sonicated for less than 15 seconds. Finally, the sample is rinsed with isopropyl alcohol, with another brief sonication, then approximately 45 seconds of rinsing with HPLC water and N2 blow dry.

SEM images of the fabricated nanostructures (nanohole array and dimer nanohole array) are shown in Figure 4.11. It can be observed that the nanoholes have smooth circular shapes per expectation, while the samples have gone under several steps of sonication and rinsing. This confirms that MgO has strong mechanical stability with regards to metallic nanoparticles, strong enough to have them survive the fabrication process.

It is noteworthy to mention that MgO is hydroscopic, which may potentially interfere with its adhesion properties. However, in a plasmonic device where it is covered by noble metals or other stable metals, its exposure to water and the potential damage caused by it is minimized. For applications where MgO has significant exposure to water, the potential damage should be evaluated through further study.

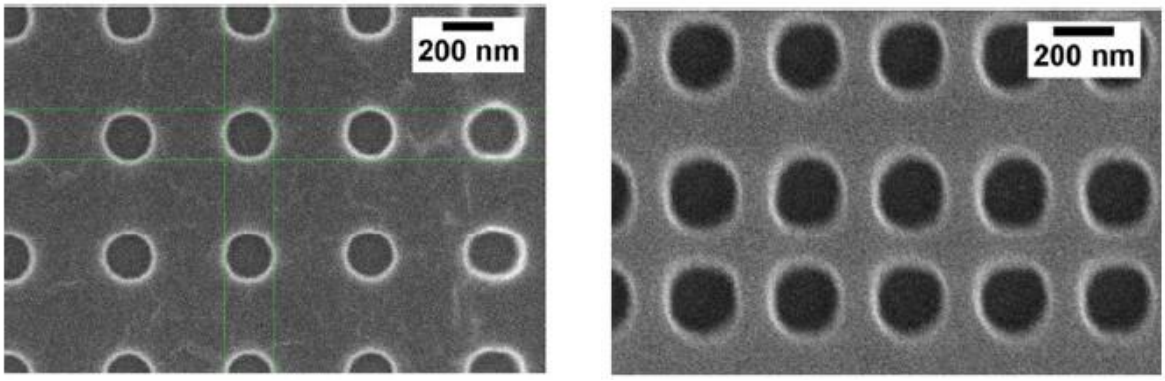

(a) (b)

Figure 4.11 SEM images of fabricated nanostructures using MgO as adhesion layer: (a) Nanohole array, (b) Dimer nanohole array (fabricated in multilayer stack of quartz substrate / MgO (3 nm) / Au (60 nm) / MgO (6 nm) / Au (5 nm)) [32].

4.6 Conclusion

In summary, MgO is proposed and testing as an alternative low loss adhesion layer. Optical performance of MgO as adhesion layer is initially studied through numerical simulations, considering its bulk material properties, confirming its potential as an adhesion layer which does not negatively affect the performance of plasmonic devices. Furthermore, as thickness of adhesion layer is typically a few nanometers, thin film optical properties of MgO are measured via ellipsometry measurements, which confirmed its promise as a low loss adhesion layer. Furthermore, adhesion performance of MgO is tested using sonication technique, showing its strong adhesion properties. Finally, mechanical stability of MgO is further confirmed through utilizing it in the structure of plasmonic nanostructures and showing that their geometry turns out to be as expected.

Chapter 5

Parallel Opto-electronic Readout of STT-RAM

5.1 Introduction

In general, readout of random access memory (RAM) cells can be accomplished optically or electrically [33-38]. Optical readout methods, in specific, have the advantage of improving the memory performance, increased data transfer rate between memory cells and processors, and simplifying the readout circuitry. In optical readout schemes, a major challenge is that optical sources and detectors are typically based on III-V semiconductor materials such as GaAs and InP [33, 34, 122], which are conventionally considered as being incompatible with CMOS technology. However, with recent advancements in silicon photonics, including silicon-based optical components, sources, and detectors, this challenge may be mitigated [123-126].

For readout of STT-RAM in specific, conventional approach is based on measurement of tunneling magnetoresistance, which is performed using an electronic readout circuitry. To achieve the benefits of optical readout mentioned above for STT-RAM, in this chapter, an optoelectronic readout scheme is proposed and theoretically demonstrated. Such method is based on optical rectification (OR) in metal layers, which is a second-order nonlinear optical phenomenon capable of inducing electrical voltage [127, 128]. Hence, there is no need for addition of the III-V semiconductors used in conventional photodetectors. In the proposed

readout scheme, a pulsed laser beam illuminates an array of STT-RAM cells and creates an OR-based photo-induced voltage (OR voltage) across each memory cell (Figure 5.1). The optically induced voltage is then used as a measure to determine the state of each cell, as its magnitude is dependent on the memory state (anti-parallel (AP) vs parallel (P)) [42, 43]. Such method simplifies the readout circuitry, since it eliminates the need for current injection into memory cells.

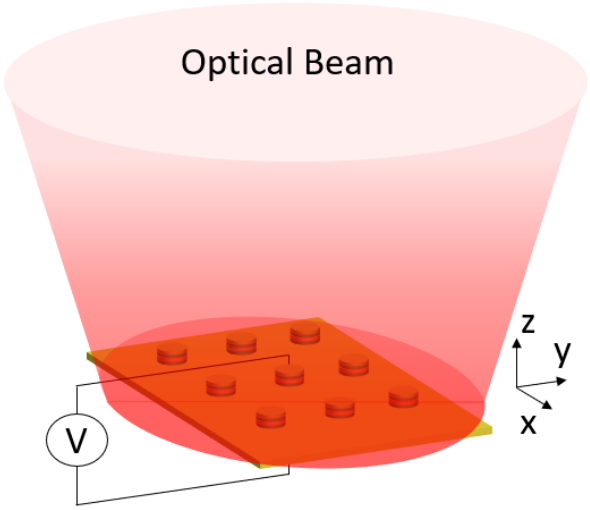

Figure 5.1 Schematic for the proposed parallel optoelectronic readout of STT-RAM cells [43].

As discussed earlier, in Chapter 4, STT-RAM structure includes metals used as electrode contact layers, which can support excitation of plasmonic modes, offering high sensitivity to changes in STT-RAM. Similar mechanism can be used to increase the magnitude of OR voltage and its variation when changing the state of memory cell, which is known as plasmon drag effect (PLDE) [39-41]. This is beneficial because increasing OR voltage variation with regards to memory state change facilitates higher memory readout speed, provided that proper electronic circuitry for voltage measurement is present. It is noteworthy to mention

that, for correct readout of memory state in each cell, the coupling between memory cells should be minimized. Therefore, the excited plasmonic mode used here for enhancing the OR voltage variation with memory state, is based on non-propagating plasmonic mode, localized surface plasmon (LSP) [42, 43]. As explained in Chapter 1, memory state of STT-RAM cells reflects on its electrical resistance (or conductivity), which is facilitated by tunneling effect. As the dielectric barrier (MgO layer) in STT-RAM has much smaller conductivity than the ferromagnet layers and the metal contact layers, one can assign all the tunneling conductivity to the MgO layer. This means that for enhancing the OR voltage change due to change of memory state, the LSP resonance is desired to show strong field enhancement around the MgO layer.

The organization of this chapter is explained in the following. First, excitation of LSP mode in STT-RAM multilayer is discussed, followed by description of the model used for calculation of OR voltage. The calculated OR voltage and its changes with the memory state change is then shown to follow the plasmonic enhancement. It is explained, subsequently, that the plasmonic enhancement in variation of the OR voltage with memory state of the cell improves the potentially achievable readout rate. Next, the effect of changing the dimensions of STT-RAM array on the excited LSP resonance is explored, which affects the potentially achievable memory readout rate. Finally, a transparent electrode is added to the structure, with the purpose of accommodating probing of the STT-RAM cells.

5.2 Non-Propagating Plasmonic Excitation in STT-RAM

As previously discussed in Chapter 1, the core element of STT-RAM structure is a magnetic tunnel junction, which includes a ferromagnet/dielectric/ferromagnet multilayer, sandwiched between two metal layers serving as electrical contact layers. A typical form of such multilayer in terms of the materials used is Au / CoFeB / MgO / CoFeB / Au, shown in Figure 5.2. Here, the goal is to excite a non-propagating plasmonic mode, localized surface plasmon (LSP) resonance, in STT-RAM cells to enable enhancement of the optically induced OR voltage in each cell. The main reason for choosing a non-propagating plasmonic excitation is to avoid optical coupling between the memory cells, as the interest is on performing readout of individual memory cells. Furthermore, LSP is known to be more sensitive to material changes, compared to propagating plasmonic mode type, surface plasmon polariton (SPP), is known to be more sensitive to changes in its surrounding material [129]. This means, it has potential for larger enhancement of the variation of OR voltage due to switching of memory state in each STT-RAM cell.

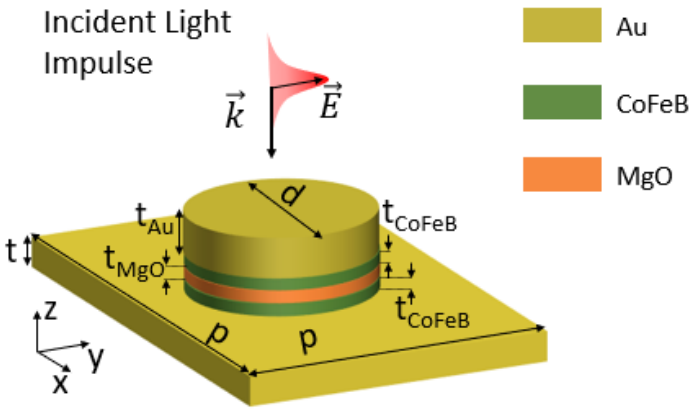

Figure 5.2 Geometry of STT-RAM cell as the unit cell of STT-RAM array shown in Figure 5.1 [43].

To excite the LSP mode, and to show its contribution to enhancement of OR effect to be used for readout of each memory cell, the STT-RAM array is designed to support LSP resonance around 1.5 μm wavelength. The simulation tool used for performing such design, as well as further studies in this chapter, is COMSOL Multiphysics 5.6. In this section and for the rest of this chapter, optical illumination is modeled as a linearly polarized (along y direction) normally incident plane wave, as shown in Figure 5.2. To reduce the simulation time and based on symmetry of the unit cell with respect to its yz symmetry plane, only half of the unit cell is defined in the simulation geometry. To account for the other half of the unit cell as well as periodicity of the array along x direction, perfect magnetic conductor (PMC) boundary conditions are defined on boundaries of the simulation domain which are parallel to yz plane. For periodicity along y direction, perfect electric boundary condition (PEC) is defined on the simulation boundaries parallel to xz plane. Regarding the material data used in the simulations, refractive index of MgO is set to 1.73 based on the measurement data reported in [85]. For Au, material data is taken from [90], and for CoFeB layers, thin-film material data presented in [83] is used. It should be noted that the thin-film data given in [83] for CoFeB includes only up to 1.6 μm wavelength, which is extrapolated for up to 1.8 μm for simulations here. Moreover, it is important to note that the effect of film thickness on the optical properties of the thin film layers in the structure of STT-RAM is ignored in the analyses throughout this chapter.

For increasing the variation of OR voltage with regards to memory state change, the excited plasmonic mode should have strong optical absorption at the design wavelength, which can be identified as a peak in the absorption spectrum of the STT-RAM array. Furthermore, a the

excited LSP mode should provide strong field localization in the MgO layer, where the changes of the memory state will be modeled. As initial demonstration, design of STT-RAM array is performed for excitation of an LSP mode around the 1.5um design wavelength. There are two design dimensions that are used to achieve a strong LSP resonance: nanodisk diameter (d), which is used for tuning the resonance wavelength, and the array period (p), which affects the resonance strength as its value specifies the fill factor of the memory cell while d is kept fixed. Other dimensions of the STT-RAM array include thickness of different layers. Thickness of MgO and CoFeB layers are chosen based on typical values used in STT-RAM cells ($t_{MgO} = 2\ nm$, $t_{CoFeB} = 0.9\ nm$). For the Au ground plane, thickness is set to $t = 100\ nm$, much larger than Au skin depth ($\leq 23.5\ nm$ throughout wavelength range of the simulations here), which helps achieve a strong resonance (meaning strong field localization), as it does not allow coupling of light to the Au/substrate interface. This also simplifies the simulation as there is no need to consider the substrate in the simulations, resulting in reduction of simulation time.

For the designed STT-RAM array, optical absorption spectrum obtained from numerical simulations is presented in Figure 5.3 (a), having a peak at the design wavelength ($1.5\ \mu m$), which shows the plasmonic resonance. In addition to absorption spectrum, spatial average of the electric field magnitude (|E|) throughout the MgO layer, normalized to the electric field of the incident plane wave, is plotted in (red curve in Figure 5.3(a)), which has its peak wavelength close to the wavelength of peak absorption. This confirms that the excited plasmonic mode creates field enhancement in the MgO layer, which is where the magnetoresistance of the memory cell is assigned to. Moreover, electric field distribution at

the plasmonic resonance wavelength, plotted in Figure 5.3(b), confirms that field localization mainly occurs in the MgO layer. This is desirable, as it facilitates enhancement of the changes in OR voltage when changing the memory state. Details regarding modeling of OR voltage in STT-RAM cells and its enhancement due to plasmonic resonance is presented in the next section. It is important to note that optical absorption coefficient and field enhancement both have their resonant peaks around the same wavelength. Therefore, one can use only one of them for designing the structure for achieving a strong plasmonic resonance. For the studies included in the rest of this chapter, absorption spectrum is used for this purpose.

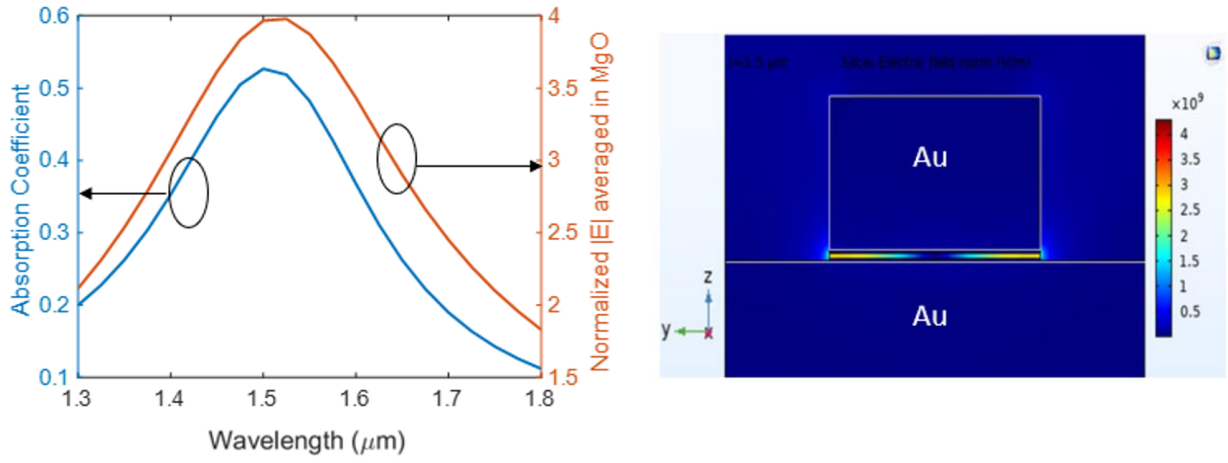

(a) (b)

Figure 5.3 Results of numerical simulation for STT-RAM array (a) Spectra for absorption coefficient (blue curve) and average of electric field magnitude normalized to electric field of incident light (red curve) (b) Electric field distribution over cross section of a unit cell at wavelength of plasmonic resonance (STT-RAM array dimensions are: $p = 200\ nm, d = 100\ nm, t_{Au} = 60\ nm, t_{CoFeB} = 0.9\ nm, t_{MgO} = 2\ nm, t = 100\ nm$) [43].

5.3 Optical Rectification-Based Photo-Induced Voltage in STT-RAM

The OR voltage across each memory cell in STT-RAM array, can be calculated through a simplified derivation of Euler's equation of fluid motion for electrons' dynamics [130], provided in [128]:

$$V_{OR} \approx \frac{1}{n^{(0)}q}\int \frac{dz}{A_z(z)}\left[\int dA_z \,.\left(\frac{\alpha_R}{4}\nabla\left|\tilde{E}\right|^2\right) + \frac{|\alpha|}{4}\langle\left|\tilde{E}(z^-)_\perp\right|^2\rangle_{A_z}\hat{n}(z)\,.\,\hat{z}\right] \tag{5.1}$$

where $n^{(0)}$ stands for the 0th-order electron density in each metal layer, q is the electric charge of single electron ($1.6 \times 10^{-19}C$), α is the electric polarizability in the metal layer, and α_R stands for its real part. $A_z(z)$ is the xy cross sectional area of the unit cell at each z point, $\hat{n}(z)$ is the unit vector perpendicular to the surface of the metal layer pointing outwards, and $\left|\tilde{E}(z^-)_\perp\right|$ is normal component of optical electric field to the surface of the metal layer, at a depth designated by the metal Thomas-Fermi screening length (l_{TF}), which is the exponential scale length for charge screening.

To calculate the OR voltage (V_{OR}) across each memory cell in STT-RAM array, COMSOL Livelink with MATLAB is used to define several cut planes parallel to xy plane across the thickness of each metal layer. Such cut planes are used to record the electric field data from running the optical simulation. The recorded data is then post-processed based on equation (5.1), to calculate the voltage induced in each metal layer of the memory cell. This is followed by summing the obtained voltage values to find the total OR voltage in the memory cell. To

utilize equation (5.1) for calculation of V_{OR}, in addition to the optical electric field data, additional material parameters are needed (α, $n^{(0)}$, and l_{TF}). Value of α can be calculated from the optical material data used in optical simulation (data same as Section 5.2.), i.e., refractive index (n) and extinction coefficient (κ), as:

$$\alpha = \varepsilon_0(\,(n - j\kappa)^2 - 1\,) \tag{5.2}$$

Regarding the parameters $n^{(0)}$ and l_{TF}, for Au layers, $n^{(0)} = 5.9 \times 10^{28}\ m^{-3}$ is used [131], based on which its Thomas-Fermi screening length is obtained using the following equation [132]:

$$l_{TF} \approx \frac{1}{2}\left(\frac{a_0^3}{n^{(0)}}\right)^{1/6} \tag{5.3}$$

where a_0 is the Bohr radius, which is the mean radius of the electron orbit in a hydrogen atom at its ground state ($a_0 \approx 5.29177 \times 10^{-11}\ m$). Based on this equation, for Au, Thomas-Fermi screening length is calculated to be $l_{TF} = 0.583$ Å. For CoFeB layers, the two parameters $n^{(0)}$ and l_{TF}, are approximated with those for Iron (Fe), $n^{(0)} = 17 \times 10^{28}\ m^{-3}$ and $l_{TF} = 1.3$ Å [133]. Such approximation is acceptable for the case of $Co_{20}Fe_{60}B_{20}$ which is one of the typical forms used in the structure of MTJs and has Fe as its major component [134].

To showcase the enhancement effect of plasmonic resonance on the V_{OR} in each STT-RAM cell, equation (5.1) is used to calculate the V_{OR} induced in each cell of the STT-RAM array designed in Section 5.2. For such calculation, a reasonable assumption regarding the incident power and intensity should be made. Here, and for the rest of this chapter, an incident pulsed

laser with a 3 kW peak power and a beam area of $20\mu m \times 20\mu m$ is assumed to illuminate the STT-RAM array. The results of the V_{OR} calculation is included in Figure 5.4, where its plasmonic enhancement is clear, as it has a maximum at the plasmonic resonance wavelength (around 1.5 μm).

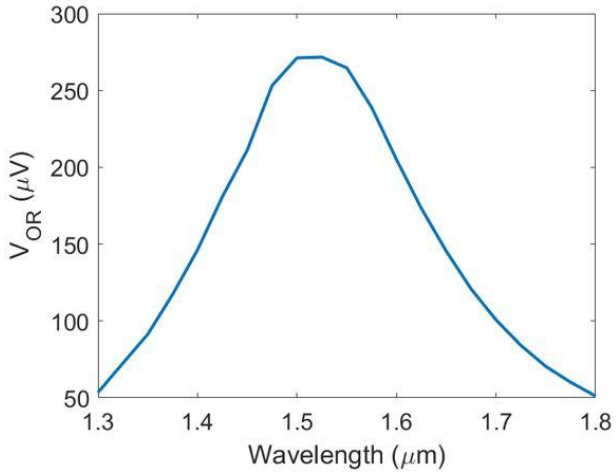

Figure 5.4 Optical rectification voltage induced in each cell in the STT-RAM array designed in Section 5.2, calculated from postprocessing of optical simulation results based on equation (5.1). (Incident pulsed laser with 3 kW peak power and beam spot area of $20\mu m \times 20\mu m$ is assumed. STT-RAM array dimensions are: $p = 200\ nm, d = 100\ nm, t_{Au} = 60\ nm, t_{CoFeB} = 0.9\ nm, t_{MgO} = 2\ nm, t = 100\ nm$) [43].

5.4 Photo-Induced Voltage as a Measure for STT-RAM Memory State

The optically induced V_{OR} in each cell of STT-RAM array can be used to determine their memory state individually. To demonstrate this, memory state of should be considered in the optical model for numerical simulation use for calculation of V_{OR}, described earlier in

Section 5.3. As explained in Chapter 1, memory state of STT-RAM cells changes its resistance, with parallel (P) state of memory cell showing a smaller resistance and anti-parallel (AP) state showing a larger resistance. Resistance value of STT-RAM in each state can be introduced as a conductivity value in its MgO layer, in the optical simulation of STT-RAM array. Such modeling approach is correct, as typical conductivity values, which are obtained later in this section, are much smaller than conductivity of CoFeB [135] and Au [136] layers (more than four orders of magnitude difference). To calculate the conductivity values to assign to the MgO layer in each state of the memory cell, measurement data of a fabricated STT-RAM cell, reported in [137] as resistance area (RA) product of $RA = 2.9\ \Omega\mu m^2$ and tunnel magnetoresistance (TMR) ratio of $TMR = 165\ \%$, is used. Conductivity of the MgO when memory cell is in P state (σ_P) can be calculated based on the following equation:

$$\sigma_P = \frac{t_{MgO}}{RA} \tag{5.4}$$

Based on this equation and using the values of $RA = 2.9\ \Omega\mu m^2$ and MgO layer thickness ($t_{MgO} = 2\ nm$), the conductivity to be assigned to the MgO layer to model the P state is $\sigma_P \approx 690\ S.m^{-1}$. Having this value and using the formula below for TMR,

$$TMR = \frac{\sigma_P - \sigma_{AP}}{\sigma_{AP}} \tag{5.5}$$

the conductivity value for MgO layer at AP memory state is found to be $\sigma_P \approx 260\ S.m^{-1}$.

To quantify the variation of OR voltage due to memory state change of STT-RAM (ΔV_{OR}), the calculated conductivity values for MgO layer at P and AP states are used in two separate optical numerical simulations followed by postprocessing to calculate the OR voltage, as

previously described in Section 5.3. The result of such calculation is presented in Figure 5.5 for the same STT-RAM array design discussed in Sections 5.2 and 5.3. It can be observed, from the plot in Figure 5.5 that the peak of ΔV_{OR} occurs around the plasmonic wavelength, with its value being $\Delta V_{OR,max} \approx 27.26\ \mu V$.

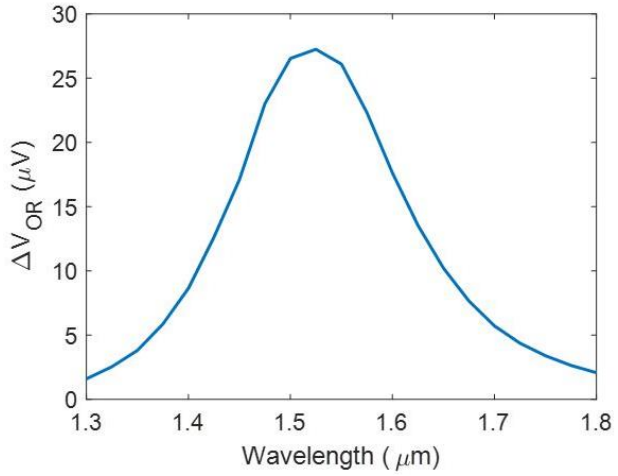

Figure 5.5 Theoretically calculated OR voltage change with memory state change of each cell in the STT-RAM array designed in Section 5.2 (Incident pulsed laser with $3\ kW$ peak power and beam spot area of $20\mu m \times 20\mu m$ are assumed. STT-RAM array dimensions are: $p = 200\ nm, d = 100\ nm, t_{Au} = 60\ nm, t_{CoFeB} = 0.9\ nm, t_{MgO} = 2\ nm, t = 100\ nm$) [43].

5.5 Potentially Achievable Memory Readout Rate

Having calculated the value of ΔV_{OR} and its peak value, one can obtain the maximum achievable memory readout rate when using the proposed STT-RAM parallel optoelectronic readout method. Having the ΔV_{OR} value, memory readout rate is calculated via determining the maximum incident laser pulse repetition rate which can differentiate between the two memory states and multiplying it by the number of STT-RAM cells (N) illuminated by the

incident laser pulse. The maximum permissible pulsed laser repetition rate is defined by the detection bandwidth (BW) required for detecting the OR voltage change as:

$$BW = \frac{1}{SNR}\left(\frac{\Delta V_{OR}}{NEP}\right)^2 \tag{5.6}$$

where the value of ΔV_{OR} is found from optical simulations, SNR is the signal-to-noise-ratio intended for the system, and NEP is noise equivalent power of the system, which includes thermal and magnetic noise of MTJ, and the noise introduced by the readout circuit.

It is clear from equation (5.6), that the value of ΔV_{OR} directly affects the speed of readout, meaning an increase in its value increases the readout rate. Therefore, plasmonic enhancement of ΔV_{OR}, discussed earlier in Section 5.4 can increase the maximum achievable memory readout rate. For example, one can use equation (5.6) to quantify the effect of plasmonic enhancement on the maximum achievable memory readout rate for the designed STT-RAM array discussed in Sections 5.2-5.4 as a 288-fold increase when comparing to the off-resonance wavelength of 1.3 μm wavelength. As mentioned above, the number of memory cells illuminated by the incident pulsed laser (N) also has a direct effect on maximum achievable memory readout speed, and it can be calculated via dividing the beam area (spot size) by the area of one unit cell. For example, the 200 nm period of unit cell in the designed STT-RAM array in Section 5.2, along with the assumption of $20\mu m \times 20\mu m$ spot size, means 10000 memory cells are activated per laser pulse. This has potential to further increase the memory readout rate.

As discussed in Section 5.1, the proposed optoelectronic readout method here is based on

PLDE (or plasmonic enhancement of OR voltage). PLDE is known to be a very fast phenomenon (femtosecond scale) [138]. Therefore, it can easily respond to pulsed lasers with their pulse repetition rate in the MHz range. However, in terms of electronic measurement of the photo-induced voltage in the cells, the total noise performance (NEP) of the system puts an upper limit on the number of cells that can be measured in parallel. In this dissertation, no assumptions are made regarding NEP of the system and the maximum number of cells measurable in parallel. The focus here is solely on estimating the PLDE-based photo-induced voltage in STT-RAM cells and quantifying the contribution of plasmonic enhancement to a higher potentially achievable memory readout rate.

5.6 Designing STT-RAM Array Dimensions for Increased Photo-Induced Voltage

To increase the maximum potentially achievable readout rate for the proposed optoelectronic readout method, based on the discussion in the previous section, one should increase the maximum value of ΔV_{OR}, which occurs around the plasmonic resonance and is notated by $\Delta V_{OR,max}$ here. This can be done through increasing the incident laser peak power or changing the design dimensions to further the plasmonic enhancement of ΔV_{OR}. Before focusing on the effect of design dimensions on plasmonic resonance and enhancement of ΔV_{OR}, study of how incident peak power affects the $\Delta V_{OR,max}$ is presented. Next, the effect of changes in the dimensions of STT-RAM should is studied. In these studies, the incident laser peak power is fixed at 3 kW (except for studying the effect of incident peak power) and the

illumination area is assumed to be $20\mu m \times 20\mu m$. The main design dimensions to be varied are the cell diameter (d), Au nanodisk thickness (t_{Au}), and array period (or unit cell period) (p). Furthermore, since asymmetry is known to cause enhancement of the OR voltage [128], thickness of CoFeB layers (t_{CoFeB}) is changed, one at a time, to see if the additional asymmetry created can further enhance the value of $\Delta V_{OR,max}$. Thickness of MgO layer is kept constant, at $t_{MgO} = 2\ nm$, which is typical for STT-RAM. The focus of the study in this section is on making the plasmonic resonance stronger and observe its effect on the enhancement of $\Delta V_{OR,max}$ which subsequently contributes to the memory readout rate.

5.6.1 Effect of Incident Peak Power

To show the effect of incident peak power on $\Delta V_{OR,max}$, the designed STT-RAM array discussed in Sections 5.2-5.45.5 is used, with the same design dimensions. For this study, the illumination spot size is kept constant, and the incident peak power is varied from 1 kW to 5 kW, meaning the incident intensity is increased. Utilizing the model described in Sections 5.3 and 5.4, $V_{OR,max}$ is calculated for P and AP states of the memory cell, and $\Delta V_{OR,max}$ is calculated from their difference. Results of $V_{OR,max}$ calculation are provided in Figure 5.6(a), showing a linear dependency on the incident peak power. This is in accordance with the expectation for optical rectification phenomenon, which is the underlying effect for creating the photo-induced voltage in each memory cell [139]. Such linear trend is also present in the $\Delta V_{OR,max}$ plot shown in Figure 5.6(b), which results in a quadratic trend for the maximum

potentially achievable memory readout rate, as it is proportional to $(\Delta V_{OR,max})^2$ based on equation (5.6).

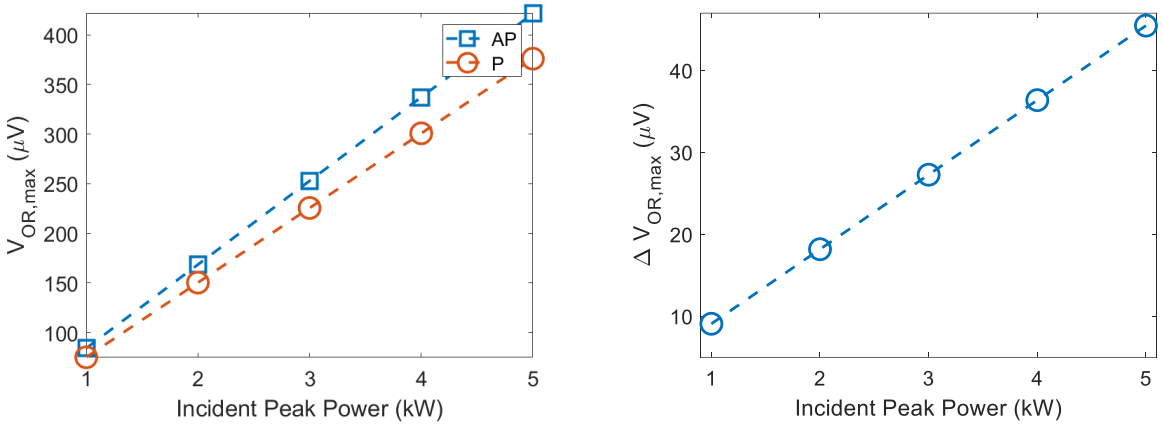

(a) (b)

Figure 5.6 Effect of changing peak power of the incident laser pulse illuminating the STT-RAM array on (a) Maximum OR voltage in each memory cell for anti-parallel and parallel memory states (b) Change in the maximum OR voltage in each memory cell due to memory state change (Illumination area of $20\mu m \times 20\mu m$ is assumed. STT-RAM array dimensions are: $p = 200\ nm, d = 100\ nm, t_{Au} = 60\ nm, t_{CoFeB} = 0.9\ nm, t_{MgO} = 2\ nm, t = 100\ nm$) [43].

5.6.2 Changing Unit Cell Period

Now that the effect of incident laser peak power on the OR voltage and potentially achievable readout rate is explored, the effect of changes in the dimensions of STT-RAM should be studied as well. This is important because changing the dimensions may increase the strength of plasmonic resonance, which in turn enhances the $\Delta V_{OR,max}$ in each memory cell thus increasing the potentially achievable memory readout rate. Firstly, effect of changing

the unit cell period (p) is studied. Changing p directly changes the fill factor of nanodisks in the unit cell. An increase in p results in smaller fill factor, which in turn reduces the peak value of absorption coefficient, meaning the plasmonic resonance is weakened. This is shown in Figure 5.7(a) (the red curve). It is also noteworthy to mention that for p values larger than a critical value ($p = 150\,nm$), changing p does not affect the plasmonic resonance wavelength (blue curve in Figure 5.7 (a)). This is in accordance with the assumption that the excited plasmonic mode is a non-propagating LSP mode (as mentioned in Section 5.2). For $p = 150\,nm$, a slight red shift of resonance wavelength can be observed, which is due to minor coupling between the memory cells. Since the focus here is on memory readout, the OR voltage created in each cell should only be affected by the memory state of it, not its adjacent cells. Therefore, value of p should be large enough to avoid inter-cell coupling.

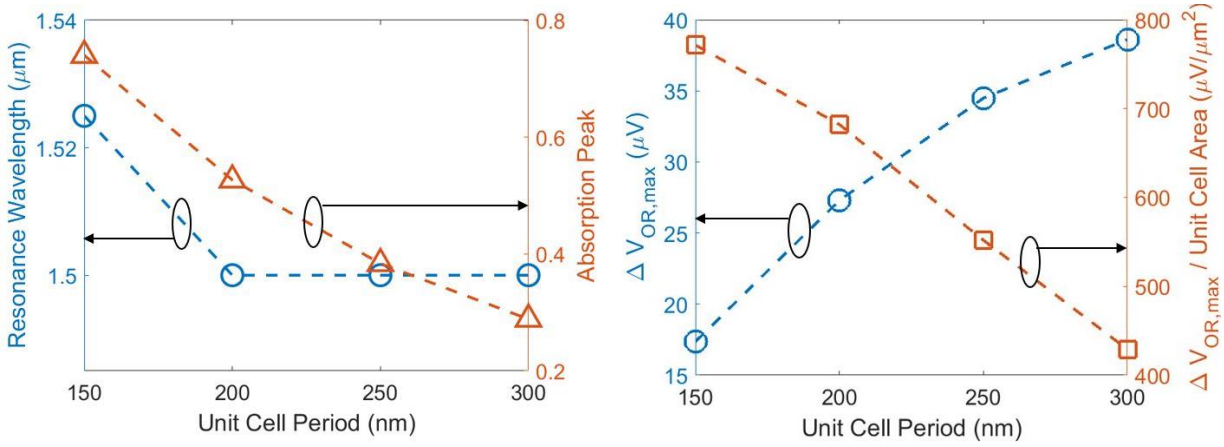

(a) (b)

Figure 5.7 Effect of changing the unit cell period of STT-RAM array on (a) Plasmonic resonance wavelength and absorption peak (b) Change in maximum OR voltage in each memory cell of the array due to its memory state change, and its normalized value to the unit cell area (Incident pulsed laser with 3 kW peak power and beam

spot area of $20\mu m \times 20\mu m$ are assumed. STT-RAM array dimensions are: $d = 100\ nm, t_{Au} = 60\ nm, t_{CoFeB} = 0.9\ nm, t_{MgO} = 2\ nm, t = 100\ nm$) [43].

While it is observed that the LSP resonance in STT-RAM cells weakens when the value of p is increased (due to reduction of absorption peak), larger p values result in increased $\Delta V_{OR,max}$ (blue curve in Figure 5.7 (b)). This is merely due to the incident intensity being kept constant when changing p, using the 3 kW peak power and $20\mu m \times 20\mu m$ illumination array assumption for the incident laser beam, as mentioned earlier. This means the incident power per unit cell becomes larger when increasing the unit cell period, contributing to increased $\Delta V_{OR,max}$. To verify this, another set of data is generated by normalizing $\Delta V_{OR,max}$ to the unit cell area, plotted as the red curve in Figure 5.7(b), showing a reducing trend with increase of p. In addition, one should note that the number of memory cells illuminated by the incident laser pulse becomes smaller for a fixed beam area when increasing p. Therefore, to evaluate the overall effect of p on the maximum potentially achievable readout rate, $N \times (\Delta V_{OR,max})^2$ can be used as a measure, based on the discussion in Section 5.5, plotted in Figure 5.8. It can be observed when increasing p, this parameter first increases then decreases, with its peak value at $p = 250\ nm$. Therefore, to achieve a higher potentially achievable readout speed, too small or too large values for p should be avoided.

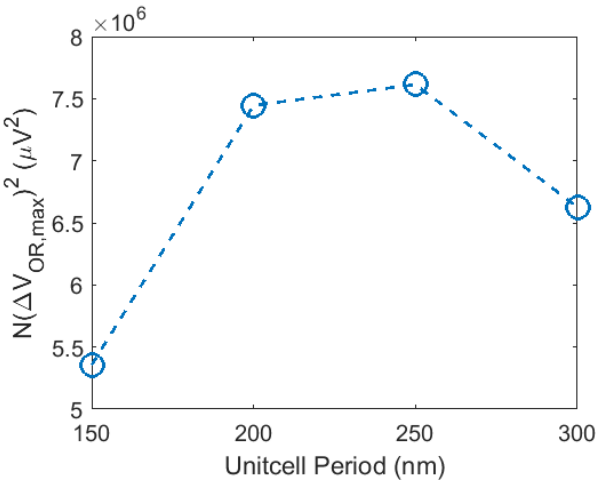

Figure 5.8 Plot of $N \times (\Delta V_{OR,max})^2$ versus unit cell period, as a measure for evaluating the effect of changing the unit cell period on maximum potentially achievable memory readout rate (Incident pulsed laser with 3 kW peak power and beam spot area of $20\mu m \times 20\mu m$ are assumed. STT-RAM array dimensions are: $d = 100\ nm, t_{Au} = 60\ nm, t_{CoFeB} = 0.9\ nm, t_{MgO} = 2\ nm, t = 100\ nm$) [43].

5.6.3 Changing Nanodisk Diameter

Besides the unit cell period, nanodisk diameter (d) is also a major design parameter, which is the main decision-maker for setting the resonance wavelength, creating a red-shift when increased (blue curve in Figure 5.9(a)). This matches the theoretical expectation, as the value of d sets the limit for confinement of the optical field component along y direction, which is the main field component of the incident field and the excited LSP resonant mode. Moreover, increasing d results in larger optical absorption peak values, as shown in Figure 5.9(a), meaning stronger plasmonic resonance. This is because the fill factor of the nanodisks in each unit cell of the STT-RAM array increases with increasing d. Although an increase in d value leads to a stronger resonance which is expected to create a larger value of $\Delta V_{OR,max}$ as

explained in Section 5.3, it also increases the cross-section area, A_z, appearing in equation (5.1), which has a reducing effect on $\Delta V_{OR,max}$. These two contradictory effects, when combined, result in optimal value of $d = 100\ nm$ providing largest $\Delta V_{OR,max}$, which in turn increases the maximum potentially achievable memory readout rate. This is shown in Figure 5.9(b).

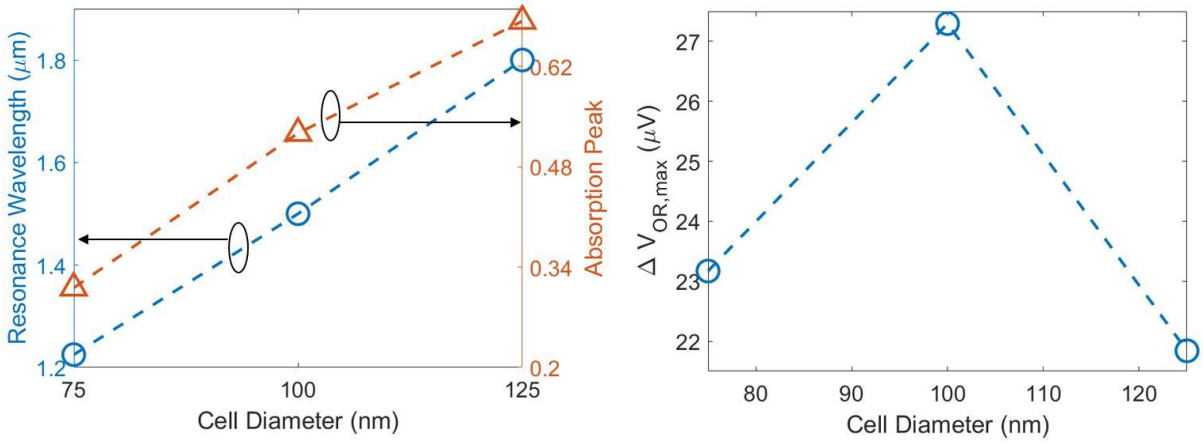

(a) (b)

Figure 5.9 Effect of changing the nanodisks diameter of memory cells in STT-RAM array on (a) Plasmonic resonance wavelength and absorption peak (b) Variation of maximum OR voltage in each memory cell of the array due to its memory state change (Incident pulsed laser with $3\ kW$ peak power and beam spot area of $20\mu m \times 20\mu m$ are assumed. STT-RAM array dimensions are: $p = 200\ nm,\ t_{Au} = 60\ nm, t_{CoFeB} = 0.9\ nm, t_{MgO} = 2\ nm, t = 100\ nm$) [43].

5.6.4 Changing Thickness of Gold Nanodisk

Thickness of the Au nanodisk also affects the plasmonic resonance strength. A larger t_{Au} value can offer more confinement of electric field around the MgO layer, which means larger

variation of in each cell when changing their memory state. Results of simulations where the value of t_{Au} is changed, is shown in Figure 5.10(a). It can be observed that increasing t_{Au} decreases the LSP resonance wavelength. It also increases the absorption peak, meaning a stronger plasmonic resonance. In both curves, changes are more significant for t_{Au} values smaller than a critical value ($t_{Au} < 60\ nm$), which is because of Au skin effect. Strengthening of plasmonic resonance due to increase of t_{Au} leads to increase of $V_{OR,max}$ variation with the memory state, as it increases the field localization in the MgO layer, which is where the memory state change is modeled. Theoretical demonstration of this is performed through calculation of $\Delta V_{OR,max}$ based on numerical simulations. The results show that as t_{Au} increases, value of $\Delta V_{OR,max}$ also increases (Figure 5.10(b)), showing convergence to 31 μV when the Au thickness increases up to $t_{Au} = 105\ nm$.

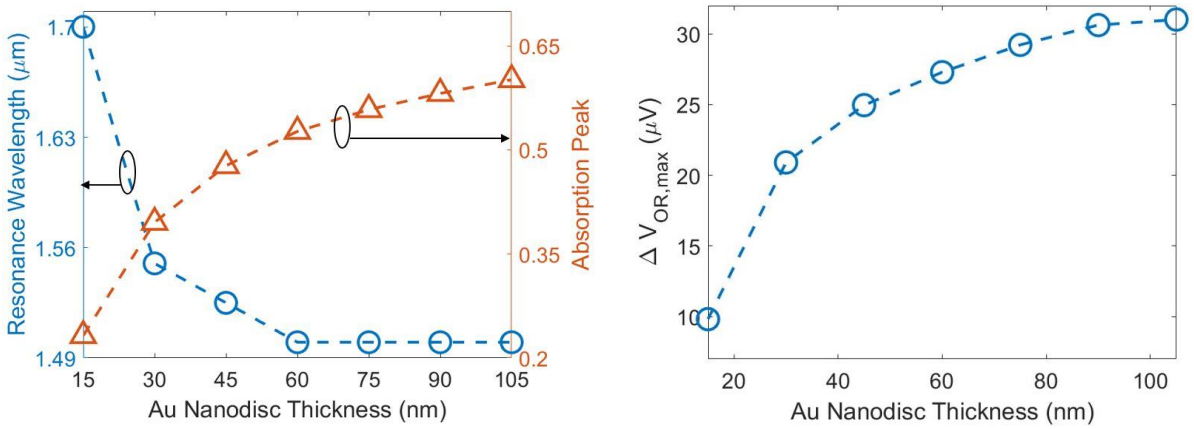

(a) (b)

Figure 5.10 Effect of changing the nanodisks diameter of memory cells in STT-RAM array on (a) Plasmonic resonance wavelength and absorption peak (b) Variation of maximum OR voltage in each memory cell of the array due to its memory state change (Incident pulsed laser with 3 kW peak power and beam spot area of $20\mu m \times 20\mu m$ are assumed. STT-RAM array dimensions are: $p = 200\ nm, d = 100\ nm, t_{CoFeB} =$

$0.9\ nm, t_{MgO} = 2\ nm, t = 100\ nm$) [43].

5.6.5 Changing Thickness of CoFeB Layers

The final design dimension to check, to see if further enhancement of $\Delta V_{OR,max}$ resulting in a larger maximum potentially achievable readout speed is possible, is the thickness of CoFeB layers (t_{CoFeB}). Since asymmetry is known to play a role in enhancement of the OR voltage [128], enhancement of $\Delta V_{OR,max}$ may be achieved when changing the thickness of one CoFeB while keeping the thickness of the other CoFeB layer constant. This is done here by changing the thickness of the CoFeB layer placed on top of the MgO layer shown in Figure 5.2 ($t_{CoFeB,top}$) from $0.9\ nm$ to $1.8\ nm$ while keeping the thickness of the bottom CoFeB layer fixed at $t_{CoFeB,bottom} = 0.9\ nm$. The $0.9\ nm - 1.8\ nm$ range is selected based on typical thicknesses used for STT-RAM. The results of numerical simulations and calculations are presented in Figure 5.11. The plasmonic resonance wavelength is observed to show only a slight change for largest value of $t_{CoFeB,top}$ included in the study here. A more noticeable change is reduction of absorption peak, meaning a weaker plasmonic resonance, when increasing the value of $t_{CoFeB,top}$. This is caused by the material optical losses in CoFeB, which is simply increased by increasing its thickness. At the same time, $\Delta V_{OR,max}$ decreases with increase of $t_{CoFeB,top}$, which in turn decreases the potentially achievable memory readout rate. This means that the effect of optical losses introduced by the additional thickness of top CoFeB layer, is superior to the possible effect of the increased asymmetry. Very similar effect is observed when increasing thickness of the top CoFeB layer while keeping $t_{CoFeB,top}$ constant (results not included here to avoid repetition).

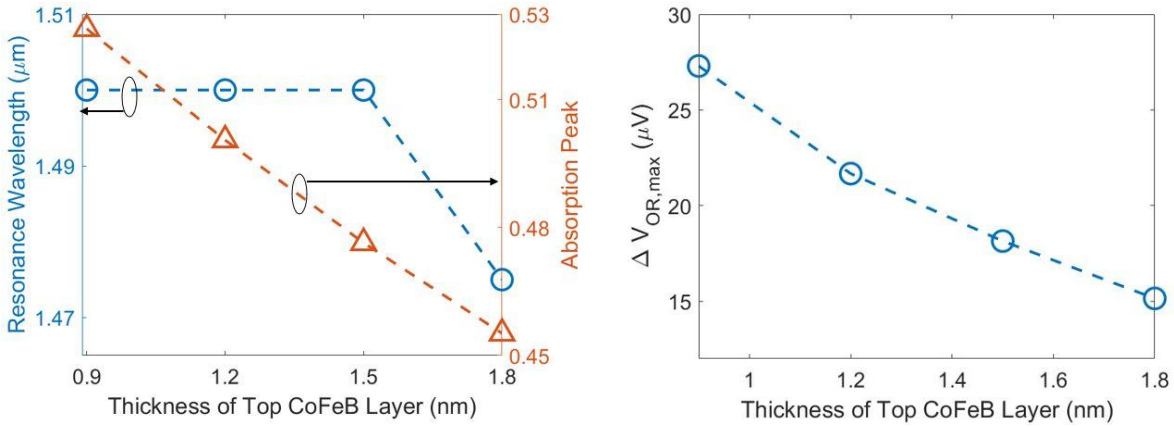

(a) (b)

Figure 5.11 Effect of changing thickness of top CoFeB layer of memory cells in STT-RAM array on (a) Plasmonic resonance wavelength and absorption peak (b) Variation of maximum OR voltage in each memory cell of the array due to its memory state change (Incident pulsed laser with 3 kW peak power and beam spot area of $20\mu m \times 20\mu m$ are assumed. STT-RAM array dimensions are: $p = 200\ nm, d = 100\ nm, t_{Au} = 60\ nm, t_{CoFeB,bottom} = 0.9\ nm, t_{MgO} = 2\ nm, t = 100\ nm$) [43].

5.7 Addition of Transparent Electrode to STT-RAM Array

After choosing the dimensions of the STT-RAM array to achieve larger $\Delta V_{OR,max}$, effect of adding a top electrode layer for facilitating the probing of photo-induced OR voltage in each memory cell should be explored. Such electrode layer would connect the OR voltage to the electronic circuitry used for its measurement. For this purpose, in addition to being electrically conductive, it is necessary for the electrode layer to be optically transparent, to avoid absorption of the optical illumination and assure efficient excitation of LSP mode in each cell. In specific, indium tin oxide (ITO) is known as a transparent conductive material,

owing to it negligible optical absorption [117, 140]. Therefore, here the impact of using an ITO electrode layer, placed on the Au nanodisk, on the value of ΔV_{OR} in STT-RAM array is studied (Figure 5.12). To create mechanical support for the ITO electrode, the space around the nanodisks between the ITO electrode and the Au ground plane at the bottom of unit cell is filled with SiO_2. It is noteworthy to mention that as previously explained in Section 5.5, ΔV_{OR} is studied as it directly affects the potentially achievable memory readout rate (equation (5.6)).

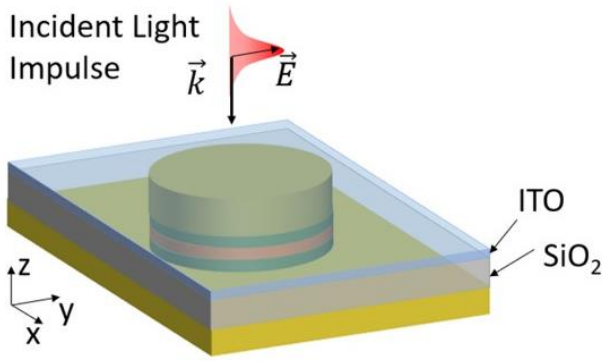

Figure 5.12 STT-RAM unit cell, with ITO electrode, as an optically transparent top electrode, and the SiO_2 spacer added (The orange layer shows the MgO barrier layer, and the green layers are CoFeB layers.) [43].

The STT-RAM dimensions used for the study here are listed in the caption of Figure 5.13, which provide the highest $\Delta V_{OR,max}$ value among the cases studied in the previous section (Section 5.6). Numerical simulation of the STT-RAM array with the ITO electrode layer and the SiO_2 spacer is performed, assuming a thickness for the ITO layer, where ITO optical material data reported in [117] are used. and ITO layer thickness is set to 10 nm. Using the model described in Sections 5.3 and 5.4, variation of OR voltage in each cell (ΔV_{OR}) with memory state change is calculated for different wavelengths around the wavelength of LSP

resonance. To consider the OR voltage induced in the ITO layer in such calculations, Thomas-Fermi screening length of $l_{TF} = 1.4$ Å and electron density of $n^{(0)} = 10^{27} m^{-3}$ are considered for ITO, based on the data reported in [140].

The results of numerical simulations are presented in Figure 5.13, including the absorption spectrum without and with presence of the ITO electrode and the SiO_2 spacer, and the OR voltage change with changing memory cell state when the ITO electrode and SiO_2 spacer are present. Looking at the absorption spectra (blue curves in Figure 5.13), addition of ITO and SiO2 layers results in 30 % increase of the absorption peak, meaning an enhancement of resonance strength, leading to stronger field localization around the MgO layer where the memory state is modeled, as explained in Section 5.4. This in turn increases peak value of ΔV_{OR}, which facilitates larger potentially achievable memory readout rate. Such increase is quantified through calculation to be around 32 % resulting in the peak value of ΔV_{OR} to be $\Delta V_{OR,max} \sim 41\ \mu V$ (red curve in Figure 5.13).

Performing further simulations (results not included here), it is verified that stronger plasmonic resonance and larger $\Delta V_{OR,max}$ when ITO top electrode and SiO_2 spacer are present, is mainly because of the SiO2 spacer added around the memory cells, as it increases the refractive index around the nanodisks, helping achieve further localization of the electric field. It should be noted that addition of the SiO2 spacer also creates a small red shift in the resonance wavelength. In addition, the effect of adding ITO electrode is minor, since ITO has negligible optical absorption. It is noteworthy to quantify the effect of plasmonic enhancement on the value of ΔV_{OR}, as it affects the maximum potentially achievable memory

readout rate. The ΔV_{OR} plot provided in Figure 5.13 (red curve), shows plasmonic enhancement by a factor of ~20 when compared to the off-resonance case of 1.3 μm wavelength. Based on equation (5.6), this translates into an increase in the potentially achievable readout speed by a factor of > 400.

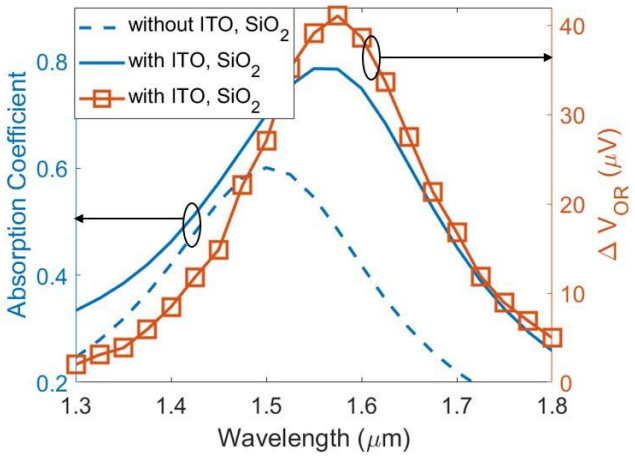

Figure 5.13 Optical absorption coefficient of STT-RAM array without and with ITO top electrode and SiO2 spacer around each memory cell (blue curves), and OR voltage change of STT-RAM array with ITO electrode and SiO2 spacer included (red curve) (Incident pulsed laser with 3 kW peak power and beam spot area of $20\mu m \times 20\mu m$ are assumed. STT-RAM array dimensions are: $p = 200\ nm, d = 100\ nm, t_{Au} = 105\ nm, t_{CoFeB} = 0.9\ nm, t_{MgO} = 2\ nm, t = 100\ nm$) [43].

It is important to note that depending on the incident laser pulse repetition rate, the $\Delta V_{OR,max}$~41 μV may be too small to achieve negligible reading error when performing measurement of ΔV_{OR} in practice. For example, to perform a reliable measurement for a MHz-range laser pulse repetition rate, typically the voltage difference between the two memory states should be in the millivolt scale. Through changing the key parameters of the plasmonic nanostructure geometry (shape and dimensions), the voltage difference may be

increased further. For example, other plasmonic nanostructures such as nanodisk dimers, bowtie antennas may be used, and optimization algorithms can be implemented, to achieve further plasmonic enhancement [14, 141].

5.8 Exploring Possibility of Memory Loss

When evaluating a memory readout method, in addition to estimating the achievable readout rate, possibility of unwanted switching or loss of the data stored in the memory cells should be investigated. For the optoelectronic readout method proposed in this chapter, as the memory cells are exposed to pulsed laser illumination for performing readout of their state, possibility of all-optical switching (AOS) should be explored. In STT-RAM cells, AOS may occur through magnetization change in one of the two ferromagnetic layers (the free layer). This can happen via the so-called inverse Faraday effect, or through thermal effects [142, 143].

Inverse Faraday effect is a phenomenon through which a high intensity laser illumination induces a static magnetization, $\mathbf{M}^{(0)}$, based on the following equation [142]:

$$\boldsymbol{M}^{(0)} = \frac{\chi}{16\pi}(\boldsymbol{E}(\omega) \times \boldsymbol{E}^{*}(\omega)) \tag{5.7}$$

where $\boldsymbol{E}(\omega)$ is the electric field of the incident optical beam at frequency ω, $\mathbf{E}^{*}(\omega)$ is its complex conjugate, and χ is the magneto-optical susceptibility of the magnetic material. Based on this equation, if the incident beam has a linear polarization, it will apply zero magnetization to the magnetic layers in STT-RAM, meaning it cannot change the

magnetization of the free layer in it. As a result, considering that the incident beam assumed for the proposed optoelectronic readout for STT-RAM is linearly polarized, no state change of STT-RAM cells can occur through the inverse Faraday effect.

On the other hand, thermal demagnetization may still happen in the memory cells for linearly polarized incident light [144], causing unwanted loss of the stored data in them. To evaluate such possibility for the proposed optoelectronic readout method, initial estimate of laser-induced heating in the memory cells is performed assuming an incident pulsed laser with pulse width of 1 ps, and wavelength of 1550 nm. Other assumptions are incident laser peak power of 3 kW and beam area of 20 $\mu m \times 20\ \mu m$ (same as assumptions in previous sections of this chapter), and the STT-RAM array design provided in Section 5.7 (shown in Figure 5.12) is considered for the thermal evaluation modeling. Considering a rectangular pulse, these values result in a 3 nJ total pulse energy, which means 0.3 pJ per memory cell.

Since the laser pulsed width is in the order of picosecond, accurate estimation of the temperature increase in the structure requires the fundamental investigation of non-equilibrium processes between electron and phonons, which is usually done via the two-temperature model (TTM), which models thermal excitation of electrons and then an increase due to lattice temperature due to electron-phonon coupling, which happens in a picosecond time scale [145, 146]. However, to get a rough estimate of the temperature increase numerical analysis using COMSOL Multi Physics 5.6 is performed. Since the MTJ cell structure in the designed STT-RAM array (Figure 5.12) mainly consists of gold, which has the lowest specific heat (the heat required to raise the temperature of unit mass of a

substance by one degree Celsius), one can make a conservative estimate of temperature increase in the structure based on temperature increase in gold. Furthermore, 100 % of the incident laser energy is assumed to be turning into heat. Based on these assumptions, about 13 K increase in temperature is calculated. This is the worst-case scenario, since many materials do not respond in such a short time period in terms of heat generation. It should be noted that in the model used here, heat dissipation to the surrounding media and transient dynamics of heating is not properly considered, so the actual temperature increase will be smaller than 13 K. Since 13 K increase will not make the total temperature of the structure close to the Curie temperature (the critical temperature above which the material magnetism is lost) of CoFeB thin films in STT-RAM, which is measured to be 728 K for a 1.1 nm-thick CoFeB layer [147], the temperature increase will not be detrimental to the magnetic state of the memory cells. The results published in [148] estimate the temperature variations to be about 100K when a 200 nm-thick Au film was illuminated by a 1053 nm pulsed laser with 50 mJ/cm^2 fluence and 140 fs pulse width. Since a much smaller laser fluence is used in the thermal modeling here (0.75 mJ/cm^2), the calculated 13 K temperature rise from the simplified model explained here is a conservative estimate. However, future study should be done regarding more rigorous modeling that considers the effect of nanostructure shape and thermal resistance of the material interfaces in the multilayer to obtain an accurate estimate of thermal response in the proposed system.

5.9 Conclusion

In conclusion, parallel optoelectronic readout of STT-RAM cells based on plasmonic enhancement of optical rectification in metal layers of STT-RAM is proposed, to achieve simplified readout circuitry without requiring addition of III-V semiconductors for optoelectronic conversion (like in conventional photodetectors). In this approach, a single optical beam from a pulsed laser source enables parallel activation of STT-RAM cells in placed in the form of an array of memory cells. Based on 2nd-order nonlinear phenomenon called optical rectification (OR), the incident optical power creates a photo-induced voltage across each memory cells, which is shown to be dependent on the memory state of each cell. The change in the OR voltage when changing the state of each memory cell determines the potentially achievable memory readout rate for the proposed method, assuming the matching electronic circuitry can be accommodated for voltage measurements. To enhance the achievable readout rate, plasmonic excitation is used. The effect of STT-RAM array dimensions on such enhancement is studied. The plasmonic enhancement is shown to provide ~20 times increase in the OR voltage change, resulting in increase of achievable readout rate by a factor of more than 400. Furthermore, an ITO electrode layer is added to the structure of STT-RAM to accommodate probing of the voltage in practice. Finally, a simplified numerical simulation is performed to roughly estimate the possibility of unwanted data loss in the memory cells due to pulsed laser illumination, showing the laser energy used in the proposed method is unlikely to change the magnetic state of memory cells. Further study should be performed to obtain an accurate estimate.

Bibliography

[1] P. Zhou, B. Zhao, J. Yang, and Y. Zhang, "Energy reduction for STT-RAM using early write termination," in *2009 IEEE/ACM International Conference on Computer-Aided Design-Digest of Technical Papers*, 2009: IEEE, pp. 264-268.

[2] K. Wang, J. Alzate, and P. K. Amiri, "Low-power non-volatile spintronic memory: STT-RAM and beyond," *Journal of Physics D: Applied Physics,* vol. 46, no. 7, p. 074003, 2013.

[3] M.-T. Chang, P. Rosenfeld, S.-L. Lu, and B. Jacob, "Technology comparison for large last-level caches (L 3 Cs): Low-leakage SRAM, low write-energy STT-RAM, and refresh-optimized eDRAM," in *2013 IEEE 19th International Symposium on High Performance Computer Architecture (HPCA)*, 2013: IEEE, pp. 143-154.

[4] E. Garzon, R. De Rose, F. Crupi, L. Trojman, and M. Lanuzza, "Assessment of STT-MRAM performance at nanoscaled technology nodes using a device-to-memory simulation framework," *Microelectronic Engineering,* vol. 215, p. 111009, 2019.

[5] M. Jasemi, S. Hessabi, and N. Bagherzadeh, "Reliable and energy efficient MLC STT-RAM buffer for CNN accelerators," *Computers & Electrical Engineering,* vol. 86, p. 106698, 2020.

[6] M. Wang, Y. Zhang, X. Zhao, and W. Zhao, "Tunnel junction with perpendicular magnetic anisotropy: Status and challenges," *Micromachines,* vol. 6, no. 8, pp. 1023-1045, 2015.

[7] S. Ikeda *et al.*, "A perpendicular-anisotropy CoFeB–MgO magnetic tunnel junction," *Nature materials,* vol. 9, no. 9, pp. 721-724, 2010.

[8] J.-Y. Choi, D.-g. Lee, J.-U. Baek, and J.-G. Park, "Double MgO-based perpendicular magnetic-tunnel-junction spin-valve structure with a top Co2Fe6B2 free layer using a single SyAF [Co/Pt] n layer," *Scientific reports,* vol. 8, no. 1, pp. 1-7, 2018.

[9] S. S. Parkin *et al.*, "Giant tunnelling magnetoresistance at room temperature with MgO (100) tunnel barriers," *Nature materials,* vol. 3, no. 12, pp. 862-867, 2004.

[10] S. Yuasa, T. Nagahama, A. Fukushima, Y. Suzuki, and K. Ando, "Giant room-temperature magnetoresistance in single-crystal Fe/MgO/Fe magnetic tunnel junctions," *Nature materials,* vol. 3, no. 12, pp. 868-871, 2004.

[11] M. D. Stiles and A. Zangwill, "Anatomy of spin-transfer torque," *Physical Review B,* vol. 66, no. 1, p. 014407, 2002.

[12] K. Huang, N. Ning, and Y. Lian, "Optimization scheme to minimize reference resistance distribution of spin-transfer-torque MRAM," *IEEE Transactions on Very Large Scale Integration (VLSI) Systems,* vol. 22, no. 5, pp. 1179-1182, 2013.

[13] T. Min *et al.*, "A study of write margin of spin torque transfer magnetic random access memory technology," *IEEE Transactions on Magnetics,* vol. 46, no. 6, pp. 2322-2327, 2010.

[14] P. Sadri-Moshkenani *et al.*, "Array of symmetric nanohole dimers with high sensitivity for detection of changes in an STT-RAM ultrathin dielectric layer," *JOSA B,* vol. 36, no. 11, pp. 3090-3097, 2019.

[15] A. Scarpa *et al.*, "Ionizing radiation induced leakage current on ultra-thin gate oxides,"

IEEE Transactions on Nuclear Science, vol. 44, no. 6, pp. 1818-1825, 1997.
[16] J. R. Schwank, M. R. Shaneyfelt, D. Fleetwood, J. Felix, and P. Dodd, "S. Member, P. Paillet, and V. Ferlet-Cavrois,"," *Radiation effects in MOS oxides," IEEE Trans. Nucl. Sci,* vol. 55, no. 4, pp. 1833-1853, 2008.
[17] L. Larcher, A. Paccagnella, M. Ceschia, and G. Ghidini, "A model of radiation induced leakage current (RILC) in ultra-thin gate oxides," *IEEE Transactions on Nuclear Science,* vol. 46, no. 6, pp. 1553-1561, 1999.
[18] H. Liang, H. Wei, D. Pan, and H. Xu, "Chemically synthesized noble metal nanostructures for plasmonics," *Nanotechnology Reviews,* vol. 4, no. 3, pp. 289-302, 2015.
[19] P. Sadri-Moshkenani *et al.*, "Plasmonic detection of possible defects in multilayer nanohole array consisting of essential materials in simplified STT-RAM cell," in *Plasmonics: Design, Materials, Fabrication, Characterization, and Applications XV*, 2017, vol. 10346: International Society for Optics and Photonics, p. 1034639.
[20] P. Sadri-Moshkenani *et al.*, "Array of symmetric nanohole dimers for STT-RAM ultrathin layer sensing," in *CLEO: Science and Innovations*, 2019: Optical Society of America, p. JW2A. 60.
[21] S. Ekgasit, C. Thammacharoen, F. Yu, and W. Knoll, "Influence of the metal film thickness on the sensitivity of surface plasmon resonance biosensors," *Applied spectroscopy,* vol. 59, no. 5, pp. 661-667, 2005.
[22] M. Najiminaini, F. Vasefi, B. Kaminska, and J. J. Carson, "Optical resonance transmission properties of nano-hole arrays in a gold film: effect of adhesion layer," *Optics express,* vol. 19, no. 27, pp. 26186-26197, 2011.
[23] W. M. Abbott *et al.*, "Less is more: Improved thermal stability and plasmonic response in Au films via the use of subnanometer Ti adhesion layers," *ACS applied materials & interfaces,* vol. 11, no. 7, pp. 7607-7614, 2019.
[24] C. Jeppesen, N. A. Mortensen, and A. Kristensen, "The effect of Ti and ITO adhesion layers on gold split-ring resonators," *Applied Physics Letters,* vol. 97, no. 26, p. 263103, 2010.
[25] X. Jiao, J. Goeckeritz, S. Blair, and M. Oldham, "Localization of near-field resonances in bowtie antennae: influence of adhesion layers," *Plasmonics,* vol. 4, no. 1, pp. 37-50, 2009.
[26] H. Aouani *et al.*, "Crucial role of the adhesion layer on the plasmonic fluorescence enhancement," *ACS nano,* vol. 3, no. 7, pp. 2043-2048, 2009.
[27] N. Djaker, R. Hostein, E. Devaux, T. W. Ebbesen, H. Rigneault, and J. Wenger, "Surface enhanced Raman scattering on a single nanometric aperture," *The Journal of Physical Chemistry C,* vol. 114, no. 39, pp. 16250-16256, 2010.
[28] T. G. Habteyes *et al.*, "Metallic adhesion layer induced plasmon damping and molecular linker as a nondamping alternative," *ACS nano,* vol. 6, no. 6, pp. 5702-5709, 2012.
[29] M. Lamy de la Chapelle, H. Shen, N. Guillot, B. Frémaux, B. Guelorget, and T. Toury, "New gold nanoparticles adhesion process opening the way of improved and highly sensitive plasmonics technologies," *Plasmonics,* vol. 8, no. 2, pp. 411-415, 2013.
[30] T. Siegfried, Y. Ekinci, O. J. Martin, and H. Sigg, "Engineering metal adhesion layers that

do not deteriorate plasmon resonances," *ACS nano,* vol. 7, no. 3, pp. 2751-2757, 2013.
[31] P. Sadri-Moshkenani *et al.*, "Effect of Tantalum and MgO adhesion layers on plasmonic nanostructures," in *Nanoengineering: Fabrication, Properties, Optics, Thin Films, and Devices XVI*, 2019, vol. 11089: International Society for Optics and Photonics, p. 1108916.
[32] P. Sadri-Moshkenani *et al.*, "Effect of magnesium oxide adhesion layer on resonance behavior of plasmonic nanostructures," *Applied Physics Letters,* vol. 116, no. 24, p. 241601, 2020.
[33] A. Krishnamoorthy, R. Rozier, J. Ford, and F. Kiamilev, "CMOS static RAM chip with high-speed optical read and write," *IEEE Photonics Technology Letters,* vol. 9, no. 11, pp. 1517-1519, 1997.
[34] D. Samyde, S. Skorobogatov, R. Anderson, and J.-J. Quisquater, "On a new way to read data from memory," in *First International IEEE Security in Storage Workshop, 2002. Proceedings.*, 2002: IEEE, pp. 65-69.
[35] S. C. Li, J.-M. Lee, J. Su, and T.-H. Wu, "1.8-V nanospeed R/W module for 64-kB cross-point cell magnetic random access memory," *IEEE transactions on magnetics,* vol. 41, no. 2, pp. 909-911, 2005.
[36] Y. Chen, H. Li, X. Wang, W. Zhu, W. Xu, and T. Zhang, "A nondestructive self-reference scheme for spin-transfer torque random access memory (STT-RAM)," in *2010 Design, Automation & Test in Europe Conference & Exhibition (DATE 2010)*, 2010: IEEE, pp. 148-153.
[37] A. Emboras *et al.*, "Nanoscale plasmonic memristor with optical readout functionality," *Nano letters,* vol. 13, no. 12, pp. 6151-6155, 2013.
[38] K. Zhang *et al.*, "VO 2-based selection device for passive resistive random access memory application," *IEEE Electron Device Letters,* vol. 37, no. 8, pp. 978-981, 2016.
[39] N. Noginova, V. Rono, F. Bezares, and J. D. Caldwell, "Plasmon drag effect in metal nanostructures," *New Journal of Physics,* vol. 15, no. 11, p. 113061, 2013.
[40] M. Akbari, M. Onoda, and T. Ishihara, "Photo-induced voltage in nano-porous gold thin film," *Optics express,* vol. 23, no. 2, pp. 823-832, 2015.
[41] M. Durach and N. Noginova, "On the nature of the plasmon drag effect," *Physical Review B,* vol. 93, no. 16, p. 161406, 2016.
[42] P. Sadri-Moshkenani *et al.*, "Optoelectronic Readout of STT-RAM Memory Cells Using Plasmon Drag Effect," in *CLEO: QELS_Fundamental Science*, 2021: Optical Society of America, p. JTu3A. 69.
[43] P. Sadri-Moshkenani, M. W. Khan, M. S. Islam, E. A. Montoya, I. Krivorotov, and O. Boyraz, "Optoelectronic Readout of STT-RAM Based on Plasmon Drag Effect," *IEEE Journal of Quantum Electronics,* vol. 57, no. 6, pp. 1-7, 2021.
[44] J. C. Maxwell, *A treatise on electricity and magnetism*. Clarendon press, 1873.
[45] S. A. Maier, *Plasmonics: fundamentals and applications*. Springer, 2007.
[46] A. A. Maradudin, "Introduction: plasmonics and its building blocks," in *Handbook of Surface Science*, vol. 4: Elsevier, 2014, pp. 1-36.
[47] A. Otto, "Excitation of nonradiative surface plasma waves in silver by the method of frustrated total reflection," *Zeitschrift für Physik A Hadrons and nuclei,* vol. 216, no. 4, pp. 398-410, 1968.

[48] E. Kretschmann and H. Raether, "Radiative decay of non radiative surface plasmons excited by light," *Zeitschrift für Naturforschung A,* vol. 23, no. 12, pp. 2135-2136, 1968.
[49] E. Devaux, T. W. Ebbesen, J.-C. Weeber, and A. Dereux, "Launching and decoupling surface plasmons via micro-gratings," *Applied physics letters,* vol. 83, no. 24, pp. 4936-4938, 2003.
[50] J. Homola, S. S. Yee, and G. Gauglitz, "Surface plasmon resonance sensors," *Sensors and actuators B: Chemical,* vol. 54, no. 1-2, pp. 3-15, 1999.
[51] J. Jackson, "Classical Electrodynamics, 3rdWiley," *New York,* 1999.
[52] S. a. Pillai and M. Green, "Plasmonics for photovoltaic applications," *Solar Energy Materials and Solar Cells,* vol. 94, no. 9, pp. 1481-1486, 2010.
[53] P. Zheng, S. K. Cushing, S. Suri, and N. Wu, "Tailoring plasmonic properties of gold nanohole arrays for surface-enhanced Raman scattering," *Physical Chemistry Chemical Physics,* vol. 17, no. 33, pp. 21211-21219, 2015.
[54] A. C. Atre, A. García-Etxarri, H. Alaeian, and J. A. Dionne, "Toward high-efficiency solar upconversion with plasmonic nanostructures," *Journal of Optics,* vol. 14, no. 2, p. 024008, 2012.
[55] A. Lesuffleur, H. Im, N. C. Lindquist, and S.-H. Oh, "Periodic nanohole arrays with shape-enhanced plasmon resonance as real-time biosensors," *Applied Physics Letters,* vol. 90, no. 24, p. 243110, 2007.
[56] F. Eftekhari *et al.*, "Nanoholes as nanochannels: flow-through plasmonic sensing," *Analytical chemistry,* vol. 81, no. 11, pp. 4308-4311, 2009.
[57] J. Homola, "Present and future of surface plasmon resonance biosensors," *Analytical and bioanalytical chemistry,* vol. 377, no. 3, pp. 528-539, 2003.
[58] M. Losurdo, F. Moreno, C. Cobet, M. Modreanu, and W. Pernice, "Plasmonics: Enabling functionalities with novel materials," vol. 129, ed: AIP Publishing LLC, 2021, p. 220401.
[59] L. Wu, P. Bai, X. Zhou, and E. Li, "Reflection and transmission modes in nanohole-array-based plasmonic sensors," *IEEE Photonics Journal,* vol. 4, no. 1, pp. 26-33, 2011.
[60] H. Chen, X. Kou, Z. Yang, W. Ni, and J. Wang, "Shape-and size-dependent refractive index sensitivity of gold nanoparticles," *Langmuir,* vol. 24, no. 10, pp. 5233-5237, 2008.
[61] I. Zoric, M. Zach, B. Kasemo, and C. Langhammer, "Gold, platinum, and aluminum nanodisk plasmons: material independence, subradiance, and damping mechanisms," *ACS nano,* vol. 5, no. 4, pp. 2535-2546, 2011.
[62] K. Bao, N. A. Mirin, and P. Nordlander, "Fano resonances in planar silver nanosphere clusters," *Applied Physics A,* vol. 100, no. 2, pp. 333-339, 2010.
[63] N. A. Mirin, K. Bao, and P. Nordlander, "Fano resonances in plasmonic nanoparticle aggregates," *The Journal of Physical Chemistry A,* vol. 113, no. 16, pp. 4028-4034, 2009.
[64] A. J. Haes, S. Zou, G. C. Schatz, and R. P. Van Duyne, "A nanoscale optical biosensor: the long range distance dependence of the localized surface plasmon resonance of noble metal nanoparticles," *The Journal of Physical Chemistry B,* vol. 108, no. 1, pp. 109-116, 2004.
[65] Y. Shen *et al.*, "Plasmonic gold mushroom arrays with refractive index sensing figures of merit approaching the theoretical limit," *Nature communications,* vol. 4, no. 1, pp.

1-9, 2013.
[66] A. Lesuffleur, H. Im, N. C. Lindquist, K. S. Lim, and S.-H. Oh, "Laser-illuminated nanohole arrays for multiplex plasmonic microarray sensing," *Optics express,* vol. 16, no. 1, pp. 219-224, 2008.
[67] S. Liu, Z. Zhang, and Q. Wang, "High sensitivity and large field enhancement of symmetry broken Au nanorings: effect of multipolar plasmon resonance and propagation," *Optics express,* vol. 17, no. 4, pp. 2906-2917, 2009.
[68] A. V. Kabashin *et al.*, "Plasmonic nanorod metamaterials for biosensing," *Nature materials,* vol. 8, no. 11, pp. 867-871, 2009.
[69] N. Liu *et al.*, "Planar metamaterial analogue of electromagnetically induced transparency for plasmonic sensing," *Nano letters,* vol. 10, no. 4, pp. 1103-1107, 2010.
[70] C.-Y. Tsai, S.-P. Lu, J.-W. Lin, and P.-T. Lee, "High sensitivity plasmonic index sensor using slablike gold nanoring arrays," *Applied physics letters,* vol. 98, no. 15, p. 153108, 2011.
[71] G. A. C. Tellez, R. N. Tait, P. Berini, and R. Gordon, "Atomically flat symmetric elliptical nanohole arrays in a gold film for ultrasensitive refractive index sensing," *Lab on a Chip,* vol. 13, no. 13, pp. 2541-2546, 2013.
[72] P. K. Jain and M. A. El-Sayed, "Plasmonic coupling in noble metal nanostructures," *Chemical Physics Letters,* vol. 487, no. 4-6, pp. 153-164, 2010.
[73] J. Chen, P. Wang, C. Chen, Y. Lu, H. Ming, and Q. Zhan, "Plasmonic EIT-like switching in bright-dark-bright plasmon resonators," *Optics express,* vol. 19, no. 7, pp. 5970-5978, 2011.
[74] T. K. Nguyen, T. D. Le, P. T. Dang, and K. Q. Le, "Asymmetrically engineered metallic nanodisk clusters for plasmonic Fano resonance generation," *JOSA B,* vol. 34, no. 3, pp. 668-672, 2017.
[75] J. Chen, Z. Li, S. Yue, J. Xiao, and Q. Gong, "Plasmon-induced transparency in asymmetric T-shape single slit," *Nano letters,* vol. 12, no. 5, pp. 2494-2498, 2012.
[76] B. Luk'yanchuk *et al.*, "The Fano resonance in plasmonic nanostructures and metamaterials," *Nature materials,* vol. 9, no. 9, pp. 707-715, 2010.
[77] A. Hajebifard and P. Berini, "Fano resonances in plasmonic heptamer nano-hole arrays," *Optics express,* vol. 25, no. 16, pp. 18566-18580, 2017.
[78] J. He, P. Ding, J. Wang, C. Fan, and E. Liang, "Double Fano-type resonances in heptamer-hole array transmission spectra with high refractive index sensing," *Journal of Modern Optics,* vol. 62, no. 15, pp. 1241-1247, 2015.
[79] Y. Zhan, D. Y. Lei, X. Li, and S. A. Maier, "Plasmonic Fano resonances in nanohole quadrumers for ultra-sensitive refractive index sensing," *Nanoscale,* vol. 6, no. 9, pp. 4705-4715, 2014.
[80] A.-P. Blanchard-Dionne and M. Meunier, "Sensing with periodic nanohole arrays," *Advances in Optics and Photonics,* vol. 9, no. 4, pp. 891-940, 2017.
[81] M. J. Weber, *Handbook of Optical Materials*. CRC Press, 2002.
[82] P. R. West, S. Ishii, G. V. Naik, N. K. Emani, V. M. Shalaev, and A. Boltasseva, "Searching for better plasmonic materials," *Laser & photonics reviews,* vol. 4, no. 6, pp. 795-808, 2010.
[83] X. Liang, X. Xu, R. Zheng, Z. A. Lum, and J. Qiu, "Optical constant of CoFeB thin film

measured with the interference enhancement method," *Applied Optics,* vol. 54, no. 7, pp. 1557-1563, 2015.
[84] E. D. Palik, *Handbook of optical constants of solids*. Academic press, 1998.
[85] R. E. Stephens and I. H. Malitson, "Index of refraction of magnesium oxide," *Journal of Research of the National Bureau of Standards,* vol. 49, no. 4, pp. 249-252, 1952.
[86] L. Wu, P. Bai, and E. P. Li, "Designing surface plasmon resonance of subwavelength hole arrays by studying absorption," *JOSA B,* vol. 29, no. 4, pp. 521-528, 2012.
[87] S. Zhang, K. Bao, N. J. Halas, H. Xu, and P. Nordlander, "Substrate-induced Fano resonances of a plasmonic nanocube: a route to increased-sensitivity localized surface plasmon resonance sensors revealed," *Nano letters,* vol. 11, no. 4, pp. 1657-1663, 2011.
[88] M. Najiminaini, F. Vasefi, B. Kaminska, and J. J. Carson, "Nano-hole array structure with improved surface plasmon energy matching characteristics," *Applied Physics Letters,* vol. 100, no. 4, p. 043105, 2012.
[89] D. Maystre, "Theory of Wood's anomalies," in *Plasmonics*: Springer, 2012, pp. 39-83.
[90] P. B. Johnson and R.-W. Christy, "Optical constants of the noble metals," *Physical review B,* vol. 6, no. 12, p. 4370, 1972.
[91] I. H. Malitson, "Interspecimen comparison of the refractive index of fused silica," *Josa,* vol. 55, no. 10, pp. 1205-1209, 1965.
[92] J. W. de Menezes, A. Thesing, C. Valsecchi, L. E. Armas, and A. G. Brolo, "Improving the performance of gold nanohole array biosensors by controlling the optical collimation conditions," *Applied optics,* vol. 54, no. 21, pp. 6502-6507, 2015.
[93] A. De Leebeeck, L. S. Kumar, V. De Lange, D. Sinton, R. Gordon, and A. G. Brolo, "On-chip surface-based detection with nanohole arrays," *Analytical Chemistry,* vol. 79, no. 11, pp. 4094-4100, 2007.
[94] J. Ferreira *et al.*, "Attomolar protein detection using in-hole surface plasmon resonance," *Journal of the American Chemical Society,* vol. 131, no. 2, pp. 436-437, 2009.
[95] J. W. Menezes, J. Ferreira, M. J. Santos, L. Cescato, and A. G. Brolo, "Large-Area fabrication of periodic arrays of nanoholes in metal films and their application in biosensing and plasmonic-Enhanced photovoltaics," *Advanced Functional Materials,* vol. 20, no. 22, pp. 3918-3924, 2010.
[96] J. Henzie, M. H. Lee, and T. W. Odom, "Multiscale patterning of plasmonic metamaterials," *Nature nanotechnology,* vol. 2, no. 9, pp. 549-554, 2007.
[97] A. A. Yanik *et al.*, "An optofluidic nanoplasmonic biosensor for direct detection of live viruses from biological media," *Nano letters,* vol. 10, no. 12, pp. 4962-4969, 2010.
[98] K.-L. Lee, P.-W. Chen, S.-H. Wu, J.-B. Huang, S.-Y. Yang, and P.-K. Wei, "Enhancing surface plasmon detection using template-stripped gold nanoslit arrays on plastic films," *ACS nano,* vol. 6, no. 4, pp. 2931-2939, 2012.
[99] J. Yuan *et al.*, "Enhanced sensitivity of gold elliptic nanohole array biosensor with the surface plasmon polaritons coupling," *Optical Materials Express,* vol. 5, no. 4, pp. 818-826, 2015.
[100] O. Peña-Rodríguez, J. Manzano-Santamaría, J. Olivares, A. Rivera, and F. Agulló-López, "Refractive index changes in amorphous SiO2 (silica) by swift ion irradiation,"

Nuclear Instruments and Methods in Physics Research Section B: Beam Interactions with Materials and Atoms, vol. 277, pp. 126-130, 2012.
[101] J. Manzano, J. Olivares, F. Agulló-López, M. Crespillo, A. Moroño, and E. Hodgson, "Optical waveguides obtained by swift-ion irradiation on silica (a-SiO2)," *Nuclear Instruments and Methods in Physics Research Section B: Beam Interactions with Materials and Atoms,* vol. 268, no. 19, pp. 3147-3150, 2010.
[102] H. Hughes *et al.*, "Radiation studies of spin-transfer torque materials and devices," *IEEE Transactions on Nuclear Science,* vol. 59, no. 6, pp. 3027-3033, 2012.
[103] M. A. Otte, M.-C. Estévez, L. G. Carrascosa, A. B. González-Guerrero, L. M. Lechuga, and B. Sepúlveda, "Improved biosensing capability with novel suspended nanodisks," *The Journal of Physical Chemistry C,* vol. 115, no. 13, pp. 5344-5351, 2011.
[104] V. Lozanova, A. Lalova, L. Soserov, and R. Todorov, "Optical and electrical properties of very thin chromium films for optoelectronic devices," in *Journal of Physics: Conference Series*, 2014, vol. 514, no. 1: IOP Publishing, p. 012003.
[105] S. Mahmoud, "Structure and optical properties of thin titanium films deposited on different substrates," *Journal of materials science,* vol. 22, no. 10, pp. 3693-3697, 1987.
[106] P. Johnson and R. Christy, "Optical constants of transition metals: Ti, v, cr, mn, fe, co, ni, and pd," *Physical review B,* vol. 9, no. 12, p. 5056, 1974.
[107] H. Kangarlou and M. Motallebi Aghgonbad, "Influence of thickness on optical properties of titanium layers," *Optics and Spectroscopy,* vol. 115, no. 5, pp. 753-757, 2013.
[108] R. Kivaisi, "Optical properties of selectively absorbing chromium films deposited at oblique angle of incidence," *Solar energy materials,* vol. 5, no. 2, pp. 115-127, 1981.
[109] J.-P. Lin, L.-M. Lin, G.-Q. Guan, Y.-W. Wu, and F.-C. Lai, "Structural, optical and electrical properties of chromium thin films prepared by magnetron sputtering," *Acta photonica sinica,* vol. 41, no. 8, p. 922, 2012.
[110] M. Khan and S. Haque, "Optical properties of chromium films deposited at normal and oblique angle of incidence," *physica status solidi (a),* vol. 136, no. 1, pp. K35-K39, 1993.
[111] A. G. Brolo, R. Gordon, B. Leathem, and K. L. Kavanagh, "Surface plasmon sensor based on the enhanced light transmission through arrays of nanoholes in gold films," *Langmuir,* vol. 20, no. 12, pp. 4813-4815, 2004.
[112] H. Guo *et al.*, "Optical resonances of bowtie slot antennas and their geometry and material dependence," *Optics express,* vol. 16, no. 11, pp. 7756-7766, 2008.
[113] Y. Khan, A. Li, L. Chang, L. Li, and L. Guo, "Gold nano disks arrays for localized surface plasmon resonance based detection of PSA cancer marker," *Sensors and Actuators B: chemical,* vol. 255, pp. 1298-1307, 2018.
[114] Y. Yang, R. Singh, and W. Zhang, "Anomalous terahertz transmission in bow-tie plasmonic antenna apertures," *Optics letters,* vol. 36, no. 15, pp. 2901-2903, 2011.
[115] R. J. Moerland and J. P. Hoogenboom, "Subnanometer-accuracy optical distance ruler based on fluorescence quenching by transparent conductors," *Optica,* vol. 3, no. 2, pp. 112-117, 2016.
[116] D. A. Belousov, V. S. Terent'ev, E. V. Spesivtsev, and V. P. Korolkov, "Spectral data of refractive index and extinction coefficient for thin films of titanium group metals used for fabrication of optical microstructures," *Data in brief,* vol. 28, p. 104903, 2020.

[117] J. W. Cleary, E. M. Smith, K. D. Leedy, G. Grzybowski, and J. Guo, "Optical and electrical properties of ultra-thin indium tin oxide nanofilms on silicon for infrared photonics," *Optical Materials Express,* vol. 8, no. 5, pp. 1231-1245, 2018.
[118] S. Mohamed, F. El-Hossary, G. Gamal, and M. Kahlid, "Properties of indium tin oxide thin films deposited on polymer substrates," *Acta physica polonica A,* vol. 115, no. 3, pp. 704-708, 2009.
[119] A. Sytchkova *et al.*, "Depth dependent properties of ITO thin films grown by pulsed DC sputtering," *Materials Science and Engineering: B,* vol. 178, no. 9, pp. 586-592, 2013.
[120] I. Zgura, S. Frunza, M. Enculescu, C. Florica, and F. Cotorobai, "Deposition of titanium dioxide layers upon polyester textile materials: Checking the adherence by ultra-sonication," *chemical vapor deposition,* vol. 6, no. 9, 2015.
[121] M. Bazargan, M. M. Byranvand, and A. N. Kharat, "A NEW COUNTER ELECTRODE BASED ON COPPER SHEET FOR FLEXIBLE DYE SENSITIZED SOLAR CELLS," *Chalcogenide Letters,* vol. 7, no. 8, 2010.
[122] S. Mokkapati and C. Jagadish, "III-V compound SC for optoelectronic devices," *Materials Today,* vol. 12, no. 4, pp. 22-32, 2009.
[123] O. Boyraz and B. Jalali, "Demonstration of a silicon Raman laser," *Optics express,* vol. 12, no. 21, pp. 5269-5273, 2004.
[124] H. Rong *et al.*, "An all-silicon Raman laser," *Nature,* vol. 433, no. 7023, pp. 292-294, 2005.
[125] Y. Wan *et al.*, "Monolithically integrated InAs/InGaAs quantum dot photodetectors on silicon substrates," *Optics express,* vol. 25, no. 22, pp. 27715-27723, 2017.
[126] L. Chen, K. Preston, S. Manipatruni, and M. Lipson, "Integrated GHz silicon photonic interconnect with micrometer-scale modulators and detectors," *Optics express,* vol. 17, no. 17, pp. 15248-15256, 2009.
[127] T. Hatano, B. Nishikawa, M. Iwanaga, and T. Ishihara, "Optical rectification effect in 1D metallic photonic crystal slabs with asymmetric unit cell," *Optics Express,* vol. 16, no. 11, pp. 8236-8241, 2008.
[128] H. Kurosawa, S. Ohno, and K. Nakayama, "Theory of the optical-rectification effect in metallic thin films with periodic modulation," *Physical Review A,* vol. 95, no. 3, p. 033844, 2017.
[129] M. Li, S. K. Cushing, and N. Wu, "Plasmon-enhanced optical sensors: a review," *Analyst,* vol. 140, no. 2, pp. 386-406, 2015.
[130] J. E. Goff and W. Schaich, "Hydrodynamic theory of photon drag," *physical Review B,* vol. 56, no. 23, p. 15421, 1997.
[131] V. Palenskis, "Drift mobility, diffusion coefficient of randomly moving charge carriers in metals and other materials with degenerated electron gas," 2013.
[132] J. S. Blakemore, *Solid state physics*. Cambridge university press, 1985.
[133] S. Zhang, "Spin-dependent surface screening in ferromagnets and magnetic tunnel junctions," *Physical review letters,* vol. 83, no. 3, p. 640, 1999.
[134] P. Khalili Amiri *et al.*, "Switching current reduction using perpendicular anisotropy in CoFeB–MgO magnetic tunnel junctions," *Applied Physics Letters,* vol. 98, no. 11, p. 112507, 2011.
[135] G. V. Swamy, P. Rout, M. Singh, and R. Rakshit, "Resistance minimum and electrical

conduction mechanism in polycrystalline CoFeB thin films," *Journal of Physics D: Applied Physics,* vol. 48, no. 47, p. 475002, 2015.
[136] R. A. Matula, "Electrical resistivity of copper, gold, palladium, and silver," *Journal of Physical and Chemical Reference Data,* vol. 8, no. 4, pp. 1147-1298, 1979.
[137] S. Ikeda *et al.*, "Dependence of tunnel magnetoresistance in MgO based magnetic tunnel junctions on Ar pressure during MgO sputtering," *Japanese journal of applied physics,* vol. 44, no. 11L, p. L1442, 2005.
[138] M. Durach, A. Rusina, and M. I. Stockman, "Giant surface-plasmon-induced drag effect in metal nanowires," *Physical review letters,* vol. 103, no. 18, p. 186801, 2009.
[139] D. R. Ward, F. Hüser, F. Pauly, J. C. Cuevas, and D. Natelson, "Optical rectification and field enhancement in a plasmonic nanogap," *Nature nanotechnology,* vol. 5, no. 10, pp. 732-736, 2010.
[140] Z. Chen *et al.*, "High mobility indium tin oxide thin film and its application at infrared wavelengths: model and experiment," *Optics Express,* vol. 26, no. 17, pp. 22123-22134, 2018.
[141] R. Fernández-García, Y. Sonnefraud, A. I. Fernández-Domínguez, V. Giannini, and S. A. Maier, "Design considerations for near-field enhancement in optical antennas," *Contemporary Physics,* vol. 55, no. 1, pp. 1-11, 2014.
[142] A. Kimel, A. Kirilyuk, P. Usachev, R. Pisarev, A. Balbashov, and T. Rasing, "Ultrafast non-thermal control of magnetization by instantaneous photomagnetic pulses," *Nature,* vol. 435, no. 7042, pp. 655-657, 2005.
[143] L. Avilés-Félix *et al.*, "Single-shot all-optical switching of magnetization in Tb/Co multilayer-based electrodes," *Scientific reports,* vol. 10, no. 1, pp. 1-8, 2020.
[144] C.-H. Lambert *et al.*, "All-optical control of ferromagnetic thin films and nanostructures," *Science,* vol. 345, no. 6202, pp. 1337-1340, 2014.
[145] Q.-L. Xiong and X.-G. Tian, "Thermomechanical interaction in metal films during ultrashort laser heating," *Mechanics of advanced materials and structures,* vol. 22, no. 7, pp. 548-555, 2015.
[146] J. B. Lee, K. Kang, and S. H. Lee, "Comparison of theoretical models of electron-phonon coupling in thin gold films irradiated by femtosecond pulse lasers," *Materials transactions,* vol. 52, no. 3, pp. 547-553, 2011.
[147] M. Yamanouchi, A. Jander, P. Dhagat, S. Ikeda, F. Matsukura, and H. Ohno, "Domain structure in CoFeB thin films with perpendicular magnetic anisotropy," *IEEE magnetics letters,* vol. 2, pp. 3000304-3000304, 2011.
[148] L. Jiang and H.-L. Tsai, "Improved two-temperature model and its application in ultrashort laser heating of metal films," 2005.